Université de Strasbourg

UNIVERSITÉ DE STRASBOURG

École doctorale
Mathématiques,
sciences de l'information
et de l'ingénieur | ED 269
Université de Strasbourg

ÉCOLE DOCTORALE MATHEMATIQUES, SCIENCES DE L'INFORMATION ET DE L'INGENIEUR – ED269

ICube-UMR 7353

THÈSE présentée par :

Rima Saadaoui

soutenue le : **27 juin 2023**

pour obtenir le grade de : **Docteur de l'université de Strasbourg**

Discipline/ Spécialité : automatique et robotique

Commande robuste de robots plans à câbles en tenant en compte des déformations des câbles

---

THÈSE dirigée par :
  M. LAROCHE Edouard   Professeur, université de Strasbourg
  Mme BARA Iuliana Gabriela   Professeur, université de Strasbourg

RAPPORTEURS :
  Mme MENINI Laura   Professeur, université de Roma Tor Vergata
  M. ZASADZINSKI Michel   Professeur, université de Lorraine

AUTRES MEMBRES DU JURY :
  M. BOYER Frédéric   Professeur, IMT Atlantic
  M. COURTEILLE Éric   Maitre de conférences, HDR, INSA Rennes
  M. PICCIN Olivier   Maitre de conférences, HDR, INSA Strasbourg
  M. OMRAN Hassan   Maitre de conférences, université de Strasbourg

"I am among those who think that science has great beauty. A scientist in his laboratory is not a mere technician: he is also a child confronting natural phenomena that impress him as though they were fairy tales."— Marie Curie

Acknowledgment

Contents

List of Figures

List of Tables

Nomenclature

Abbreviations

$CDPR$ Cable-Driven Parallel Robot

DAE Differential-algebraic equation

DOF Degrees of freedom

LMI Linear matrix inequalities approach

ODE Ordinary differential equation

RMS Root-mean-square deviation

Coordinate systems

$\mathcal{R}_g$ Fixed global reference frame

$\mathcal{R}_i$ Reference frame attached to the flexible cable $\#i$

$\mathcal{R}_p$ Reference frame attached to the moving platform

Matrices

^gR_p The rotation matrix between $\mathcal{R}_g$ and $\mathcal{R}_p$

$\dot{A}$ The time derivative of the Jacobian matrix of the constraints

$\dot{M}$ The time derivative of the kinetic inertia matrix

$\dot{M}_r$ The time derivative of the kinetic inertia matrix of the system relative to q_r

A The Jacobian matrix of the constraints

A_{11} The bloc (1,1) of the matrix A_1 with dimension $(k \times k)$

A_{12} The bloc (1,2) of the matrix A_2 with dimension $(k \times k)$

B_{11} The bloc (1,1) of the matrix B_1 with dimension $(k \times n)$

H The matrix of the DAE model

J The inverse kinematic Jacobian matrix

$M(s)$ The interconnection transfer matrix in chapter 4

M The kinetic inertia matrix of the system in chapter

M_0 the inertia matrix of the platform

M_i the inertia matrix relative to each cable $\#i$

M_P The projection matrix

M_r The kinetic inertia matrix of the system relative to q_r

M_{int} The intrinsic parameters matrix

M_{PR} The reduced projection matrix of reduced dimension

W The forces matrix

Transfer functions

$G(s)$ The system transfer function

$G_p(s)$ The position part of the system $G(s)$

$G_\alpha(s)$ The orientation part (α) of the system $G(s)$

$G_{T_m}(s)$ The mean tension part of the system $G(s)$

$G_{x-y}(s)$ The translation part $(x-y)$ of the system $G(s)$

$K(s)$ The controller transfer function

$K_p(s)$ The position part of the controller $K(s)$

$K_\alpha(s)$ The orientation part of the controller $K(s)$

$K_{T_m}(s)$ The mean tension part of the controller $K(s)$

$K_x(s), K_y(s)$ The translation part $(x-y)$ of the controller $K(s)$

$P(s)$ The plant system

$S_u(s)$ The sensitivity on the input

$S_y(s)$ The sensitivity on the output

$T_{ed}(s)$ The transfer between the error e and the disturbance d

$T_{er}(s)$ The transfer between the error e and the reference r

$T_{ur}(s)$ The transfer between the control u and the reference r

$T_{vd}(s)$ The transfer between the $v = d + u$ and the disturbance d

$T_{zw}(s)$ The closed-loop transfer function

$W_\alpha(s)$ The weighting functions on the orientation signal

$W_d(s), W_3(s)$ The weighting functions on the disturbance signals

$W_e(s), W_1(s)$ The weighting functions on the error signals

$W_i(s)$ The weighting functions on the input

$W_o(s)$ The weighting functions on the output

$W_p(s)$, The weighting functions on the position signals

$W_{Tm}(s)$ The weighting functions on the mean tension signal

$W_u(s), W_2(s)$ The weighting functions on the control signals

$W_x(s), W_y(s)$ The weighting functions on the translation signals

Scalars

K_{c_i} The kinetic energy of each cable #i

(p_1, p_2, p_3) Poles

$(w_0, w_{00}$ The natural frequencies

(x_e, q_e, q_{r_e}) The operation points

α The orientation of the platform along z axis

α_0 The initial orientation of the platform along z axis

$\ddot{\theta}_i$ The angular acceleration of the motor #i

$\ddot{l}_i$ The second time derivative of length of the cable #i

Δ_M The gain margin

$\dot{\alpha}$ The rotational velocity of the platform along z axis

$\dot{\theta}_i$ The angular velocity of the motor #i

$\dot{\varphi}_i$ The time derivative of the new representation of the flexible mode of cable #i

$\dot{\varphi}_i$ The time derivative of the orientation angle of cables #i

$\dot{K}_{w_i}$ The time derivative of the kinetic energy of the winch drum #i

$\dot{l}_i$ The time derivative of length of the cable #i

$\dot{V}$ The time derivative of the total potential energy associated with the conservative forces exerted by spring of the whole system

$\dot{w}_i$ The time derivative of the new representation of the flexible mode of cable #i

$\dot{x}_p$ The velocity of the platform along x axis

$\dot{y}_p$ The velocity of the platform along y axis

γ The performance criteria

λ_i the Lagrange multipliers for each constraint

$\mathcal{L}$ The Lagrange equation

$\Phi_j(x)$ The function that presents the shape of flexibility

ρ The cable mass per unit length

τ_i The torque of the actuator $\#i$

θ_{i_0} the zero configuration of the actuator $\#i$

θ_i The position of the actuator $\#i$

$\tilde{l}_i$ The length of cable $\#i$ of the transmission unit

$\tilde{l}_t$ The total length of the cables coiled on a coaxial tension winch

ε_p The steady-state error

φ_i The orientation angle of cable $\#i$

ξ The damping ratio

a_{i_j} The flexible mode

A_i The exit point of the cable $\#i$

A_{rk} The elements of the matrix A

$b_m(t)$ The measurement noise signal

B_i The attachment point of the cable $\#i$ at the platform

c Actuation redundancy

c_α The torque exerted around the center of mass O_p of the platform

C_d The derivative gain of the PID (or PD) controller

C_i The integral gain of the PID controller

C_p The proportional gain of the PID (or PD) controller

$d(t)$ The disturbance signal

d The number of the degree of freedom

$e(t)$ The error signal

g The gravity

j_0 The inertia of the drum wrench

j_i The inertia of the drum wrench $\#i$

j_p The inertia of the platform

K The kinetic energy of the whole system

k The number of variables in flexible cable model $o = 3n + 3$

K_p The kinetic energy of the platform

K_r The kinetic energy relative to q_r

k_t The stiffness of the linear spring of the transmission unit

K_{w_i} The kinetic energy of the winch drum and of the coaxial tension winch drum

l_{i_0} The initial unwounded length of cable #i

l_i The length of the cable #i

l_t The total length of the cables

m The mass of the platform

M_i A point located on the unwound portion of the flexible cable #i in chapter '3

N The number of flexibility modes

n The number of cables

n_u The number of controlled inputs

n_w The dimensions of the exogenous inputs $w(t)$

n_y The number of measured outputs

n_z dimensions of the performance outputs $z(t)$

Q_i The generalized force for each variable #i

$r(t)$ The reference signal

r Radius of the winch drum

r_t Radius of the coaxial tension winch drum

sk The longitudinal position

T_i The tension of cable #i

T_m The mean tension of cables

T_m^r The reference of mean tension of cables

$u(t)$ The control signal

V The total potential energy associated with the conservative forces exerted by spring of the whole system

V_i The potential energy associated with the conservative forces exerted by each spring of the transmission unit

V_{p_i}	The gravitational potential energy of each cable #i
v_{x_i}	The velocity of the point M_i of the cable #i along x direction
v_{y_i}	The velocity of the point M_i of the cable #i along y direction
$w(t)$	The exogenous input in chapter 4
w_c	The bandwidth
w_i	The new representation of the flexible mode of cable #i
$x(t)$	The state space vector in chapter 4
x_{A_i}	The position of the the point A_i along x axis
x_{B_i}	The position of the the point B_i along x axis
$x_K(t)$	The state space vector of the controller $K(s)$ in chapter 4
x_{M_i}	The position of the the point M_i along x axis
x_{p_0}	The initial translation of the platform along x axis
x_p	The translation of the platform along x axis
$y_m(t)$	The measurement signal
y_{A_i}	The position of the the point A_i along y axis
y_{B_i}	The position of the the point B_i along y axis
y_{M_i}	The position of the the point M_i along y axis
y_{p_0}	The initial translation of the platform along y axis
y_p	The translation of the platform along y axis
$z(t)$	The performance output

Vectors

${}^p e_i$	Column vector of the fixed position of the point B_i in $\mathcal{R}_p$
$\ddot{q}$	Column vector of the second time derivative the generalized coordinate
$\dot{\theta}$	Column vector of the angular velocity of the motors
$\dot{q}$	Column vector of the time derivative of the generalized coordinate
$\dot{q}_r$	Column vector of the time derivative of the new generalized coordinate
$\dot{X}$	Column vector of the velocities of the platform
η	Column vector of the null space of the matrix W
Γ	Column vector calculated as $\Gamma = H^{-1} F$

$\hat{l}_i$ Column vector of the unit vector in the direction of l_i

λ Column vector of the multipliers of Lagrange

μ An arbitrary column vector

Ψ_p Column vector of the orientation of the platform

θ Column vector of the position of the actuators

$\tilde{q}_i$ Column vector of the generalized coordinate of each cable calculated as $\tilde{q}_i = \begin{bmatrix} x & w_i & \varphi_i \end{bmatrix}^T$

C Column vector of the partial derivative of the kinetic energy

C_r Column vector of the partial derivative of the kinetic energy relative to q_r

e_i Column vector of the position of the point B_i in $\mathcal{R}_p$

F Column vector of the equations of the right side of the equation (3.18)

F_1 The bloc (1,1) of the matrix F with dimension $(3n + 3 \times 1)$

F_2 The bloc (1,2) of the matrix F with dimension $(2n \times 1)$

F_p Column vector of the external forces applied on the platform

f_p Column vector of the force exerted at the center of mass O_p of the platform

h Column vector of the constraints equations

J_i Row vector of the inverse kinematic jacobian matrix

$l(X)$ Column vector of the cable lengths

$l(X_0)$ Column vector of the initial unwounded cable lengths

P_p Column vector of the position of the platform

P_{A_i} Column vector of the position of the exit point A_i of the cable $\#i$

P_{B_i} Column vector of the position of the attachment point B_i of the cable $\#i$ at the platform

Q Column vector of generalized forces

q Column vector of the generalized coordinate that is presented as $q = \begin{bmatrix} x_p & y_p & \alpha \end{bmatrix}^T$ in section (2.3.5) and presented as $q = \begin{bmatrix} q_1^T \dots q_n^T & x_p & y_p & \alpha \end{bmatrix}^T$ in section (3.2)

q^* Column vector of the desired trajectory and is presented as $q^* = \begin{bmatrix} x_p^* & y_p^* & \alpha^* \end{bmatrix}^T$

q_0 Column vector of the generalized coordinate in the center on the workspace

q_e Column vector of the operation point

q_i Column vector of the generalized coordinate of each cable calculated as $q_i = \begin{bmatrix} l_i & w_i & \varphi_i \end{bmatrix}^T$

Q_r Column vector of the generalized forces relative to q_r

q_r Column vector of the new generalized coordinate

T Column vector of the cable tensions

T Column vector of the tensions of the cables

u_1 Column vector that ensures the cable's tensions remain positive

V_p Column vector of the velocity of the platform

X Column vector of the pose of the platform

X_0 Column vector of the initial pose of the platform

Résumé de thèse en français

Contexte et problématique

L'idée et l'histoire de la robotique remontent au monde antique, mais la première apparition du mot robot remonte à la pièce de l'écrivain tchèque Karl Chapek "Rossum's Universal Robots" (R.U.R) publiée en 1920, où le terme a été inventé par son frère Josef du mot tchèque "robota", signifiant travail ou servage.

Au cours de la deuxième révolution industrielle, la capacité de l'ingénierie structurelle à contrôler l'électricité a été développée afin que de petits moteurs puissent alimenter des machines. Les premières utilisations des robots modernes ont eu lieu dans les usines en tant que robots industriels. En 1954, George Devol a déposé une demande de brevet pour la fabrication d'un bras robotique, qui a été accordé en 1961. En coopération avec Joseph Engelberg, George Devol a ouvert une entreprise pour produire des robots sous le nom d'Unimation, ce qui signifie mouvement, en 1956. Les robots créés étaient basés sur le modèle de base de George Devol et ces robots étaient appelés à l'époque des machines de transport programmées car leur fonction était de transporter des objets d'un endroit à un autre. Victor Scheinman a inventé le premier bras robotique articulé composé de six articulations rotatives à l'Université de Stanford en 1969. Cette invention a permis l'utilisation de robots dans des applications plus complexes telles que les opérations de soudage et d'assemblage. Au fil des ans, plusieurs catégories de robots ont été créées en fonction du type de leurs structures, de leur articulation et de leur espace de travail.

Les manipulateurs parallèles ont été introduits à la fin des années 1970 et ont révolutionné de nombreux secteurs industriels. Ces manipulateurs se caractérisent par une disposition parallèle de moteurs et de segments rigides fixés à une plate-forme. L'architecture Gough-Stewart est l'architecture de robot parallèle la plus courante (Jianjun et al. (2013)).

Depuis quelques années, une nouvelle catégorie de robots parallèles est apparue, appelée robot parallèle à câbles (CDPR), où les câbles remplacent les liaisons rigides. Un robot à câbles parallèles est équipé d'une plate-forme (ou d'un effecteur) reliée à une base par des câbles, avec laquelle il est possible de déplacer la plate-forme en modifiant sa longueur. Cette architecture particulière combine des robots parallèles et les propriétés des câbles, ce qui conduit à des mécanismes efficaces.

Ces robots ont de nombreuses caractéristiques intéressantes, telles qu'un rapport charge utile sur poids élevé (Albus et al. (1992)), des structures légères avec une faible inertie de mouvement et un grand espace de travail comme présenté par Cone (1985). Comme les actionneurs de ces robots sont fixés à la base, la masse et l'inertie de la plate-forme mobile sont réduites, ce qui rend ce type de robot parfait pour une utilisation dans des applications à grande vitesse (Kawamura et al. (1995)). Les principaux problèmes rencontrés lors de l'étude des CDPR sont la nature physique

1

des câbles qui ne permettent de produire que des efforts unilatéraux: les câbles ne peuvent exercer qu'une force de traction et doivent donc être maintenus sous une tension positive pendant le fonctionnement. De plus, les câbles sont souples, ce qui introduit des vibrations transversales qui peuvent entraîner des imprécisions et retarder le positionnement de la plate-forme. Il est donc nécessaire d'atténuer ces vibrations, pour atteindre des performances satisfaisantes. De plus, en augmentant la bande passante des CDPR, les correcteurs classiques basés sur un modèle de robot à câbles à segments linéaires deviennent moins efficaces et n'offrent plus les performances souhaitées.

Objectifs de la thèse

Dans cette thèse, deux objectifs principaux sont explorés : premièrement, une analyse systématique de la modélisation, de la simulation et de la synthèse des modèles d'équations différentielles-algébriques (EDA), et deuxièmement, surmonter le problème de la flexibilité des câbles en contrôlant le mouvement de la plate-forme tout en assurant l'amortissement. En raison des complexités liées à la synthèse des modèles DAE, le premier objectif n'a pas donné lieu à une contribution, alors que le second objectif a donné lieu à une contribution scientifique. Cette contribution est réalisée en deux étapes : modéliser la flexibilité du système et améliorer son amortissement par une approche de synthèse de loi de commande.

Modélisation de robot à câble flexible

Les robots parallèles à câbles sont composés de points d'attaches reliés à une plate-forme par l'intermédiaire des câbles enroulables (voir Figure 1). Ce type de robot possède plusieurs avantages tels que le faible coût de construction et de maintenance ainsi que le déplacement rapidement dans des grands espaces.
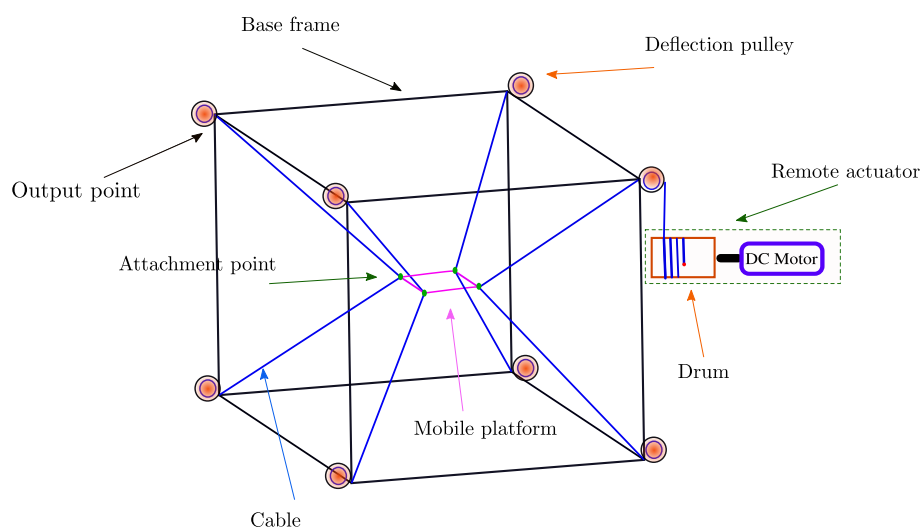
Figure 1: Structure d'un robot parallèle à à 8 câbles et 6 degrés de liberté.

Dans la littérature sur la modélisation des robots à câble, différentes hypothèses

sont envisageés. Dans cette thèse, nous avons modélisé la flexibilité des câbles en considérant l'approche des modes supposés et nous contribuons à étendre le modèle présenté par Ayala Cuevas et al. (2017) pour obtenir un modèle dynamique 2D avec 3 degré de liberté en utilisant le formalisme d'Euler-Lagrange.

Dans la thèse, on considère un robot parallèle plan à 4 câbles flexibles (Figure 2).
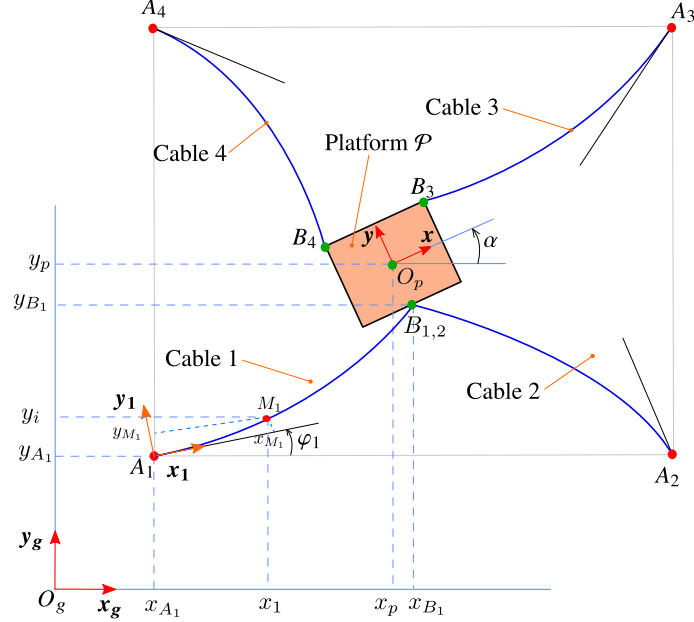
Figure 2: Représentation d'un robot parallèle plan à 4 câbles flexibles.

Chaque câble est considéré comme flexible, inextensible et caractérisé par trois variables : sa longueur l_i (pour le câble $\#i$, ou $i = 1, 2, 3, 4$), son orientation au point d'attache φ_i et son mode de flexibilité w_i obtenu en utilisant la méthode des modes supposés pour modéliser le déplacement transversal.

Le système est paramétré avec un vecteur de coordonnées généralisées q de $3n+3$ variables de position, ses variables sont les trois paramètres qui caractérisent chaque câble (longueur, mode de flexibilité et orientation) ainsi que les coordonnées de position (x_p, y_p) et la orientation α de la plate-forme où n est le nombre de cables considéré.

Les robots parallèles à câbles sont des mechanismes en chaîne cinématique fermée car la position de chaque extrémité de câble $(x_{pi}(\bar{q}_i), y_{pi}(\bar{q}_i))$ coïncide avec la position de point d'attache de la plate-forme (x_{B_i}, y_{B_i}). Les équations de la fermeture géometrique correspondantes forment l'ensemble de deux contraintes algébriques pour chaque câble :

$$h(q) = 0 \quad \Leftrightarrow \quad \begin{cases} x_i(\bar{q}_i) - x_{B_i} = 0 \\ y_i(\bar{q}_i) - y_{B_i} = 0 \end{cases} \quad (i = 1, ..., 4) \tag{1}$$

avec $\bar{q}_i = \left[l_i, w_i, \varphi_i\right]^T$.

La flexibilité des câbles a été modélisée en considérant la méthode des modes supposés. Nous avons choisi une forme polynomiale pour représenter cette flexibilité. Le nombre de modes de flexibilité est estimé à partir de l'observation. En considérant un seul mode de flexibilité w_i, le déplacement selon x_i peut s'exprimer comme suit :

$$\delta y_{M_i}(x,t) = \frac{x^2}{l_i} w_i(t) \qquad (i = 1, \ldots, 4). \tag{2}$$

La position de point mobile M_i dans le repère global $\mathcal{R}_g = (O_g, \boldsymbol{x_g}, \boldsymbol{y_g})$ peut donc s'exprimer comme:

$$\begin{cases} x_i(\tilde{q}_i) = cos(\varphi_i)\, x_{M_i} - sin(\varphi_i)\, y_{M_i} + x_{A_i} \\ y_i(\tilde{q}_i) = sin(\varphi_i)\, x_{M_i} + cos(\varphi_i)\, y_{M_i} + y_{A_i} \end{cases} \quad \text{for } i = 1, \ldots, n \tag{3}$$

où $\tilde{q}_i = \begin{bmatrix} x & w_i & \varphi_i \end{bmatrix}^T$ et $(x_{M_i}, y_{M_i}) = \left(x - \frac{1}{2} \int_0^x (\frac{\partial\, \delta y_{M_i}(x,t)}{\partial x})^2\, dx, \delta y_{M_i} \right)$ est la postion de point M_i dans le repère local $\mathcal{R}_i = (A_i, \boldsymbol{x_i}, \boldsymbol{y_i})$.

Choix de la position des points d'attache

Nous avons effectué une étude l'atteignabilité de l'espace de travail qui vise à choisir le design de la plateforme (les points d'attache) qui augmente la manoeuvrabilité en orientation après avoir constaté sa faiblesse dans le cas d'une la configuration (1) (voir Figure 2.12), et aussi d'assurer la stabilité de la plate-forme pendant le mouvement car notre plate-forme flotte dans l'espace, ce qui la rend sujette à basculer hors plan $x - y$.

Les résultats de l'étude pour les différentes géométries sont illustrées dans le tableau (1).
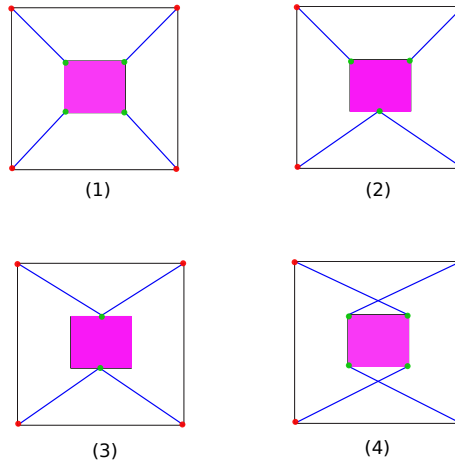
Figure 3: Différents scénarios pour différents points d'attache de câbles.

D'après les résultats présentés dans le tableau (1), la géométrie (2) est considérée pour notre étude, car la plate-forme est stable durant le mouvement et aussi cette configuration offre une meilleure manoeuvrabilité en orientation.

Validation de modèle geometrique

La validation expérimentale a été réalisée à l'aide d'un prototype de robot à câble plan appelé prototype INCA qui existe dans le laboratoire ICube. Lors de l'exploitation

	Orientation maximale
Géométrie (1)	Une orientation qui ne dépassent pas $\pm 2,29^o$
Géométrie (2)	Une orientation jusqu'à $\pm 30^o$
Géométrie (3)	Une orientation jusqu'à $\pm 42.39^o$ mais la platform est unstable
Géométrie (4)	Une orientation jusqu'à $\pm 85,94^o$ mais la platform est unstable

Table 1: L'orientation maximale que les configurations dans la Figure (3) peuvent effectuer

du prototype INCA, nous avons observé que les câbles sont flexibles. La validation a pour objectif de calculer les positions des points du câble dans le plan INCA à partir d'une vidéo et de les comparer avec le modèle de câble flexible que nous avons proposé lors de la modélisation (dans l'équation 3). Pour effectuer cette étude, une vidéo du mouvement du câble a été prise pendant le fonctionnement du robot. Dans un premier temps, les points du câble ont été extraits (voir Figure 4) en utilisant les outils de traitement d'image (dans le plan de l'image), puis les positions de ses points ont été tranformés dans le plan de l'INCA en utilisant une matrice de projection (en éffectuant une calibration de la caméra) et comparées au modèle géométrique considéré durant la modélisation en utilisant l'approche des moindres carrés. Les résultats montrent que le modèle géométrique de câble flexible proposé représente bien le comportement réel du câble (voir Figure 5).
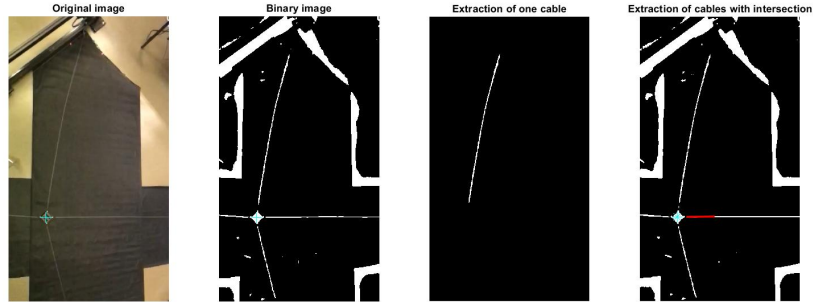
Figure 4: Extraction de câble à partir d'un flux vidéo (a. image originale b. image binaire c. extraction d'un câble d. extraction des câbles avec intersection).

Modèle dynamique à câble flexible

Le modèle dynamique a été obtenu en utilisant l'équation d'Euler-Lagrange avec des multiplicateurs adaptée aux systèmes dynamiques à contraintes géométriques. Le modèle dynamique a été obtenu comme :

$$\dot{M}(q,\dot{q})\dot{q} + M(q)\ddot{q} = \underbrace{\frac{\partial K(q,\dot{q})}{\partial q}}_{C} + Q(q,\tau) + A(q)^T\lambda \tag{4}$$

où M est la matrice d'énergie cinétique, K est l'énergie cinétique, τ est le vecteur des couples des enrouleurs, Q est le vecteur des forces généralisées, $\lambda = \begin{bmatrix} \lambda_1, \ldots, \lambda_{2n} \end{bmatrix}^T$ est le vecteur des multiplicateurs de Lagrange, A est la matrice jacobi-
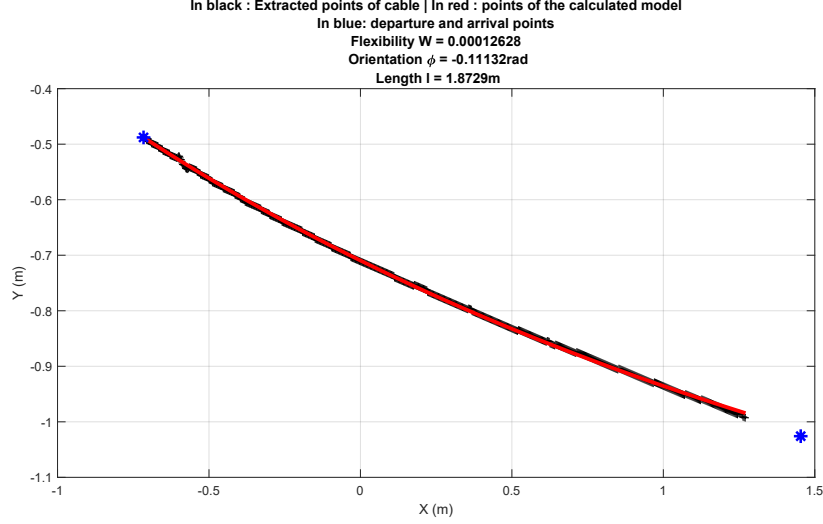
Figure 5: La reconstruction du câble à partir de la vidéo

enne des contraintes géométriques (dans l'équation 1) avec q vérifiant les contraintes cinématiques $\dot{A}\,\dot{q} = 0$. La matrice M est inversible dans l'espace de travail.

En combinant la dérivé par rapport au temps de contraintes geometriques et le modèle dynamique (4), nous avons obtenu un modèle algèbro-différentielle représenté comme:

$$\underbrace{\begin{bmatrix} M(q) & -A(q)^T \\ A(q) & \mathbb{O} \end{bmatrix}}_{V} \begin{bmatrix} \ddot{q} \\ \lambda \end{bmatrix} = \underbrace{\begin{bmatrix} C(q, \dot{q}) + Q(q, \tau) - \dot{M}(q, \dot{q})\,\dot{q} \\ -\dot{A}(q, \dot{q})\,\dot{q} \end{bmatrix}}_{F} \tag{5}$$

Transformation de modèle EDA au modèle EDO

Comme le but de la thèse est de synthétiser un correcteur $\mathcal{H}_\infty$, alors une linéarisation du modèle dynamique obtenu est primordiale. Dans la thèse, nous avons suivre deux approches pour linéariser le modèle DAE qui n'ont pas abouti en raison de la non-commandabilité et de la non-observabilité du modèle linéaire obtenu. Ensuite, le modèle dynamique a été transformé en un modèle donné sous la forme d'un ensemble d'équations différentielles ordinaires (EDO) pour éviter la dépendance entre les variables qui causent la non-commandabilité et la non-observabilité.

Ce modèle EDO linéaire d'ordre minimal est obtenu en trasformant la paramétrisation d'origine q en un ensemble réduit de paramètres q_r. La première étape consiste à supprimer les contraintes géométriques en exprimant certaines variables en fonction d'autres. Ceci a été fait en exprimant les longueurs l_i et les orientations φ_i des câbles en fonction de la pose de la plate-forme $X = \begin{bmatrix} x_p & y_p & \alpha \end{bmatrix}^T$ et les modes de flexibilité w_i comme suit :

$$l_i(w_i, X) = 3\sqrt{\frac{(x_{B_i} - x_{A_i})^2 + (y_{B_i} - y_{A_i})^2}{9 - 3\,w_i^2 + 4\,w_i^4}} \tag{6}$$

$$\varphi_i(w_i, x_p, y_p, \alpha) = atan2(y_{B_i} - y_{A_i}, x_{B_i} - x_{A_i}) - \beta_i \tag{7}$$

avec :

$$\beta_i = atan2(\delta y_i, l_i - \delta x_i) \tag{8}$$

où (x_{B_i}, y_{B_i}) sont les positions des points d'attache de la plate-forme et (x_{A_i}, y_{A_i}) sont les positions de points d'attache des câbles avec la base.

Ainsi, le modèle dynamique (5) a une représentation différentielle ordinaire équivalente :

$$M_r(q_r)\,\ddot{q}_r = \underbrace{\frac{\partial T_r(q_r, \dot{q}_r)}{\partial q_r}}_{C_r} + Q_r - \dot{M}_r(q_r, \dot{q}_r)\,\dot{q}_r. \tag{9}$$

avec $C_r = \frac{1}{2}\dot{q}_r^T\left(\nabla_{q_r} M_r\right)\dot{q}_r$, $Q_r = -\frac{1}{r}\left(\nabla_{q_r} l_i\right)$ and $q_r \in \mathbb{R}^{n+3}$.

La linéarisation du modèle différentielle ordinaire autour de centre de l'espace de travail fournit un modèle linéaire commandable et observable.

Synthése $\mathcal{H}_\infty$ et simulation

Les robots parallèles à câbles sont soumis aux variations de leur propre inertie ainsi qu'aux perturbations extérieures, ce qui justifie la nécessité de choisir une commande pouvant assurer une bonne robustesse. La commande $\mathcal{H}_\infty$ est une méthode de synthèse qui traite des systèmes multivariables linéaires dans le but d'assurer les performances souhaitées tout en assurant de bonnes propriétés de rejet des perturbations, de suivi de trajectoire et de robustesse vis-à-vis de les dynamiques négligées.

La synthèse $\mathcal{H}_\infty$ a été introduite par Zames et Helton à la fin des années 1970 et au début des années 1980 en (Helton (1978), Zames (1981)). Cette méthode a de multiples applications dans des domaines très variés et est devenue ces dernières années l'une des méthodes de la commande robuste.

Le contrôle des robots à câbles s'effectue généralement en deux étapes : le contrôle de la position de la plateforme et la gestion des tensions des câbles. Le plus souvent, ces deux étapes sont réalisées séparément. La contribution scientifique de la thèse est de développer un schéma de synthèse $\mathcal{H}_\infty$ pour les robots à câbles planaires à 3 degrés de liberté prenant en compte la flexibilité des câbles. Ce schéma synthétise un contrôleur $\mathcal{H}_\infty$ qui gère à la fois la tension moyenne des câbles et également la pose de la plate-forme.

La figure 6 montre la forme générale du schéma de synthèse à quatre blocs. Les entrées exogènes et les sorties de performance sont $v_1(t), v_2(t)$ et $(z_1(t), z_2(t))$ respectivement. Des fonctions de pondérations sont imposées sur les signaux d'erreur $W_e(s)$, les signaux de commande $W_u(s)$, les signaux de perturbations $W_d(s)$ et les signaux de référence $W_r(s)$.

Un schéma de synthèse à 4 blocs a été envisagée pour le pilotage de la pose de la plateforme et de la tension moyenne des câbles. Les résultats de la synthèse $\mathcal{H}_\infty$ sont représentés sur la figure 7. Pour les aspects fréquentiels, on voit que tous les gabarits fréquentiels (ligne en pointillé) sont respectés, car ils sont au-dessus des transferts. Nous avons obtenu un correcteur d'ordre 30 et avec un critère de performance en boucle fermée $\gamma = 0.7729 < 1$.

Les résultats de simulation du système non-linéaire commandé par le correcteur $\mathcal{H}_\infty$ obtenu sont présentés sur les Figures 8 à 12.

Les résultats de simulation montrent que le correcteur synthétisé contrôle parfaitement le mouvement de la plate-forme en position et oreintation ainsi que la moyenne des tensions des câbles toute et en rejetant les perturbations en amortis-
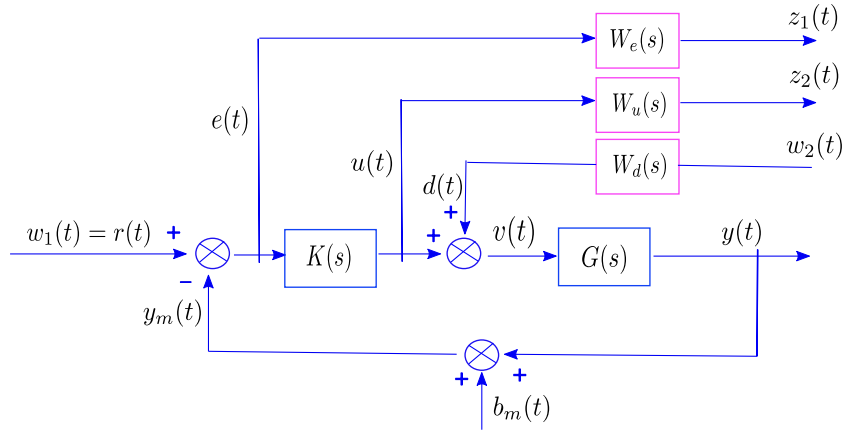
Figure 6: Le schéma de synthèse à quatre blocs.
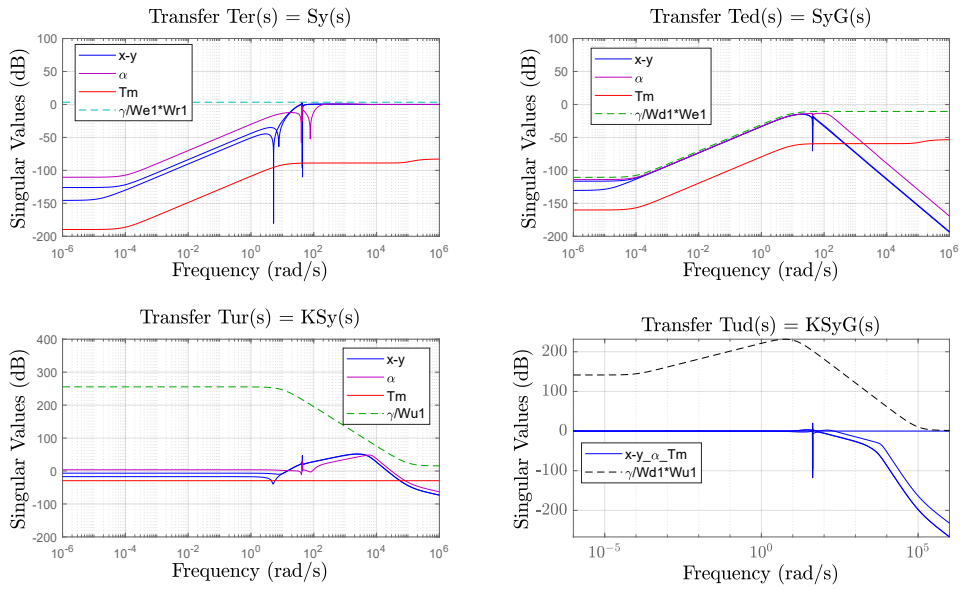
Figure 7: Réponse fréquentielle de la boucle fermée avec les gabarits fréquentiels (pointillé) avec schéma de synthèse $\mathcal{H}_\infty$ à quatre blocs.

sant les oscillations produites par la flexibilité des câbles (la fléxibilité des cables est montrée dans la Figure (12)).

Organisation de la thèse

Après une introduction générale, les différents chapitres de cette thèse sont présentés comme suit :

- Le chapitre 1 est consacré à l'état de l'art des différents travaux ayant étudié les robots parallèles à câble. Dans un premier temps, les différentes approches envisagées pour modéliser ces robots sont rapportées. Puis, la'état de l'art s'attache également à présenter les travaux dédiés au contrôle de ces robots
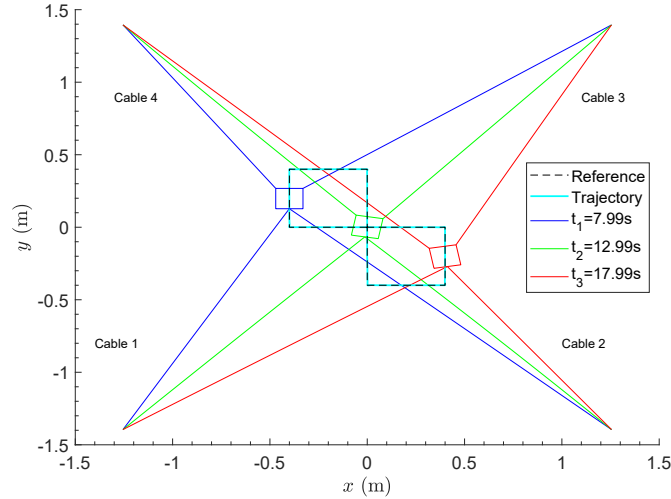
Figure 8: Trajectoires de la plate-forme et des câbles dans le plan $x - y$ avec le correcteur $\mathcal{H}_\infty$.
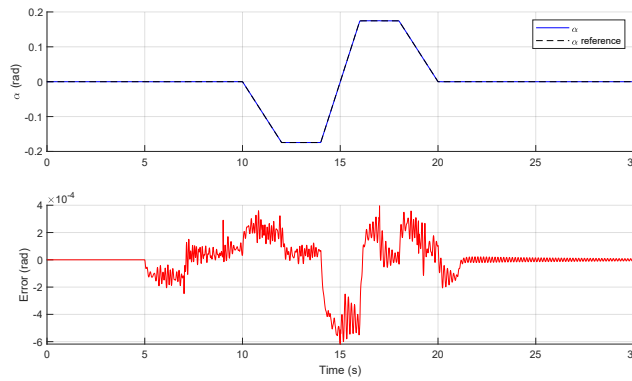
Figure 9: Trajectoires d'orientation de la plate-forme pour le contrôle $\mathcal{H}_\infty$ avec la synthèse à quatre blocs.

en termes de gestion de la tension des câbles et de positionnement de la plate-forme.

- Le chapitre 2 est consacré à la modélisation dynamique des robots à câbles rectilignes en basant sur l'architecture du prototype INCA. Ce modèle permet d'ajuster la loi de commande PID et d'évaluer l'espace de travail.

- Le chapitre 3 présente la forme plus complexe du modèle dynamique qui prend en compte les flexibilités du câble. La linéarisation de ce dernier est calculée algébriquement pour obtenir un modèle convenable pour le contrôle $\mathcal{H}_\infty$.

- Le chapitre 4 présente la méthodologie de synthèse $\mathcal{H}_\infty$. Commençant par une brève présentation des outils mathématiques nécessaires pour effectuer la synthèse $\mathcal{H}_\infty$, le chapitre met également en évidence les différentes approches pour calculer le contrôleur $\mathcal{H}_\infty$.

9
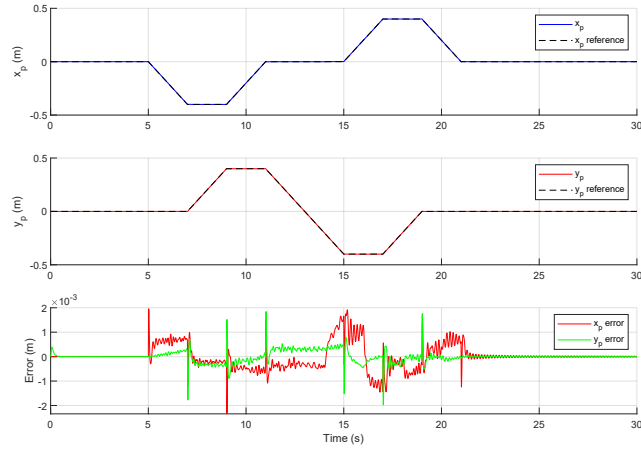
Figure 10: Suivi et erreur des trajectoires x_p et y_p avec correcteur $\mathcal{H}_\infty$ avec la synthèse à quatre blocs.
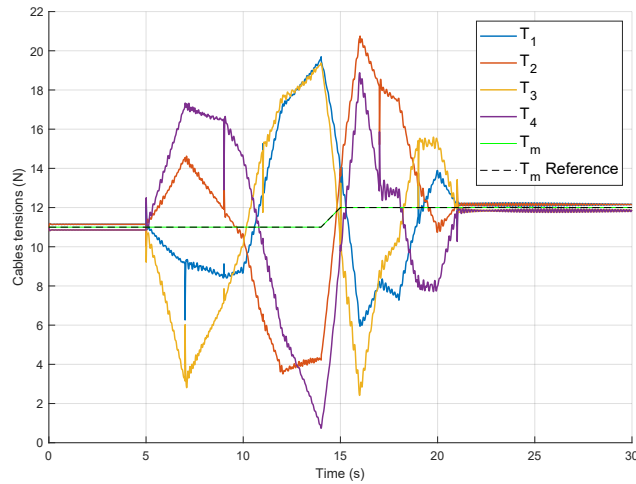
Figure 11: Tensions des câbles et tension moyenne de référence avec la synthèse $\mathcal{H}_\infty$.

- La dernière partie 4.7 est la conclusion à tirer de ce travail et les perspectives envisagées pour accomplir des travaux futurs.
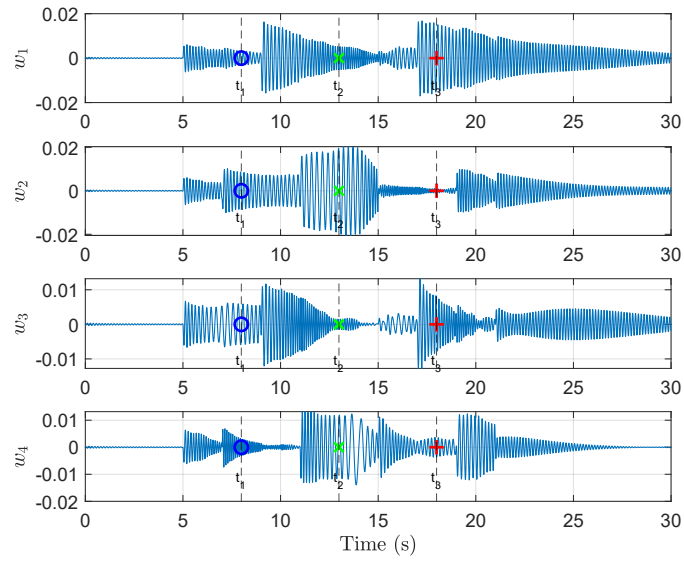
Figure 12: Coordonnées modales pour la flexibilité des câbles avec la synthèse $\mathcal{H}_\infty$.

General introduction

Context and research problem

The idea and history of robotics date back to the ancient world, but the first appearance of the word robot dates back to Czech writer Karl Chapek's play "Rossum's Universal Robots" (R.U.R) published in 1920, where the term was invented by his brother Josef from the Czech word "robota", meaning work or serfdom.

During the second industrial revolution, the ability of structural engineering to control electricity was developed so that small motors could power machines. The first uses of modern robots were in factories as industrial robots. In 1954, George Devol applied for a patent for the manufacture of a robotic arm, which was granted in 1961. In cooperation with Joseph Engelberg, George opened a company to produce robots under Unimation, which means movement, in 1956. The created robots were based on the basic model of George Devol and these robots were called programmed transport machines at that time because their function was to transport objects from one place to another. Victor Scheinman invented the first articulated robotic arm consisting of six rotating joints at Stanford University in 1969. This invention enabled the use of robots in more complex applications such as welding and assembly operations. Over the years, several categories of robots have been created based on the type of their structures, their articulation, and their workspace.

Parallel manipulators were introduced at the end of the 1970s and revolutionized many industrial sectors. These manipulators are characterized by a parallel arrangement of motors and rigid segments attached to a platform. Gough-Stewart architecture is the most common parallel robot architecture (Jianjun et al. (2013)).

In recent years, a new category of parallel robots has appeared, called the cable-driven parallel robot (CDPRs), where cables replace rigid links. A parallel cable robot is equipped with a platform (or an end-effector) connected to a base through cables, with which it is possible to move the platform by modifying its length. This particular architecture combines parallel robots and cables' properties, which leads to efficient mechanisms.

These robots have many interesting features, such as a high payload/weight ratio (Albus et al. (1992)), light structures with low inertia of movement, and a large workspace as presented reported by Cone (1985). As the actuators in these robots are attached to the fixed robot base, the mass, and inertia of the moving platform are reduced, making this type of robot perfect for use in high-speed applications (Kawamura et al. (1995)).

The main problems that have been encountered when studying the CDPRs are the physical nature of the cables that allow producing only unilateral efforts. The cables can only exert a pulling force and must therefore be maintained under a positive tension during operation. Moreover, the cables are flexible, which introduces transverse vibrations that may cause inaccuracy and delay the platform's positioning. It

is therefore necessary to attenuate these vibrations, to reach satisfying performance. Furthermore, by increasing the bandwidth of CDPRs, the classic controllers based on a straight-line segments cable robot model become less efficient and no longer provide the desired performances.

Thesis objectives

In this thesis, two main objectives are explored: first, a systematic analysis of the modeling, simulation, and synthesis of differential-algebraic equation models (DAE), and second, overcoming the problem of cable flexibility by controlling the platform movement while ensuring damping. Because of the complexities involved in the synthesis of DAE models, the first objective did not result in a contribution, whereas the second objective led to a scientific contribution. This contribution is achieved in two steps: modeling the flexibility of the system and improving its damping using a synthesis approach.

- **Modeling of cable's flexibility**

  In the cable robots modeling literature, different hypotheses have been taken into account. In this thesis, we modeled the flexibility of the cables considering the assumed mode approach and we contribute to extending the model presented by Ayala Cuevas et al. (2017) to obtain a 2D dynamic model with 3-DOF using the Euler-Lagrange formalism. This obtained model is a non-linear DAE model.

  As the control purpose in this thesis is to synthesize a linear controller, then a linearization of the non-linear obtained dynamic model is paramount. In this thesis, we present two approaches to linearize the DAE model which did not come to fruition due to the non-controllability and non-observability of the obtained linear model. Then, the dynamic model has been transformed into an ordinary differential equation (ODE) model to avoid the dependency between variables that cause the non-controllability and the non-observability.

- **$\mathcal{H}_\infty$ synthesis**

  The control of the cable robots is generally performed through two steps: controlling the platform's position and managing the cables' tensions. Most often, these two steps are performed separately. The scientific contribution of this thesis is to develop an $\mathcal{H}_\infty$ synthesis scheme for a 3DOFs planar cable robot considering cable flexibility. This scheme synthesizes an $\mathcal{H}_\infty$ controller that manages both the mean tension of the cables and also the pose of the platform.

Thesis organisation

After this general introduction, the different chapters in this thesis are presented as follows:

- Chapter 1 devotes to the state-of-the-art of various works that studied cable-driven parallel robots. First, the different approaches considered for modeling these robots are reported. Then, since the model of the studied cable robot in

this thesis considers flexibility, the approaches for modeling the cable's flexibility are detailed. The state-of-the-art also focuses on presenting the works dedicate to the control of these robots in terms of cable tension management and platform positioning.

- Chapter 2 dedicates to the modeling of parallel straight-line segments cable robots. First, we present in detail the description of the robot prototype that was considered for the experimental study. The robot prototype is the INCA prototype developed by the Haption company. The robot prototype is presented as it served as a set-up for the development and validation of the modeling approaches. Then, based on the same architecture of the prototype, we propose a dynamic model of a planar parallel robot with straight-line segments using the Euler-Lagrange formalism. In addition, it is used to adjust the PID control law and to evaluate the workspace.

- Chapter 3 presents the more complex form of the dynamic model that takes into account the cable's flexibilities. The assumed mode approach is used to model the flexibility and the Euler-Lagrange formalism is used to obtain the DAE dynamic model with 4 cables and 3DOFs. The geometry of the model is validated experimentally by considering a video obtained during the operation of the INCA cable robot prototype. A contribution to the transformation of the DAE model into an ODE model by reducing the geometric constraints is presented in this chapter. The linearization of this latter is calculated algebraically to obtain a suitable model for the $\mathcal{H}_\infty$ control.

- Chapter 4 presents the $\mathcal{H}_\infty$ synthesis methodology. Starting with a brief presentation of the mathematical tools required to perform the $\mathcal{H}_\infty$ synthesis, the chapter highlights also the different approaches to calculate the $\mathcal{H}_\infty$ controller. This chapter contributes to present in detail an $\mathcal{H}_\infty$ synthesis methodology, where we tried different $\mathcal{H}_\infty$ synthesis schemes from two-block scheme up to four-block scheme to chose the suitable for better trajectory tracking and disturbance rejection. The obtain $\mathcal{H}_\infty$ controller manages the mean tension of cables and the 3DOFs of the platform ($(x - y)$ translation and orientation). In addition, the results of the frequency response and the simulation of the closed-loop system controlled with the obtained $\mathcal{H}_\infty$ controller are detailed and discussed. The $\mathcal{H}_\infty$ obtained controller has not yet been validated experimentally.

- Last part 4.7 is the conclusion to draw from this work and the perspectives envisaged to accomplish in future work.

Chapter 1

Literature review on cable robots

1.1 Introduction

In recent years, the CDPRs have played an increasingly important role in the research sector, as well as in industry, where they are used for a large range of applications. Several approaches in the literature have been proposed and studied in the design, the modeling, and control of CDPRs.

The purpose of this chapter is to present a general overview of the description of the CDPRs, their classification by architecture, their applications and their advantages and disadvantages. The current research and problems that face the modeling, control, design and analysis of the workspace of the CDPRs are also detailed.

1.2 Rigid-link serial and parallel robots

Based on their structure, two types of robot architectures can be distinguished: serial robots and parallel robots.

1.2.1 Serial robots

Serial manipulators, also known as robotic arms, are ubiquitous in industry and have the shape of a human arm. These mechanisms are generally made up of rigid links connected by actuated revolute or prismatic joints that provide the end-effector with a certain mobility and a given number of degrees of freedom (DOF). Even though this type of robot is the most studied and used in industry, serial manipulators have several shortcomings such as :

- A limited precision can be caused by the accumulation of errors from link to link.

- A low ratio of load carrying capacity over its own weight result in the need to have bulky and powerful actuators to sustain both weight and dynamic forces of successive links and of the end-effector.

- A low stiffness caused by the open kinematic structure.

Among typical examples of robots with this architecture are the SCARA assembly robot used for pick and place tasks (Figure (1.1a)) or collaborative robots used in close interaction with a human operator (Figure (1.1b)).

(a) FANUC SR-3iA SCARA robot (source: fanuc.eu)

(b) KUKA LBR iiwa cobot (source: kuka-robotics.com)

Figure 1.1: Serial robots (Cobot and SCARA robot)

1.2.2 Rigid-link parallel robots

Rigid-link parallel robots can be described as closed kinematic chain mechanisms consisting of several segments (independent kinematic chains) attached to a base and motorized to support an end-effector or a platform as formulated by Merlet (2012). Thanks to the presence of multiple kinematic chains attached to the base, good load distribution and platform precision is achieved, which is harder to obtain using serial robots. In addition, parallel robots can be operated at high speed but generally have a smaller workspace. These robots can be used as motion simulators or precise positioning devices. The Stewart platform in Figure (1.2a) and the Delta robot in Figure (1.2b) illustrate the concept of parallel robot.
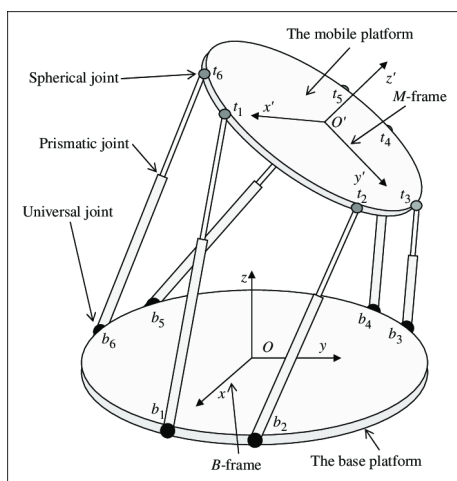
(a) Stewart platform (Jianjun et al. (2013))
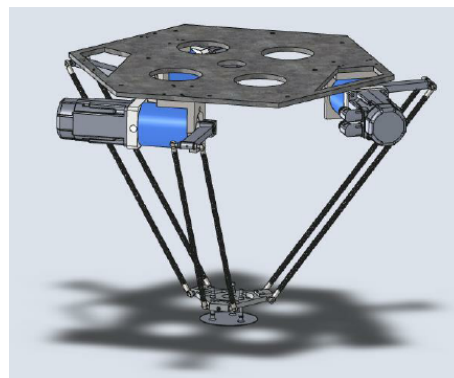
(b) Delta robot (Opl et al. (2012))

Figure 1.2: Parallel robots (Stewart platform and Delta robot)

1.3 Cable-driven parallel robots description

Cable-driven parallel robots are a particular variant of parallel robots where cables replace the rigid-link chains [1] (see Figure 1.3). Each cable connects the base to an attachment point on the movable platform (end-effector). The actuators generally consist of motors coupled to drums to store the cables and are often equipped with deflection pulleys for guiding the cables. By rotating the drums, it is possible to unwind and rewind the cables and then change the position and the orientation of the platform. A cable is a unidirectional transmission element which can only act on the platform in traction (produces only positive tension). Generally, the actuators and the cable deflection pulleys are fixed to the base.
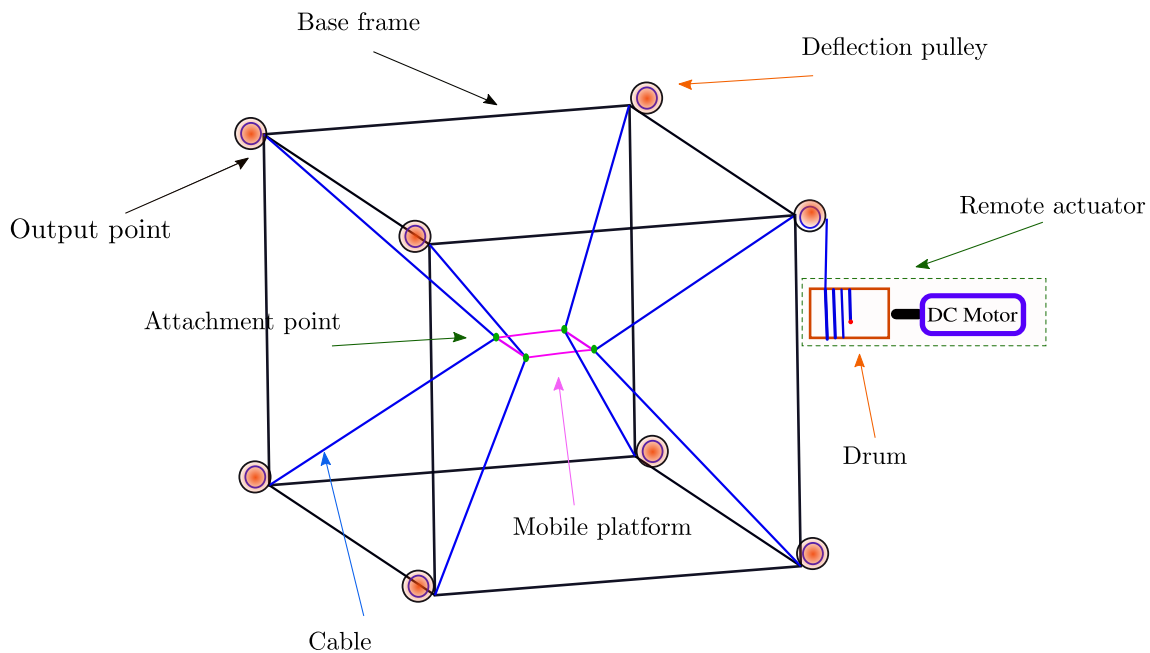
Figure 1.3: Elements of cable-driven parallel robot.

A cable parallel robot's geometry and setup are determined by the choice of the platform and the form of the robot base as well as the place of the attachment points and of the output points (see the cable robot attached to the aerostat BOB in Figure (1.4a) and CAREX prototype in Figure (1.4b)), by the number of cables and their arrangement (suspended and non-suspended CDPRs) and also by number of the degrees of freedom of the platform movement.

1.3.1 Classifications

Suspended and non-suspended CDPR

Two kinds of CDPRs can be reviewed according to the number of cables and how they are arranged.

- The suspended CDPRs are robots where all cables are located above the platform and the equilibrium is ensured by the gravity as virtual cable such as

---

[1]Landsberger and Sheridan are the first to replace the rigid-link of a Stewart platform with cables in the work (Landsberger and Sheridan (1985)).
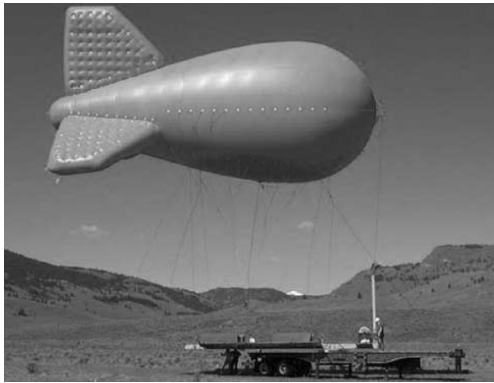
(a) Aerostat with cable robot (Lambert et al. (2007))
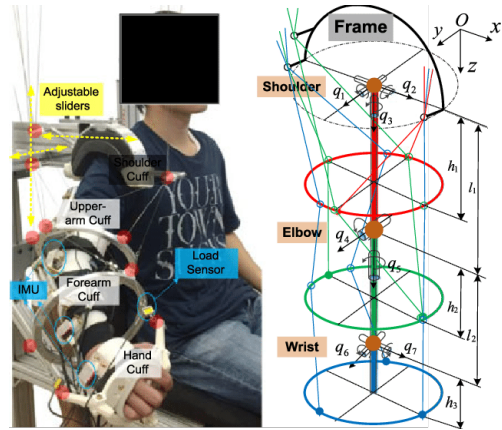
(b) CAREX prototype (Cui et al. (2016))

(c) The INCA 6D prototype

(d) The The MARIONET-CRANE prototype (Merlet and Daney (2010))

Figure 1.4: Cable robot applications

the FAST robot in Figure (1.5a) (Sai et al. (2018)) and CoGiRo robot (with 8 cables and 6 DOFs) in Figure (1.5b) (Gouttefarde et al. (2007)). The robots with this geometry can carry a heavy load charge and the cables are less likely to interfere with other objects in the workspace. However, these robots have a low stiffness along the vertical direction which makes them very sensitive to external disturbances that cause instability and vibrations. In addition, their ability to generate acceleration is limited.

• The non-suspended CDPRs are robots where at least one cable is located below the platform such as IPAnema robot in Figure (1.6a) (Pott et al. (2013)) and the horizontal planar cable robots in Figure (1.6b) (Bayani et al. (2016)) in which the gravity has no effect on the equilibrium of the platform. For these robots, the internal cable forces are increased which implies good stiffness and accuracy of platform positioning. However, the construction costs can be increased due to the use of powerful motors to ensure this rise in cable tensions.
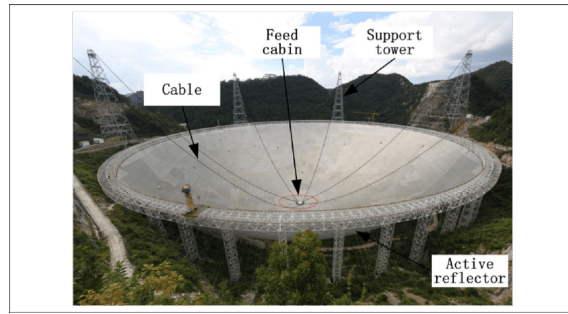
(a) The FAST (Sai et al. (2018))

(b) The CoGiRo robot (source: www.lirmm.fr/cogiro)
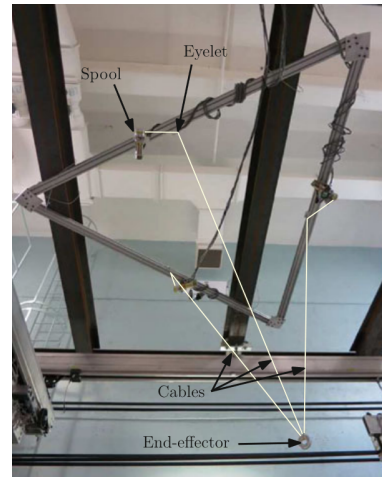
(c) The Laval university prototype (Gosselin (2013))

Figure 1.5: Suspended cable robots
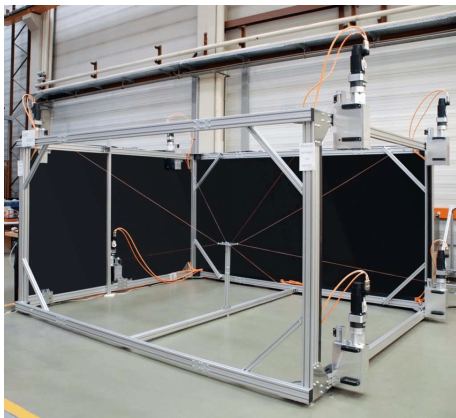
(a) IPAnema robot (Pott et al. (2013))
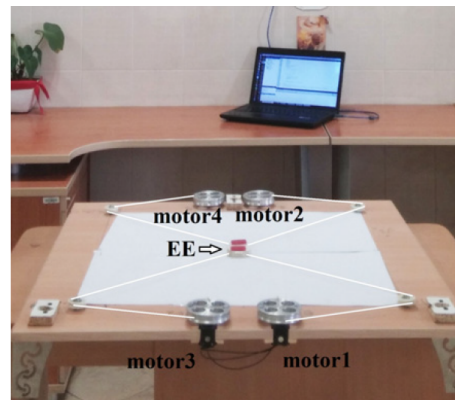
(b) Horizontal planar robot (Bayani et al. (2016))

Figure 1.6: Non-suspended cable robots

Redundant/ Non-redundant actuated CDPRs

The actuation redundancy c is defined based on the number of cables n and the degrees of freedom d of the platform as $c = n - d$. The CDPRs are classified according to their actuation redundancy as outlined below:

- The redundant actuated CDPRs configuration requires more cables than de-

grees of freedom of the platform ($n \geq d + 1$), with this configuration the robot can generate forces in all directions. In this configuration, in general, the pose of the platform is entirely defined by the lengths of the cables. CDPRs in this case are redundant robots with output points located above and below the platform. Non-suspended robots are an example of this configuration such as IPAnema robot (with 8 cables and 6 DOFs) in Figure (1.6a) (Pott et al. (2013)) and SkyCam robot (with 4 cables and 3 DOFs) [2]. The redundancy occurs when adding a cable which improves stiffness, positioning accuracy and safety and can help singularity avoidance which makes these robots well suited for applications requiring high speed and/or accelerations. However, this configuration increases the risk of cable collision.

- In the case of non-redundant actuated CDPRs configuration ($n \leq d$), robots can generate forces only in specific directions. the pose of the platform is not completely defined by the lengths of the cables in the case where we have a less number of cables than degrees of freedom ($n < d$). A preliminary geometrico-static study is proposed by Carricato and Merlet (2010) for this configuration of robots for a crane robot (with 6 DOFs and a number of cables $2 \leq n \leq 5$) and by Mishra and Caro (2021) for a spatial CDPR (with 4 cables and 6 DOFs). The suspended robots are an example of this configuration (for instance see the Laval university prototype (with 3 cables and 3 DOFs) in Figure (1.5c)) (Gosselin (2013)) and the Fast robot (with 6 cables and 6 DOFs) in Figure (1.5a) (Sai et al. (2018)). The suspended CDPRs are suitable for pick and place applications due to their capacity to transport heavy charges as presented by Belzile et al. (2020).

1.3.2 Advantages and disadvantages

Advantages

CDPRs have several interesting advantages due to their cable-based design by overcoming the drawback of rigid-link parallel robots:

- A cable is an easily stored mechanical element with little clutter, reducing interference risks and allowing a clear view of the workspace.

- Due to the low masses and inertia of their kinematic chains, CDPRs can move with higher dynamics.

- Low cost of construction and maintenance.

- A large workspace ranging in size from one meter to hundreds of meters and the ability to work in an encumbered environment.

- A high payload capability for cable compared to robot mass.

- They are easily transportable and reconfigurable due to their simple structure.

- The lightness of the cables.

---

[2]http://www.skycam.tv/.

Disadvantages

Despite all these attractive benefits, the use of cables poses some challenges:

- The workspace is limited by the unilateral actuation (the cables can only produce traction forces in the direction of the cable), by the maximum and minimum cable tensions, and by the collisions of the cables with the platform, or with the environment.

- Cables are deformable continua which leads to a more complex behavior.

- Cable self-collisions add complexity to the path planning of the moving platform.

Despite these disadvantages which create specific problems during the design and control of the CDPRs, many applications of these robots highlight their particular advantages.

1.3.3 Applications

The numerous advantages of cable-driven parallel robots make them popular in a wide range of applications, whether in research or industry. The following are examples of some applications:

- The characteristics of CDPRs make them particularly suitable for **heavy object handling and high dynamics** application. For example, the NIST ROBOCRANE with 6 cables and 6 DOFs presented by Albus et al. (1992) can lift and position objects or power tools weighing up to 1 ton suspended from a conventional crane. The CoGiRo robot which is a highly dynamic robot with a large workspace (15 meters long, 11 meters wide, and 6 meters high) has the capacity to lift loads of 500kg (CoG). Furthermore, the industrial two versions of the IPANEMA that are used for medium to large-scale inspection, handling, and assembly operations (Figure (1.6a) are very appropriate for high velocity and/or acceleration applications. In addition, the FALCON robot can achieve a maximum speed of 13 m/s and is used for ultrahigh speed applications as presented by Kawamura et al. (1995).

- The lightness and flexibility of the cable robots have allowed their use in **neurorehabilitation** applications, whether to identify and optimize human movements or for rehabilitation tasks. For example, cable-driven arm exoskeleton CAREX (Figure (1.4b), the leg rehabilitation system by Homma et al. (2003), and MARIONET-REHAB by Merlet (2010) that is used during rehabilitation tasks to measure the human joint motion.

- The structure of CDPRs has also allowed them to be used in **aeronautical** and **astronautical** applications. By suspending an airplane model in a wind tunnel, the WDPSS-8 robot by Yangwen et al. (2010) simulates the free flight of airplanes and studies aerodynamic behavior. A CDPR has been used by Yiğit et al. (2021) to suspend an omnidirectional aerial manipulator by a spring. For an aeronautical application, the work developed by Mankala et al. (2006) presented an MXER-type tether system that proposed to transfer payloads from low-energy orbits to higher-energy orbits using propellant-free thrust.

- The large workspace of the CDPRs made them eligible to move sensors or cameras for **metrology** applications. For example, the SkyCam robot [3] designed by August Design Company is used to carry a camera in a large stadium for live transmission, and the 6 cable robot presented by Deschenes et al. (2007) that manipulates accurately a camera to capture images along hemispheric trajectories. In addition, the giant FAST prototype with a 500 meters cable length presented in Figure (1.5a) is built for the orientation of radio telescope receivers while the multi-tethered system illustrated in Figure (1.4a) is used for positioning an aerostat.

- Having the ability to be transported and reconfigured, CDPRs can be easily installed on natural disaster sites for **search and rescue operations**. For instance, the proposed system by Bosscher et al. (2005) utilizes vehicles placed around a disaster site to attach sensor equipment to the cable robot, which scans the area for victims as well as the MARIONET-CRANE in Figure (1.4d) (Merlet and Daney (2010)) that is equipped with a thermal camera that can locate a body from more than fifty meters away.

- A CDPR is well suited for **haptic** applications that offer force feedback to the user by exploring a virtual remote environment, where the end-effector is generally a joystick. These include the various generations of SPIDAR robots proposed by (Chamaret et al. (2009), Poitrimol and Igarashi (2020)) for manipulating virtual objects or for manipulating virtual simulators of movements as presented by Perreault et al. (2010). Furthermore, the cable robot prototype INCA 6D that was developed by the company Haption and installed at the ICube laboratory in Strasbourg (see Figure (1.4c)).

- CDPRs have also been considered for **construction** application. For instance, the robots presented by (Barnett and Gosselin (2015), Izard et al. (2017), Chawla et al. (2021)) which are dedicated to the 3D printing.

1.4 Current research and problematics

The disadvantages stated on CDPRs presented in the general introduction and in section (1.3.2) make their study even more complex. The last decades have seen significant progress in research to take into account these technical difficulties on CDPRs. Several approaches in modeling, control, and workspace analysis and design have been presented in the literature and this section briefly discusses these recent works on CDPRs.

1.4.1 Modeling

It is common to ignore the cable behavior when modeling cable-driven parallel robots. Generally, a simplistic modeling approach is considered where the cables are modeled as inextensible rigid straight-line segments with neglected mass in which these segments connect the exit points to the platform such as presented by (Williams II and Gallina (2003), Pham et al. (2009), Filipovic et al. (2014)).

---

[3]http://www.skycam.tv/.

In reality, the cables can only apply tensile force to the platform and are not rigid links. Furthermore, for large workspace applications and under the action of gravity, the cables are subject to deformations due to their length and weight. As a result of these deformations, the platform cannot be precisely positioned. Then, the simplifying assumption of straight and inextensible cables should be reconsidered due to the fact that the dynamics are very fast and the weight of the cables is not negligible compared to the mass of the platform. In some studies, as presented in the following, these deformations and the cable's elasticity were studied.

The force applied to the end of cables can extend it. Then, the cables have been modeled as massless virtual springs with linear stiffness by Weber et al. (2014), with non-linear stiffness by Kawamura et al. (1995), or as tension and damping springs by Bedoustani et al. (2008). Furthermore, the work presented by Sugahara et al. (2022) considers the effect of the viscoelasticity of a synthetic fiber cable.

Some authors consider the mass of cables that introduce the sagging effect and present a static study such as in the works (Kozak et al. (2006), Riehl et al. (2009), Arsenault (2013), Ottaviano et al. (2015)), and also the work of Gouttefarde et al. (2012) that proposes a simplified study to this model. In addition, a dynamic analysis is proposed by (Yuan et al. (2015a), Yuan et al. (2015b)) considering the dynamic stiffness matrix method. Note that the Catenary elastic model that describes the cable sagging was considered first in the domain of civil engineering to construct the cable-stayed bridges as reported by Irvine (1981). Unlike the previously proposed approach, dynamic modeling considering inextensible cables with varying masses was presented by Aref et al. (2008). A stiffness analysis for massless virtual spring cables was presented by (Suilu et al. (2012), Surdilovic et al. (2013)).

In order to take into account the transverse vibrations, the cables are discretized as finite rigid segments interconnected by ball joints including small stiffness and damping effects by Collard et al. (2011), where several models with one to ten segments per cable were compared regarding their static equilibria, their elevated platform behaviors, and their eigen frequencies. In the work of Du et al. (2012) the time-varying cable lengths were discretized as elastic segments and in the work of Du et al. (2014) the finite element method was extended to include the dynamic behavior of the cables. On the other hand, the cables were considered as particular cases of flexible segments modeled using the assumed mode approach as sums of contributions of a given base approximating the shape of flexibility. Considering this approach, the flexible cable dynamic models were driven using the Lagrange formalism by Ayala Cuevas et al. (2017) for 2DOF CDPR, by Godbole et al. (2019) for 1DOF CDPR, and by Saadaoui et al. (2022a) for 3DOF CDPR. Furthermore, the dynamic model was driven by Du and Agrawal (2015) using the Hamiltonian principle for 6DOF. The previous works were considered polynomial and trigonometric function to represent the shapes of flexibility. The Cosserat beam theory model was considered by Tempel et al. (2019) to formulate the deflection configuration through higher-order Bézier curves for the case of elastic-flexible CDPR with time-varying length. In addition to cable robots, this approach is also used to model the soft robotics manipulators, as described by Boyer et al. (2020) and by Armanini et al. (2023), where the dynamic models were obtained considering the Lagrangian or Hamiltonian principle.

Based on the dynamic models presented in this section, different control approaches are synthesized as introduced in the next section.

1.4.2 Control

The synthesis of the controller for CDPRs aims to track well the pose of the platform. During this synthesis, the tensions of the cables must be monitored so that to remain in a region of achievable tensions to reduce the vibrations and the deformations of the cables and increase the stiffness of the mechanism. Then, the control of the CDPRs is divided into two steps, the control of the platform's position and the management of the tensions of cables.

Distribution of cables tension

CDPR's static and dynamic equilibrium is ensured by the cable's tensions. These tensions are determined by the motor torques and the external forces applied to it. In the case of non-homogeneous distribution of cable tensions, these tensions may approach the upper and lower limits, causing the cable to be damaged or relaxed. CDPR control may be lost due to the cable's relaxation which reduces the platform's stiffness. Using a tension distribution algorithm, we are able to control the cable tension in order to avoid this problem. By identifying and tuning cable tensions based on a given criterion, these algorithms can choose a solution among an infinity of possible solutions of tensions that satisfy the criterion. In the case of cable robots with actuation redundancy, solving the distribution of cables tension problem presents a tension distribution algorithm that makes it possible to distribute the tension of the cables while tracking accurately the platform's trajectory is present the work of Lafourcade (2004).

A direct calculation of cable tensions is possible in the case of simple actuation redundancy ($n = d+1$), by proposing a simple calculation algorithm as in the work by Bruckmann et al. (2006), or by determining an analytical solution to the problem in the case of CDPR (with 7 cables and 6 DOFs) in the work of Fang et al. (2004).

The study of the distribution of cable tension is a bit more complex in the case of multiple actuation redundancy ($n > d+1$). In this case, two different approaches can be used:

- **Iterative algorithms**: these methods formulate a constrained optimization problem to choose an optimal admissible tension vector while minimizing a criteria which is in general the norm of the cable tension vector in order to minimize the energy consumption of the actuators. An iterative algorithm with linear criteria solved by linear programming while minimizing the $1-$norm as presented by Vafaei et al. (2010) or while minimizing the ∞-norm as presented by Gosselin and Grenier (2010). These methods are relatively simple but do not ensure the continuity of the tensions in the cables. Other methods with quadratic criteria are solved by quadratic programming, generally minimizing the $2-$norm of the vector of the tensions of the cables as in the work of Agahi and Notash (2009). These methods ensure the continuity of the tensions in the cables.

- **Non-iterative algorithms**: these methods are considered to improve the problem of calculation time of the iterative approach with quadratic programming. Among these methods, we can cite the one based on the projection technique proposed by (Pott et al. (2009)) which calculates an analytical solution by the projection of a desired tension belonging to the set of feasible

tensions. Another non-iterative method proposed by Mikelsons et al. (2008) is based on the construction of the polytope of admissible solutions by determining the vertices of this polytope.

Position and force control

The control strategies have been implemented to manage the forces applied by the platform in contact with an environment and/or manage the position trajectory of this platform.

For the force control, we mention, the admittance control law coupled with a closed-loop velocity controller proposed by Fortin-Côté et al. (2014) for the haptic interfaces based on cable-driven parallel mechanisms by introducing adaptations for smooth surfaces and sharp edges.

The aim of the hybrid position-force control is to apply process forces in a programmable direction to a surface while the movement perpendicular to the force vector is position controlled as formulated by Kraus et al. (2015). For instance, this hybrid control has been applied in the case of the 9-cable-driven parallel Mechanism presented by Yi et al. (2019) to adjust the cable force precisely while controlling the cable length, and in the case of redundant pneumatic muscles-cable-driven ankle rehabilitation robot presented by Liu et al. (2022) to keep all pneumatic muscles and cables in tension.

Several position control approaches have been reported in the literature. The adaptive control was considered with CDPRs with uncertainties by Babaghasabha et al. (2015) for a control strategy that does not require a measurement of the end-effector acceleration and keeps all cables in tension, and by Harandi et al. (2021) while separating the determinant and adjugate of Jacobian matrix to represent them into a new regressor form. The model predictive control (MPC) proposed by Katliar et al. (2017) to control the acceleration and angular velocity of cable robot-based motion simulator and to improve the prediction of the reference trajectories of the simulator, whereas linear variant MPC has been used by Xiang et al. (2020) to plan dynamic transition trajectories to general periodic motions that extend beyond the static workspace of the mechanism for a 3DOFs cable-suspended parallel robot. The work presented by Qian et al. (2021) proposes an adaptive sliding mode impedance control (ASMIC) algorithm for a 6DOFs compliant upper limb rehabilitation robot (ULRR) driven by series elastic actuators (SEAs) to reduce impedance error, whereas a second-order sliding mode control based on projection neural network was designed by Rahmani et al. (2020) for position tracking of a parallel cable robot to control torque generation. This approach was based on a synchronization control strategy for a good disturbance rejection as presented in the work of Jia et al. (2020). A kinematic approach for the control-based on a cascaded architecture has been presented by Chellal et al. (2015) to ensure an accurate end-effector positioning and management of the cable's tension of parallel cable robot with 6DOFs.

Some position control strategies have been implemented for the CDPRs to reduce the vibration and properly track the trajectory of the platform and reject the disturbance. The work presented by Yousefzadeh and Tourajizadeh (2017) proposed an approach that considers only the feedback from the joints to reduce vibration in the case of a 6DOFs cable-suspended parallel robot with elastic cables, in addition, a filtration method is employed to prevent excitation of natural modes. A model predictive control was designed by Khayour et al. (2020) to reject the vibration on

26

elastic cable-driven parallel robots by computing the control law and allocating the control signals to the available actuators by assigning their binary on-off states. A neuro-fuzzy intelligent control algorithm was designed by Ahouee et al. (2017) to better detection of reference routes and model in simulation a 3DOFs planar CDPRs with elastic cables. The $\mathcal{H}_\infty$ control strategy is known for their ability to manage well flexibility. Thus, the $\mathcal{H}_\infty$ based controller have been designed for flexible links by Farruggio and Menini (2000) and by Yazdanpanah (1997). Then, this strategy has been extended in the case of CDPRs, as the work presented by Chellal et al. (2017) to limit the inappropriate effects of cable flexibility for 6DOFs CDPRs. The $\mathcal{H}_\infty$ control strategy has been considered also in other robotic applications as presented by Zasadzinski et al. (1997) for its ability to produce reduced-order controllers.

The control in the joint space is performed considering the motor position or cable length references using the inverse geometric model, such as in the work proposed by Ming and Toshiro (2004) where a PD controller was designed and combined with a non-linear term in the joint space to compensate the dynamics of the platform, or as the work of Gholami et al. (2008) where a PD controller was designed with a feed-forward loop to satisfy the required tracking performance.

The control in the operational space is performed by estimating the current pose of the platform from the robot measurements of the motor positions, such as a design of a PD controller with two feed-forward loops in the operational and joint space allowing the separate compensation of the dynamics of the platform and the actuators as presented by Lamaury and Gouttefarde (2013).

1.4.3   Design and workspace analysis

In the CDPR literature, most considered CDPR prototypes were designed based on intuition and experience, such as the Falcon robot presented by Kawamura et al. (1995) and the giant robot LAR presented by Bouchard and Gosselin (2007). However, some design methods have been proposed for optimizing the geometry of CD-PRs, taking as a criterion the reachable workspace as presented by Azizian and Cardou (2012) or the capacity to generate forces as proposed by Perreault and Gosselin (2008).

The workspace of a parallel cable robot is defined by the set of poses where the geometric constraints due to the maximum cables' lengths and static constraints that ensure positive cable tensions and the static and dynamic equilibrium of platform must be satisfied as formulated by Chellal (2016). Several workspaces and equilibrium conditions have been studied in the literature and they are described as follows:

Wrench-closure workspace (WCW)

The WCW is an approach that is based on the static equilibrium of the platform. The whole set of platform poses belongs to the WCW if the static equilibrium of the platform is assured by positive cable tensions without any upper limits. For example, a determination and analysis of the wrench-closure workspace of planar parallel have been presented by Gouttefarde and Gosselin (2004) and by Gouttefarde and Gosselin (2006) to determine the constant-orientation wrench-closure workspace by means of a graphical representation of its boundary and to disclose the parts of the reachable workspace which belong to the WCW, respectively.

Wrench-feasible workspace (WFW)

This approach is based on the feasible static equilibrium of the platform. The WFW is the set of all platform poses for which cables can balance any wrench among a given set of wrenches that can be applied to the platform while cable tensions are limited by given upper and lower limits. The lower T_{min} and upper T_{max} limits of the cable tension are defined to avoid the relaxation and damage of the cables respectively. For instance, Gouttefarde addressed the problem of the determination and analysis of the WFW of n-degree-of-freedom parallel mechanisms in the works (Gouttefarde et al. (2007), Gouttefarde et al. (2011)) by given an approximation of a set of n-dimensional boxes such that each box of the set is fully included in the WFW.

Static Equilibrium Workspace

The Static Feasible Workspace is a particular case of the WFW, where all poses of the platform can be reached by compensating only its weight and without any external wrench applied to it. For instance, the work presented by Alp and Agrawal (2002) presents a static equilibrium analysis for a 6-cable-suspended parallel robot and the work presented by Pusey et al. (2004) aims to tackle some aspects of the optimal design of a 6DOFs cable robot by addressing the variations of the workspace volume and the accuracy of the robot using different geometric configurations, different sizes, and orientations of the moving platform.

Dynamic workspace

As it was reported by Barrette and Gosselin (2005), the dynamic workspace is defined with the set of all poses and dynamic conditions (accelerations) for which all cables are in positive tension. The work proposed by Gagliardini et al. (2018) presents a more general definition of the dynamic feasible workspace (DFW) and, in the same work, defined the Required Wrench Set (RWS) as the set of wrenches that cables need to apply on the moving platform to achieve dynamic equilibrium.

1.5 Conclusion

An overview of the cable robot literature has been presented in this chapter. First, we discussed the difference between serial and parallel robots and then we introduced in detail the description of the cable-driven parallel robots. The classification of these robots has been presented based on their geometry and their actuation redundancy. Moreover, we mentioned the advantages and disadvantages of the CDPRs and presented their different applications.

Additionally, several approaches for the modeling and the control of the CDPRs have been reported in the literature. Furthermore, we have provided a description of the different algorithms used for cable tension distribution and the analysis of the workspace. In the next chapters (2 and 3), we present the different hypotheses and approaches of the modeling that have been considered to solve the problematic in this thesis.

Chapter 2

Dynamic modeling of a straight-line segments cable-driven parallel robots

2.1 Introduction

This chapter starts with a description of the hardware and software of the cable robot prototype. This prototype is developed by the Haption company and is located in the ICube laboratory. In its original version, the robot prototype includes 8 cables. For our study we have attached the cables so as to obtain a planar robot with 4 cables. Having an experimental system served us as a basis for conceptualizing and putting forward modeling hypotheses, as well as performing experimental tests to geometrically validate the theoretical model afterward.

Several approaches and assumptions are considered and presented in the literature to model cable-driven parallel robots. This chapter presents a dynamic modeling methodology for planar CDPRs with n cables using the Euler-Lagrange formalism. The dynamic model was developed based on a simplistic modeling approach that assumes the cables are straight-line segments without mass. This modeling hypothesis allows us to study and analyze the dynamics of CDPRs and it was presented in this chapter in order to be used for the study of the reachability of the workspace. Furthermore, this model is also considered for the design of PD and PID controllers.

2.2 Experimental system description

The experimental system considered for the study in this thesis is an INCA prototype with a planar geometry. The Haption company[1] developed the INCA prototype for manipulating objects in virtual environments. This prototype is a force feedback haptic interface driven by cables and it was inspired by work of Hirata and Sato (1992): the SPIDAR. It owns a large workspace and high forces and is considered for the following applications: ergonomic studies, accessibility studies, and assembly simulation.

During this thesis, the INCA 6D prototype is retrofitted to a horizontal plane robot with four cables and a platform to address handling problems (see Figure 2.1). In this section, we describe the hardware and software architecture of the planar INCA robot.

---

[1]https://www.haption.com/fr.
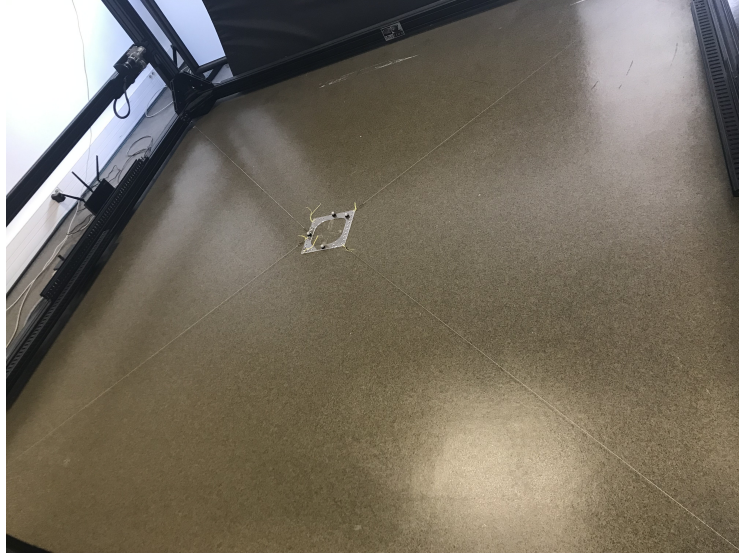
Figure 2.1: The INCA plane robot with 4 cables and platform.

The INCA 6D robot (see Figure 1.4c) consists of a cubic base of about 2.800 m side with 8 cables to move the platform and 8 other cables that are connected to the return springs to ensure pre-tension in the cables attached to the platform. In the case of our study for a planar robot, only 4 displacement cables are used to move the platform.

2.2.1   Platform

A square platform of 20 cm and weighing 130 g is attached by 4 cables and is located in the center of the workspace (see Figure 2.2), the platform is equipped with 4 markers.

Figure 2.2: The platform of the INCA

2.2.2   Actuators

In the case of the planar robot, 4 cables are fixed at the 4 vertices of the cubic base by the mean of the output points. Each outpoints is connected to an actuator (see Figure 2.3) that consists of a DC motor of type Maxon 144877, to mechanize two kinds of drums: the winch drum that stores the cable driven towards the platform and the coaxial tension winch drum that stores another cable driven towards its free end to a linear spring, while the other end of the spring remains fixed to the base.
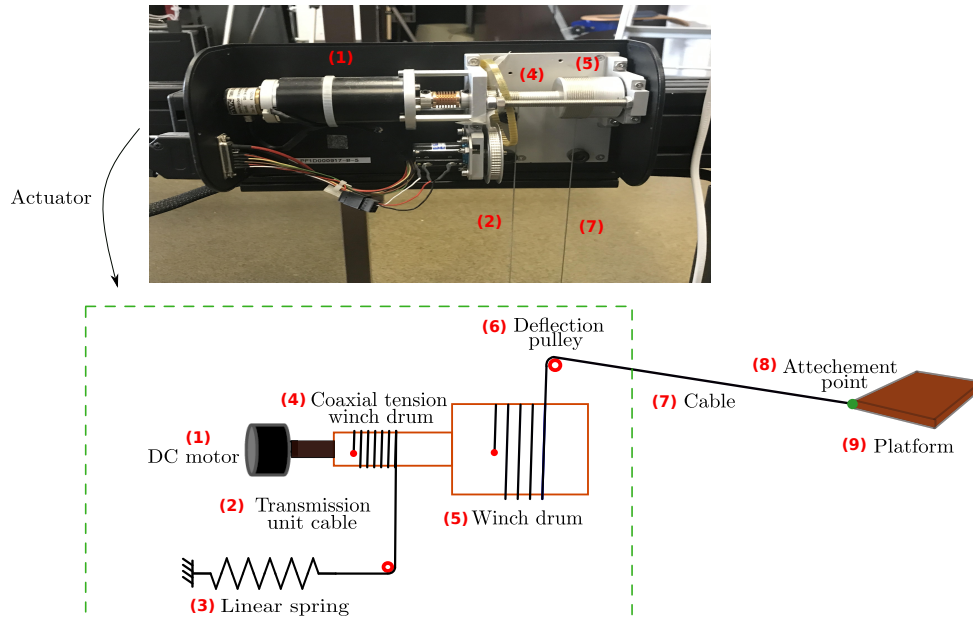
Figure 2.3: Actuator scheme of the INCA robot prototype.

2.2.3   Proprioceptive sensors

Two kinds of proprioceptive sensors are installed for the intrinsic measurement: four incremental optical encoders of type GIO 24 with 4×3600 pulses per revolution to measure the angular positions of the DC motors and four current sensors to measure the currents absorbed by the motors.

2.2.4   Computers

The real-time control architecture of the INCA required the use of three calculators (see Figure (2.4)):

- Vicon computer: is a Dell Inspiron computer that runs under a Windows 10 operating system, in this computer is installed the Vicon tracker software for tracking the platform's movement as will be detailed in the next section.

- Control computer: is a Dell Inspiron computer also where the Simulink is installed to implement the controller.

- INCA computer: is an Intel Pentium M 1.6 GHz that runs under a Linux-Xenomai real-time operating system. This computer contains An AXT power

supply, a MEANWELL $SP300-48$ power supply, a CPU NEXCOM EBX 562 card, a TOR $01LEMS010$ card, and two industrial PCI cards ($01LEMS015$). All these cards are embedded in the computer by Haption to drive the motors.
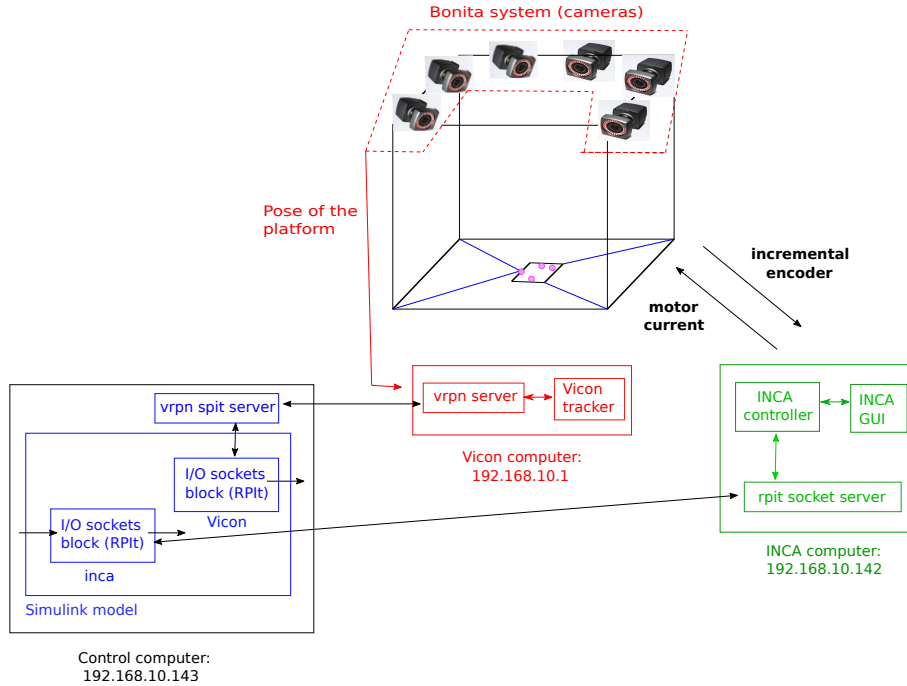
Figure 2.4: Real-time control architecture of the INCA.

2.2.5   Bonita motion capture system

The Bonita motion capture system is composed of six exteroceptive sensors that are used for extrinsic measurement. These sensors are infrared cameras with a maximum image acquisition frequency of 240 Hz with a VGA resolution to offer a good capture accuracy even for the movement of fast objects. The system is fixed to the top of the base to measure the platform's pose, while the platform is equipped with markers that reflect the radiation emitted by infrared diodes of cameras (see Figure (2.5)).

The tracking of the platform's movement is performed by the Vicon tracker software [2]. This software is used by the six infrared cameras (Bonita system) to stream the precise marker's motion (by detecting the reflection of the markers that are made of reflective material) and also to construct the 3D pose.

To track the motion of a rigid body and for data streaming recording, we create the object (the rigid body) with a fixed frame reference that we capture with the cameras by arranging at least three markers asymmetrically.

After calibrating the object to be tracked, the pose of the object (the platform) is then measured and subsequently made accessible to a second computer with a VRPN (Virtual-Reality Peripheral Network) server running on the tracking software.

The time delay estimated between the start of the image acquisition with the Bonita system and the availability of the platform pose measurement is 10.7 ± 0.7

---

[2]A software developed by the company Vicon version 5.

(a) Bonita system placed in the INCA.   (b) Infrared camera.
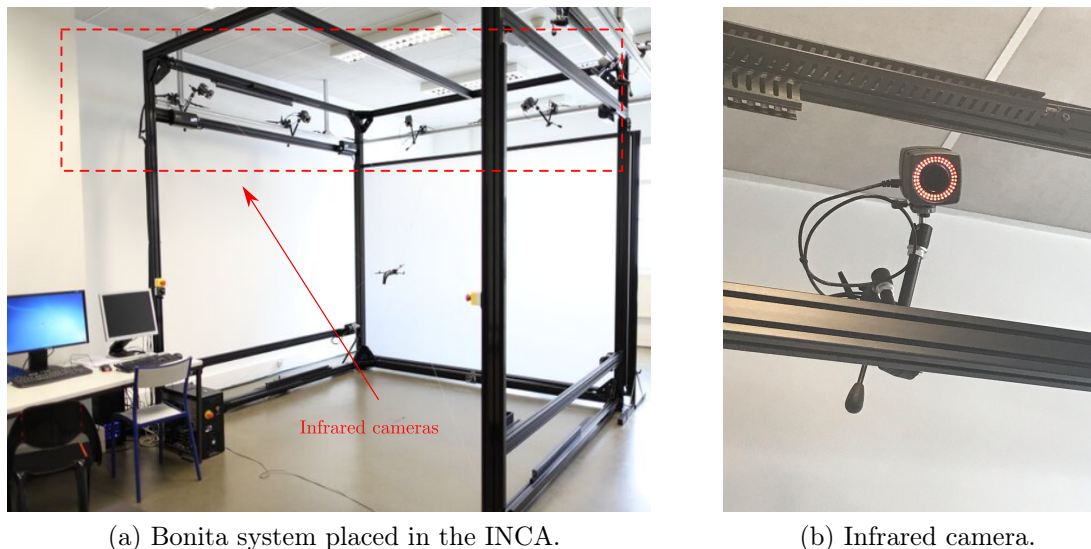
Figure 2.5: Bonita motion capture system.

ms as reported by Chellal (2016). The pose accuracy is estimated as 1.7 ± 0.4 mm from the root mean square error in the images between the current position and that estimated by the sensor system as reported by Chellal (2016).

2.2.6   Communication between the computers

The Vicon tracker software communicates with the INCA robot prototype (INCA computer) directly via the local network through an I/O socket block rpit. The closed-loop control can be implemented directly on Simulink which is installed on the control computer. Simulink's network requests are handled in the following two phases (see Figure 2.4):

- Phase one: A local server (vrpn-rpit-server) runs on the local PC (control's computer) to communicate between the Vicon tracker (Vicon computer) and the Simulink to recover the pose of the tracked object.

- Phase two: A network server (rpit-socket-server) runs on the INCA controller computer associated with the real-time controller and responds to Simulink requests (see the Simulink scheme in Figure (2.6)).

To model this INCA cable robot prototype, we considered its architecture and applied the laws of physics to find the dynamic model that suits it. Based on this architecture, we have proposed a dynamic model of a straight-line segments cable parallel planar robot that is demonstrated in detail in the next section (2.3).

In order to verify the acquisition of the position by the Bonita system and also to verify that we are on the plane, we have excited the prototype with currents on the 4 motors so that the platform can follow a square trajectory. The results of the pose measurements (6D) are shown in Figures (2.7, (2.8)). The results confirm the hypothesis of the 3DOFs, the horizontal translation, as well as the two out-of-plane orientations are quite negligible.
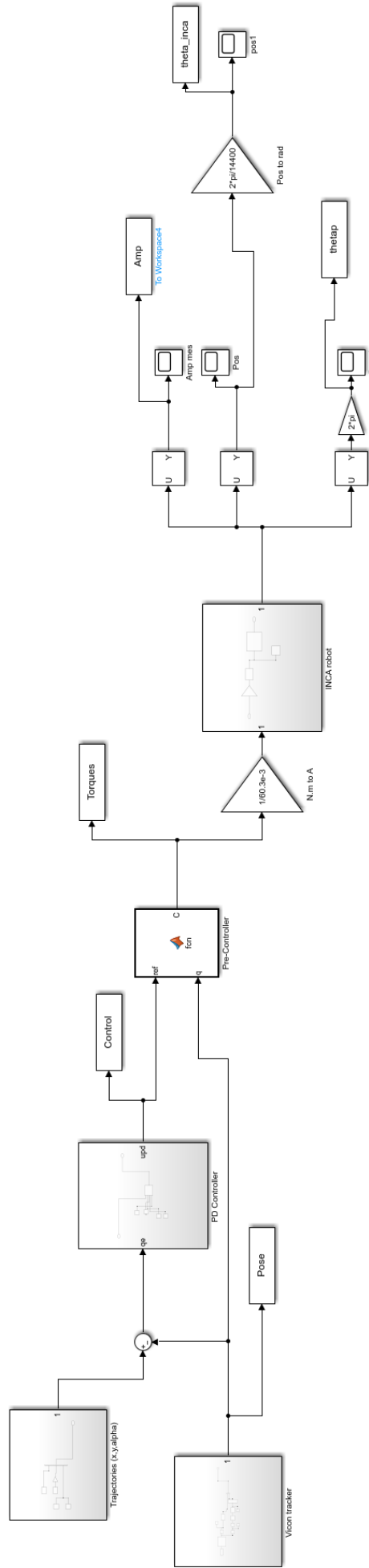
Figure 2.6: Simulink scheme used to control the INCA.
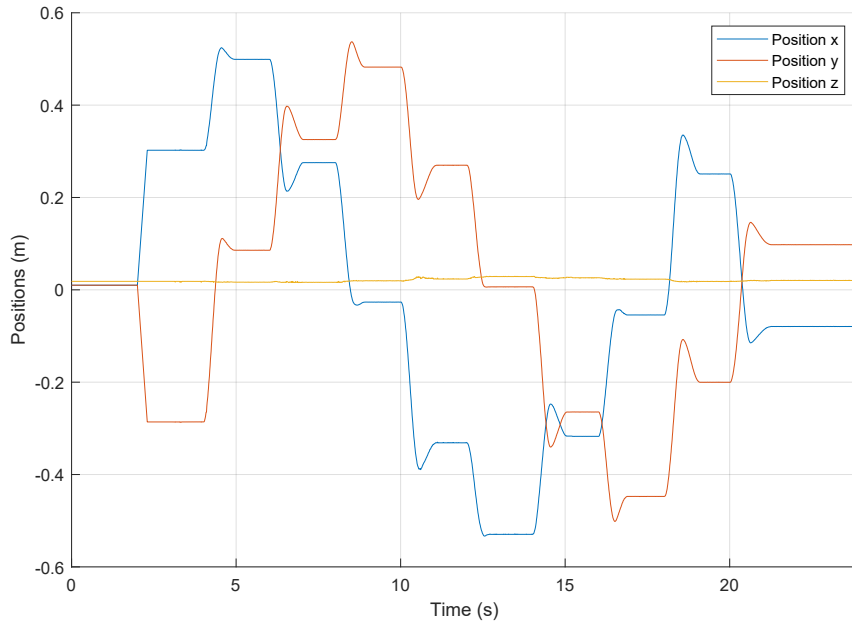
Figure 2.7: Open-loop trajectories of the platform positions $(x - y - z)$.
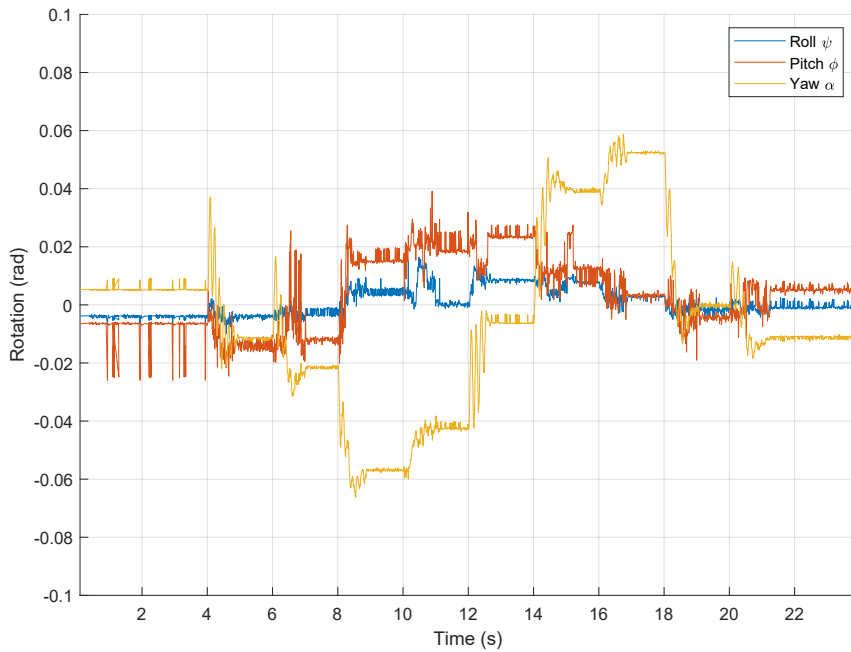
Figure 2.8: Open-loop trajectories of the platform orientations about axis $(x-y-z)$.

2.3 Simplified modeling

We first develop a simple model with the following modeling hypothesis: cables are straight-line segments without mass, flexibility, and extensibility. Despite this simplification, this modeling approach can be successfully used for studying the reachable workspace of CDPRs operating in a two or three dimensions space as by (Pusey et al. (2004), Chellal et al. (2017)).

2.3.1 CDPR description

We consider a planar CDPR with n cables attached to a moving platform $\mathcal{P}$, this setup is illustrated in Figure (2.9) with $n = 4$ cables and it is inspired by system experimental in Figure (2.1). The points A_i and B_i denote the proximal and distal anchor points of each cable. These points' positions are measured using a fixed global reference frame $\mathcal{R}_g = (O_g, \boldsymbol{x_g}, \boldsymbol{y_g})$ and a reference frame $\mathcal{R}_p = (O_p, \boldsymbol{x}, \boldsymbol{y})$ attached to the moving platform at its center of mass.
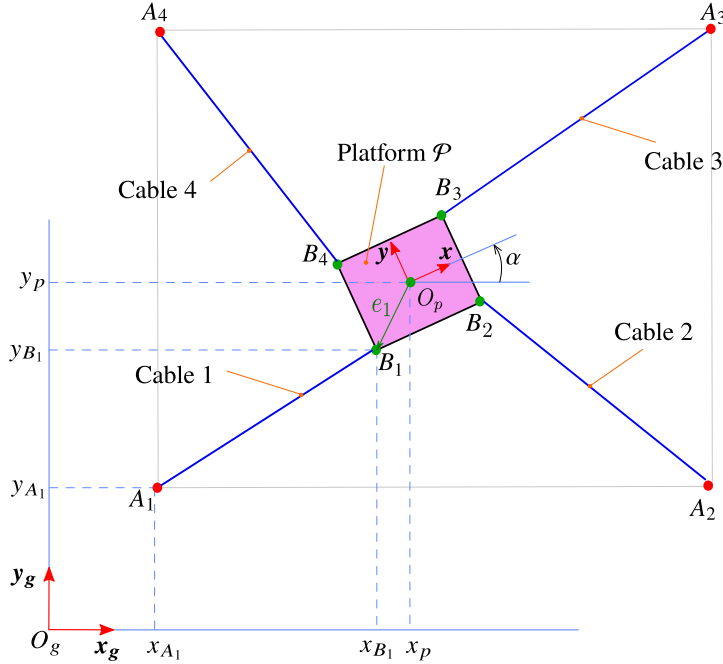
Figure 2.9: Schematic representation of a planar four straight-line segment cable robot.
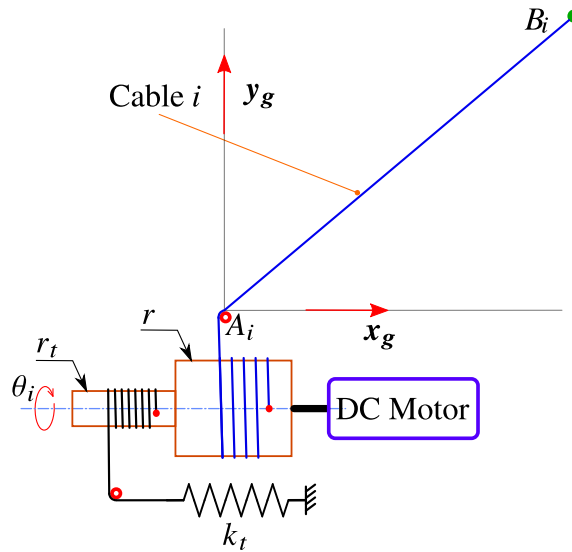
Figure 2.10: Working principle of a transmission unit for straight-line segment cable i.

The figure 2.10 describes the working principle of a transmission unit. The DC

motors rotate with an angle θ_i in both directions so that the cables can be unwound and wound around a winch drum of radius r. The actuators exert a torques τ_i on these winch drums. A second cable of total length $\tilde{l}_t$ is coiled on a coaxial tension winch drum of radius r_t and attached at its free end to a linear spring of stiffness k_t.

Based on the considered hypothesis, the cables are modeled as straight-line segments without mass, and their exit point, the A_i position, is considered fixed because the relative size of the output pulley at this point is small compared to the overall setup size. The CDPR is assumed to move in the horizontal plane. Therefore the following assumptions holds: the cable's tension is high enough so that the platform remains in the plane then all off-plane movements are neglected, which implies that gravity does not affect the movement on the plane. With an appropriate robot construction, we can observe that when we fully unwind the cable linked to the platform, then the pre-tension cable is also fully unwound, which means that we will obtain:

$$\tilde{l}_t = \frac{r_t}{r} l_t \tag{2.1}$$

where l_t is the total length of the cable i.

2.3.2 Position analysis

Considering the work in this thesis, the robot is planar, so the platform translates only on the $x - y$ plane and rotates about the z-axis with 3 DOFs. The kinematics of the robot is the relationship between the pose of the platform $X = \begin{bmatrix} x_p & y_p & \alpha \end{bmatrix}^T$ and the joint coordinates, ie the actuator positions $\theta = \begin{bmatrix} \theta_1 & \dots & \theta_n \end{bmatrix}^T$.

The position P_{A_i} of the exit point A_i of the $\#i$ cable is a fixed position in $\mathcal{R}_g$. The other end of the cable $\#i$ is attached to the platform at point B_i, and its position in $\mathcal{R}_g$ is denoted P_{B_i}. The length of the $\#i$ cable can be calculated by the Euclidean norm $l_i(X) = \|l_i\|_2 = \|A_i B_i\|_2$ between the position of the attachment point P_{B_i} and the position of the exit point P_{A_i} as:

$$l_i(X) = \|P_{B_i} - P_{A_i}\|_2 = \left\| P_p + \underbrace{{}^g R_p(\alpha)\, {}^p e_i}_{e_i(\alpha)} - P_{A_i} \right\|_2 \tag{2.2}$$

where $e_i(\alpha) = O_p B_i$ is the position of the point B_i in $\mathcal{R}_p$, and can be calculated using the fixed coordinates ${}^p e_i = {}^p O_P B_i$ in $\mathcal{R}_p$, and ${}^g R_p(\alpha)$ is the rotation matrix represented as:

$$ {}^g R_p(\alpha) = \begin{bmatrix} cos(\alpha) & -sin(\alpha) \\ sin(\alpha) & cos(\alpha) \end{bmatrix} \tag{2.3}$$

in which the homogeneous coordinates of a vector $\boldsymbol{v}$ in a reference frame $\mathcal{R}_j$ being denoted by ${}^j v$.

The initial configuration of the platform $X_0 = \begin{bmatrix} x_{p_0} & y_{p_0} & \alpha_0 \end{bmatrix}^T$ chosen at the center of the workspace, corresponds to the zero configuration of the actuators ($\theta_{i_0} = 0$) with an initial unwounded cable lengths $l(X_0) = \begin{bmatrix} l_{1_0} & \dots & l_{n_0} \end{bmatrix}^T$.

The inverse kinematic model can be written as follows:

$$\theta(X) = -\frac{l(X) - l(X_0)}{r} \tag{2.4}$$

where $l(X) = \begin{bmatrix} l_1 & \dots & l_n \end{bmatrix}^T$.

2.3.3 Velocity analysis

The first-order kinematic model of the robot is described by the relationship between the velocity of the platform $\dot{X} = \begin{bmatrix} \dot{x}_p & \dot{y}_p & \dot{\alpha} \end{bmatrix}^T$ and the vector of the angular velocity of the motors $\dot{\theta} = \begin{bmatrix} \dot{\theta}_1 & \dots & \dot{\theta}_n \end{bmatrix}^T$.

The time derivative of equation (2.4) gives:

$$\dot{\theta}(X, \dot{X}) = -\frac{\dot{l}(X, \dot{X})}{r}. \tag{2.5}$$

Using the differentiation with respect to the time of the equation (2.2), the equation (2.5) is expressed as:

$$\dot{\theta}(X, \dot{X}) = -\frac{1}{r} J \dot{X} \tag{2.6}$$

where the matrix J is the inverse Jacobian of dimension $n \times d$, given by:

$$J(X) = \begin{bmatrix} \frac{\partial l_1}{\partial x_p} & \frac{\partial l_1}{\partial y_p} & \frac{\partial l_1}{\partial \alpha} \\ \vdots & \vdots & \vdots \\ \frac{\partial l_n}{\partial x_p} & \frac{\partial l_n}{\partial y_p} & \frac{\partial l_n}{\partial \alpha} \end{bmatrix} \tag{2.7}$$

in which d is the number of DOFs.

2.3.4 Force analysis

The external forces applied on the platform $F_p = \begin{bmatrix} f_p^T & c_\alpha \end{bmatrix}^T$ are due to the cables' tension effect on the platform side. The force f_p is exerted at the center of mass O_p of the platform, and the torque c_α is exerted around this center of mass and they are calculated in equilibrium as:

$$f_p = -\sum_{i=1}^{n} \hat{l}_i T_i \tag{2.8}$$

$$c_\alpha = -\sum_{i=1}^{n} (e_i \times \hat{l}_i) T_i \tag{2.9}$$

where $\hat{l}_i = \frac{l_i}{\|l_i\|_2}$ is the unit vector in the direction of l_i.

Knowing that $J_i = \begin{bmatrix} \hat{l}_i^T & (e_i \times \hat{l}_i)^T \end{bmatrix}$ is a row of the inverse Jacobian matrix as reported by Merlet (2012), and using the equations (2.8) and (2.9) we can express the forces F_p applied at the platform as a function of the vector of the tensions of the cables $T = \begin{bmatrix} T_1 & ,\dots, & T_n \end{bmatrix}^T$ in the following matrix form as:

$$F_p = -J(X)^T T \tag{2.10}$$

2.3.5   Dynamic modeling

We consider that the robot is composed of two subsystems represented by the platform and the transmission unit that are connected by the cables. The dynamics of each subsystem will first be established separately and then assembled to obtain the dynamics of the global system.

Transmission unit dynamic modeling

In this section, we isolate the transmission unit, then the kinetic energy of the winch drum and of the coaxial tension winch drum is calculated as follows:

$$K_{w_i} = \frac{1}{2} j_i \dot{\theta}_i^2 \tag{2.11}$$

where j_i is the drum inertia calculated using the wounded portion of the cable as:

$$j_i = j_0 + \rho\,(l_t - l_i)\,r^2 + \rho\,(\tilde{l}_t - \tilde{l}_i)\,r_t^2 \tag{2.12}$$

where $\tilde{l}_i$ is the length of cable #i of the transmission unit, j_0 is the inertia of the drum and ρ is the cable mass per unit length.

Since $\theta_i = \dfrac{\tilde{l}_i}{r_t}$ and $(l_i - l_t) = -r\,\theta_i$ and using equations (2.12) and (2.1), we can express the equation (2.11) as follows:

$$K_{w_i} = \frac{1}{2} \left[j_0 + \rho l_t r^2 + \frac{\rho}{r}(r_t^3 - r^3)l_i \right] \dot{\theta}_i^2 \tag{2.13}$$

The potential energy V associated with the conservative forces exerted by the spring of each transmission unit can be expressed as:

$$V_i = \frac{1}{2} k_t (\tilde{l}_t - r_t\,\theta_i)^2 \quad (i = 1, \dots, n). \tag{2.14}$$

Knowing that $(l_i - l_t) = -r\,\theta_i$ and using equations (2.1) and (2.14), then we obtain the total potential energy associated with the conservative forces exerted by the spring of the whole system as:

$$V(X) = \sum_{i=1}^{n} \frac{1}{2} k_t \left(\frac{r_t}{r} \right)^2 l_i^2. \tag{2.15}$$

The applied external mechanical power to the transmission unit is represented by the actuation torque τ_i, the elastic action exerted by the tension spring and the positive tension force T_i exerted by the cable (see Figure 2.11). We assume that the transmission of cable tension from the actuator side to the platform side can be considered perfect (the tension on the platform side is identical to the tension on the actuator side) without delays and losses.

The work-energy theorem is applied to the transmission unit i to determine the tension force T_i of the cable #i as follows:

$$\dot{K}_{w_i} = -\dot{V} + \tau_i \dot{\theta}_i + T_i \dot{l}_i. \tag{2.16}$$

Using the time derivative of the equations (2.13) and (2.15), we obtain:
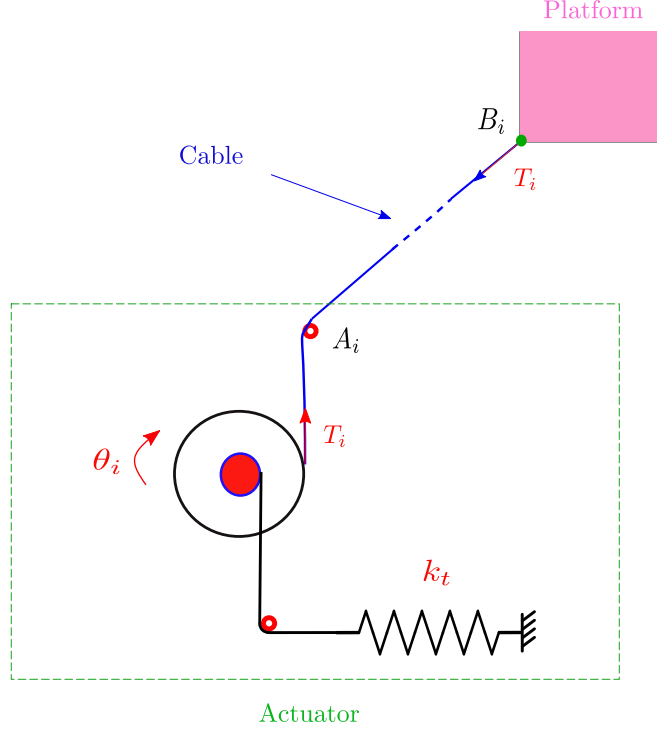
Figure 2.11: A global dynamic diagram of a 3 DOFs CDPR.

$$\tau_i\,\dot{\theta}_i + T_i\,\dot{l}_i - k_t\,\frac{r_t}{r}\,l_i\,\dot{l}_i - \frac{1}{2}\,\rho\,(r^3 - r_t^3)\,\dot{\theta}_i^2\,\dot{\theta}_i - (j_0 + \rho l_t r^2 + \rho\,(r_t^3 - r^3)\,\theta_i)\,\dot{\theta}_i\,\ddot{\theta}_i = 0. \quad (2.17)$$

Since $\dot{l}_i = -r\dot{\theta}_i$, $\ddot{l}_i = -r\ddot{\theta}_i$, the expression of T_i can be calculated as:

$$T_i = \frac{\tau_i}{r} + k_t\left(\frac{r_t}{r}\right)^2 l_i + \left[j_0 + \rho\frac{r_t^3}{r}l_t + \rho\frac{r^3 - r_t^3}{r}(l_t - l_i)\right]\frac{\ddot{l}_i}{r^2}$$
$$- \rho\frac{r^3 - r_t^3}{3r^3}\dot{l}_i^2. \quad (2.18)$$

Platform dynamic modeling

The cables are attached to the platform at the attachment points B_i, and each cable #i acts on the platform with the tension force $-\vec{T}_i$ as presented in Figure (2.11).

Considering the three variables (x_p, y_p, α), we can express the generalized coordinate vector as the pose of the platform $q = X = \begin{bmatrix} x_p & y_p & \alpha \end{bmatrix}^T$.

The kinetic energy of the platform is given by the following equation:

$$K_p = \frac{1}{2}m(\dot{x}_P^2 + \dot{y}_P^2) + \frac{1}{2}j_P\dot{\alpha}^2 \quad (2.19)$$

in which m is the mass of the platform and j_p is the inertia about its center of mass.

Global dynamic model

To obtain the global dynamic model we can use mechanic's analytical methods such as the Hamiltonian principle or the Lagrangian formalism (Goldstein et al. (2002)),

which allows modeling the CDPR using a finite set q of generalized coordinates. Our study uses Lagrangian formalism to determine the dynamic model. The development of the dynamic model is based on the following considerations:

- The kinetic energy of the whole system platform and transmission unit can be expressed as

$$K = K_p + \sum_{i=1}^{n} K_{w_i} \tag{2.20}$$

Kinetic energy can be expressed in its quadratic form as follows:

$$K(q, \dot{q}) = \frac{1}{2}\dot{q}^T M \dot{q} \tag{2.21}$$

where $M(q) = \mathrm{diag}(M_1, M_2, M_3)$ being the kinetic inertia matrix of the system.

- The generalized forces acting on the system are the wrench (force and torque) corresponding to the cable tension acting on the platform that can be expressed as:

$$Q = Q_{ext} = F_p. \tag{2.22}$$

- The dynamic model is given by the Lagrangian formalism as follows:

$$\frac{\mathrm{d}}{\mathrm{d}t}\left(\frac{\partial K}{\partial \dot{q}_j}\right) - \frac{\partial K}{\partial q_j} = Q_j \quad (j = 1, \ldots, 3). \tag{2.23}$$

The kinetic energy in equation (2.21) is quadratic in the velocity, then its time partial derivative is calculated as: $\dfrac{\partial K}{\partial \dot{q}} = M(q)\dot{q}$, which gives us $\dfrac{\mathrm{d}}{\mathrm{d}t}\dfrac{\partial K}{\partial \dot{q}} = M(q)\ddot{q} + \dot{M}(q)\dot{q}$. Afterward, for the whole set of equations, we find the model matrix form as follows:

$$M(q)\ddot{q} = Q + \frac{\partial K}{\partial q} - \dot{M}\dot{q}. \tag{2.24}$$

in which $Q = \begin{bmatrix} Q_1 & \ldots & Q_j \end{bmatrix}^T$ is the column matrix of generalized forces.

The dynamic model presented in (2.24), is an ordinary differential equation model (ODE model) with a minimal parametrization $q = \begin{bmatrix} x_p & y_p & \alpha \end{bmatrix}^T$. A different approach of modeling is possible by considering a redundant parametrization $q = \begin{bmatrix} l_i & x_p & y_p & \alpha \end{bmatrix}^T$ leads to a differential-algebraic equation model (DAE model) with Lagrange multipliers. There is no preference between the ODE model or the DAE model for modeling, due to the simplicity of the model with straight-line segments cable which makes obtaining algebraic expressions easy and possible for both approaches.

2.3.6 Cable tension distribution

In the case of a non-redundant actuated cable robot ($n \leq d$), the mechanism admits one feasible solution for the cable tension. This solution can be expressed according to the equation in (2.10) as:

$$T = W^{-1}(X)\, F_p \qquad (2.25)$$

where $W(X) = -J^T$ is the forces matrix assumed with full rank.

In the redundant actuated cable robot ($n > d$) case (which is the case of the robot studied in this thesis), the cables are susceptible to control all the DOFs with positive tensions. In this case, the mechanism admits an infinity of solutions that can be written:

$$T = W^+ F_p + \eta\, \mu \qquad (2.26)$$

where $W^+ = W^T\, (W\, W^T)^{-1}$ is the Moore–Penrose pseudoinverse of the matrix W, $\eta = null(W)$ is a $(n \times d)$ matrix, and $\mu = [\mu_1, \dots, \mu_d]^T$ is an arbitrary vector (Gouttefarde et al. (2015)).

2.3.7 Reachability of the workspace and tuning of the attachment points

The workspace analysis is a study that enables to determine of the reachability of the workspace. Since we want to control both the orientation and the translation of the platform, a study of the workspace reachability is necessary. The analysis presented here seeks to choose the platform design (attachment points) that increases the maneuverability in orientation after observing its weakness in the case of a configuration (1) (see Figure 2.12), and also to ensure the platform's stability during movement because our platform floats in space which makes it subject to flip-out off the $x - y$ plane.

The study was carried out in three stages:

- Selection of different platform geometries (the cables are attached to different attachment points).

- Evaluation of the possible external torque applied on the platform considering only the position at the center of the workspace.

- Choice of the platform geometry with better manoeuvrability in orientation.

First, we consider four different geometries for a rectangular platform (changing the cables attachment points location) to select the best geometry that offers us more freedom in orientation (see Figure 2.12). These geometries are the most reported in the planar parallel cable robot literature. Geometry (1) was considered to study a horizontal planar robot by Bayani et al. (2016), Fattah and Sunil (2005) considered geometry (2) to study a planar vertical cable robot, geometry (3) was used for the case of KNTU planar robot by Babaghasabha et al. (2015), and the geometry (4) was presented in the work of Williams II et al. (2003).

Then, we aim to determine the angle interval of α ensuring manoeuvrability, (i.e. on what interval of α the robot will be able to deliver positive or negative
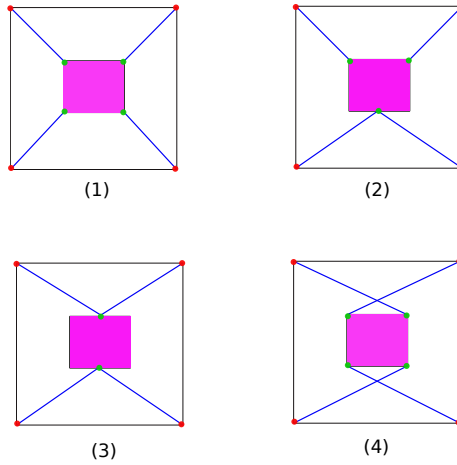
Figure 2.12: Different scenarios for different cable attachment points locations.

external torque applied to the platform (the accessible torque range)). To achieve this interval of α, we follow the Algorithm 1 for each geometry.

First, we limit ourselves to working in the center of the workspace ($x_p = 0, y_p = 0$), we vary α between -90° to $+90^o$ and for only two possible values of the torque motors of either min or max (0.1 N.m or 1 N.m) we consider the equation (2.10) to examine the obtained external torque c_α calculated by the following equation:

$$c_\alpha = - \begin{bmatrix} 0 & 0 & 1 \end{bmatrix} J(X)^T T. \tag{2.27}$$

---

input : Given a fixed position $x_p = 0$, $y_p = 0$, a two values (0.1 Nm or 1 Nm) of torques ($\tau_1, \tau_2, \tau_2, \tau_4$) and varied the orientation angle $\alpha \in [-90^o, 90^o]$.

output: External torque applied on the platform C_α.

for $\alpha \leftarrow -90$ **to** $+90$ **do**
    for $\tau_1 \leftarrow 0.1$ **to** 1 **do**
        for $\tau_2 \leftarrow 0.1$ **to** 1 **do**
            for $\tau_3 \leftarrow 0.1$ **to** 1 **do**
                for $\tau_4 \leftarrow 0.1$ **to** 1 **do**
                    Using equation (2.27) to calculate c_α;
                end
            end
        end
    end
end
Return the possible external torque applied on the platform c_α.

Algorithm 1: Calculation of reachable workspace in orientation.

The different geometries with different orientations that can perform each one of them are illustrated in Table (2.1).

	Maximum orientation
Geometry (1)	Can perform orientation that do not exceed $\pm 2.29^o$
Geometry (2)	Can perform orientation up to $\pm 30^o$
Geometry (3)	Can perform orientation up to $\pm 42.39^o$ but the platform is unstable
Geometry (4)	Can perform orientation up to $\pm 85.94^o$ but the platform is unstable

Table 2.1: The maximum orientation that the configurations in Figure (2.12) can perform

From the results presented in the Table (2.1), we draw the following conclusions:

- The geometry (1) was not considered in our study, because of its limitation in orientation.

- The geometry (2) is considered for our study because offers better manoeuvrability in orientation.

- The geometries (3) and (4) offer better maneuverability in orientation. However, they are not considered for our study because the platforms are not stable during the movement and can flip out off the $x - y$ plane. In addition, for geometry (4), the cables are crossed leading to the cable/cable contact problem. This problem can be avoided by placing cables in different plans or by considering a low-friction cable material as reported by Williams II et al. (2003) which is not possible in the case of our work given the existing robot prototype.
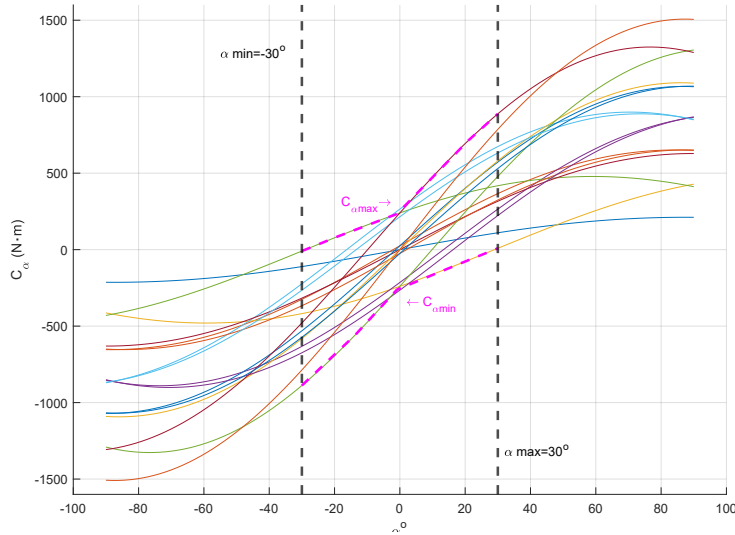
Figure 2.13: The external torque c_α for different values of α for geometry (2).

Figure 2.13, presents the obtained applied torque c_α for different values of α in the case of the geometry (2). Each curve represents the obtained possible external torque c_α applied on the platform by varying the orientation α (for 100 possible values between -90° and 90°) and by fixing each of the four motor torques at values

44

of either 0.1 N.m or 1 N.m (for two possible values for each motor torque we get 16 curves = 4^2). By considering the geometry in (2) and for a specific square trajectory, we defined the workspace reachability by calculating the possible orientation in a different location in the workspace as illustrated by Figure 2.14. From these results, we identify the approximate orientation interval that can be applied on a platform as $\alpha = \pm 26.35^o$.
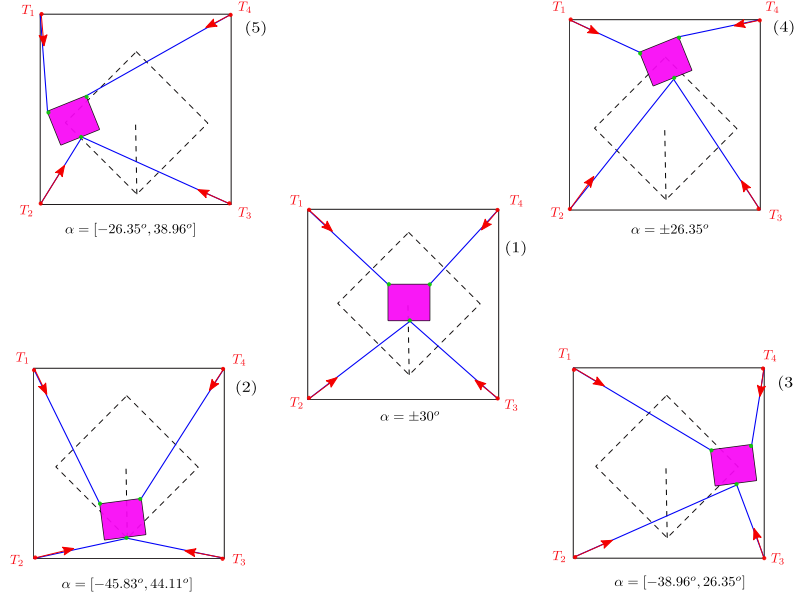
Figure 2.14: The platform's possible orientation in different locations in the workspace.

2.3.8 PD and PID controllers implementation

The aim of designing the PD or the PID controllers is to have standard controllers used to highlight the advantages of the $\mathcal{H}_\infty$ (studied in chapter 4) synthesized for the cable robot model with flexibilities.

PD controller design

We considered the straight-line segments cable model presented in section (2.3.5) to design the PD controller. Considering the equation (2.10), then the forces applied on the platform can be written as:

$$M_m \ddot{q} = -\frac{1}{r} J^T(q)\,\tau \tag{2.28}$$

where $M_m = \text{diag}(m, m, J_p)$.

The objective is to control the platform of the CDPR in position and orientation with the PD controller while ensuring positive cable tensions. The control is performed by driving the winch motor's torques (control signals) u in order that the platform can track the imposed trajectories $q^* = (x_p^*, y_p^*, \alpha^*)$. The control makes it possible to converge q towards the reference q^* using the closed-loop reference model that is presented as:

$$\ddot{q} + A_a \dot{q} + B_b q = B_b q^*. \tag{2.29}$$

The matrices are given as: $A_a = \mathrm{diag}(2\,\xi\,w_0, 2\,\xi\,w_0, 2\,\xi\,w_{00})$, $B_b = \mathrm{diag}(w_0^2, w_0^2, w_{00}^2)$, with ξ is the damping ratio and w_0 and w_{00} are the natural frequencies that define the position and orientation dynamics respectively.

Left multiplying the equation (2.29) by M_m, and using the equation (2.28), the control u must satisfy the following equation:

$$M_m \left(B_b \left(q^* - q\right) - A_a \dot{q}\right) = -\frac{1}{r}\, J^T(q)\,\tau. \tag{2.30}$$

From equations (2.30) and (2.26), the control signal τ that ensures the platform to follow the trajectories references q^* is calculated as:

$$\tau = -\frac{1}{r}\, J^{+T}(q)\, \overbrace{(\underbrace{M_m\, B_b}_{C_p}\, (q^* - q) - \underbrace{M_m\, A_a}_{C_d}\, \dot{q})}^{u_{PD}} + u_1 \tag{2.31}$$

where $u_1 \in \ker(J^T)$ is a vector that ensures the cable's tensions remain positive. The PD control signal u_{PD} is computed by choosing the proportional gain $C_p = M_m\, B_b$, and the derivative gain $C_d = M_m\, A_a$.

PID controller design

The PID controller has been designed for the same objectives as the PD controller.

By considering the platform position and orientation reference signal q^* and the control signal $u = \tau$, then the model is written as follows:

$$M_m \ddot{q} = -\frac{1}{r}\, J^T(q)\,\tau. \tag{2.32}$$

The objective is to design a PID controller with two degrees of freedom. The used control law is written as:

$$u(t) = \tau = C_i \int_0^t \left(q^*(\tau) - q(\tau)\right) d\tau + C_p \left(b\, q^*(t) - q(t)\right) - C_d\, \dot{q}(t). \tag{2.33}$$

We choose $b = 0$ to ensure a continuous control in the presence of a step on the reference. By replacing the control law expression u in the equation (2.32) and by time deriving it, we obtain:

$$M_m\, \dddot{q}(t) = -\frac{1}{r}\, J^T(q)\, (C_i\, (q^*(t) - q(t)) - C_p\, \dot{q}(t) - C_d\, \ddot{q}(t)) \tag{2.34}$$

then,

$$\dddot{q}(t) - \frac{1}{r}\, J^T(q)\, M_m^{-1}(\,C_i\, q(t) + C_p\, \dot{q}(t) + C_d\, \ddot{q}(t)) = -\frac{1}{r}\, J^T(q)\, M_m^{-1}\, C_i\, q^*(t). \tag{2.35}$$

The closed-loop model in the equation (2.35) is of order three and possesses three poles. By applying a Laplace transform, the characteristic equation of a model with order three can be written, considering the poles, as:

$$s^3 + \underbrace{(p_1 + p_2 + p_3)}_{z_1} s^2 + \underbrace{(p_1\,p_2 + p_2\,p_3 + p_1\,p_3)}_{z_2} s + \underbrace{p_1\,p_2\,p_3}_{z_3} = 0. \qquad (2.36)$$

Then, the PID gains in the equation (2.35) can be obtained as: $C_d = -\frac{1}{r}\,J^T(q)\,M_m^{-1}\,A_a$, $C_p = -\frac{1}{r}\,J^T(q)\,M_m^{-1}\,B_b$, and $C_i = -\frac{1}{r}\,J^T(q)\,M_m^{-1}\,D_d$, where the matrices are given as using the equation (2.36) as: $A_a = \mathrm{diag}(z_1, z_1, z_1)$, $B_a = \mathrm{diag}(z_2, z_2, z_2)$, and $D_d = \mathrm{diag}(z_3, z_3, z_3)$.

The value of the three poles $(-p_1, -p_2, -p_3)$ are to be chosen such that to ensure the stability of the closed-loop system.

2.4 Conclusion

This chapter sets out the structure and the model of the system considered for the study. First, a detailed description of the hardware and the software of the INCA planar cable robot prototype was presented. Then, the model for planar CDPR with three degrees of freedom was developed by considering n cables and integrating the pre-tensioning system for more realistic modeling of the existing prototype INCA. The dynamic modeling was performed based on the Euler-Lagrange formalism.

A simple hypothesis of modeling was taken into account in this chapter which assumes that the cables are modeled as a straight-line segment. This model version was used to study the workspace reachability in order to choose the geometry of the platform's attachment points, which offers us good maneuverability on orientation. Therefore, this rigid cable model served as a basis to manage the cables' tension during the design of the PD and PID controllers.

The following chapter uses the same Euler-Lagrange formalism for the modeling to obtain a more complex version of the dynamic model, which assumes that the cables are flexible.

Chapter 3

Dynamic modeling of a flexible cable-driven parallel robots

3.1   Introduction

This chapter presents a more complete and complex version of the dynamic model than the one presented in the chapter (2). This version takes into account the flexibility and the mass of cables where the flexibility has been modeled using the assumed modes approach. Using the Euler-Lagrange formalism, a differential-algebraic equation model was obtained.

The $\mathcal{H}_\infty$ synthesis requires first the linearization of the dynamic model, thus two different linearization approaches of the DAE model have been applied. Nevertheless, these approaches failed because they produced non-controllable and non-observable linear models. Thus, a transformation of the DAE model into an ordinary differential algebraic model has been performed, and the obtained model has been linearized. This yields a linear model suitable for $\mathcal{H}_\infty$ controller design.

The chapter also presents the steps we have followed to validate the geometric flexible cable robot model proposed theoretically. The geometric validation of the theoretical model was performed based on the data collected from a video of the motion of cables of the INCA prototype.

3.2   Model with flexible cables

In a real-world application, the cables are not straight-line segments and are subject to the forces exerted by their own weight and those applied to their extremities, resulting in a phenomenon of flexibility also called deformation (see Figure 3.1). Considering this flexibility and the mass of the cables in their modeling makes the models more precise.

To begin with, we attempted to implement Du and Agrawal (2015) approach. This approach was based on obtaining the 3D dynamic model using the Hamiltonian principle and by modeling the flexibility of cables considering the assumed modes approach with six flexibility modes. For this model, constraint violation stabilization techniques have been employed to express the acceleration constraint as presented by Baumgarte (1972). Following this model, we could not obtain an algebraic model suitable for synthesis and simulation due to its complexity.

Afterward, we opted for the model where the dynamic model is obtained by con-

sidering the same steps as the straight-line segments modeling (in section 3.2) using the Lagrangian formalism. The exception is that to avoid the complexity of equations with the consideration of flexibility, we choose a redundant parametrization resulting in algebraic constraints between the variables, which yields a differential algebraic equation model (DAE model) with Lagrange multipliers. This approach of modeling was developed first by Ayala Cuevas et al. (2017) for 2 DOFs flexible 3 cables robot. In this thesis, we extended the modeling to a 3 DOFs flexible 4-cable robot.

Finally, to obtain a suitable linear model for control purposes, we managed to perform a transformation of the DAE model into an ordinary differential equation model (ODE model) despite the complexity of the equations.
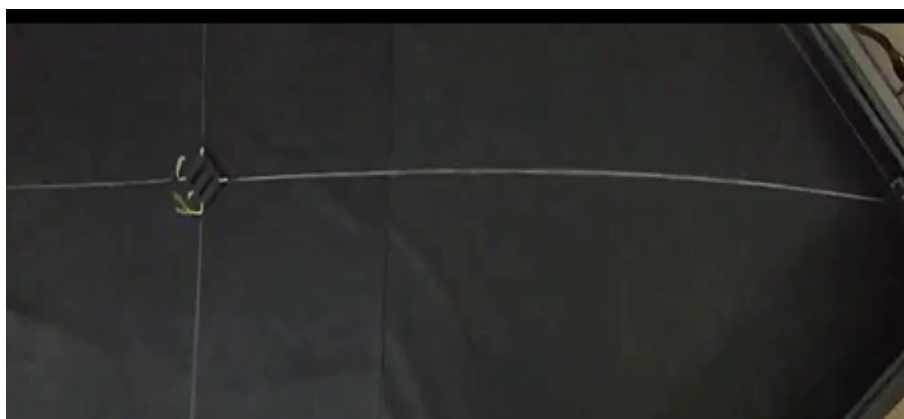
Figure 3.1: The observation of cable flexibility during the movement of INCA prototype.

3.2.1 Position analysis of a flexible cable

The description of the parallel-driven flexible cable robot (see Figure 3.2) is similar to that of the robot with straight-line segments cables presented in section 2.3.2. However, the mass and the flexibility of cables considered.

We assume that:

- Each cable is perfectly flexible and inextensible.

- There is no twist in cables.

- All off-plane flexibilities are ignored.

- The cable is flexible and the flexibility is modeled following the assumed modes approach.

Transverse displacement of the cables

We aim to describe its transverse displacement in a plane. A point M_i is located on the unwound portion of the ith cable between A_i and B_i and the local reference frame $\mathcal{R}_i = (A_i, \boldsymbol{x_{l_i}}, \boldsymbol{y_{l_i}})$ is attached to the flexible cable #i (see Figure 3.3a), starting from a rectilinear position of the cable along the $\boldsymbol{x_i}$ direction. The position of the point
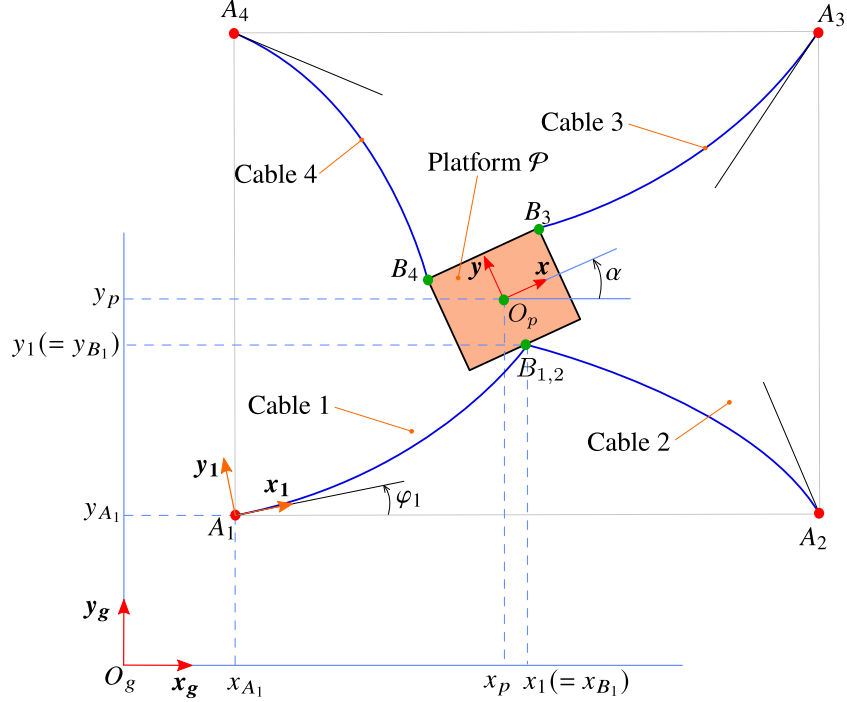
Figure 3.2: Schematic representation of a planar four flexible cable robot.

M_i on the deformable 1-D continuum is parameterized by the arclength $x \in [0, l_i]$ ($x = 0$ corresponds to the winch drum's location while $x = l_i$ corresponds to the position of the end of cables). Based on Euler–Bernoulli beam theory (Timoshenko (1953)), we assume that by displacing laterally the cables, the point M_i would be displaced with a small displacement $\boldsymbol{\delta M_i} = \delta x_{M_i} \boldsymbol{x_{l_i}} + \delta y_{M_i} \boldsymbol{y_{l_i}}$ along the $\boldsymbol{x_{l_i}}$ and $\boldsymbol{y_{l_i}}$ directions to its next position of the coordinates $(x_{M_i}, y_{M_i}) = (x + \delta x_{M_i}, \delta y_{M_i})$.

An approach based on discretization is chosen to interpret the transverse displacement; this approach uses the assumed modes (Meirovitch (1967)). DeLuca and Siciliano (1993) used it for modeling the deformation of segments of a robot arm. Then this approach has been adapted to model the flexibilities of the cables as presented by (Du and Agrawal (2015), Godbole et al. (2019)).

The approach is used to approximate the form that the transverse vibration can take. The vibration is represented as a linear combination of a finite number of time-dependent modes a_{ij} and functions Φ_j dependent on space as:

$$\delta y_{m_i}(x, t) = \sum_{j=1}^{N} \Phi_j(x) \, a_{ij}(t) \tag{3.1}$$

where the function $\Phi_j(x)$ represents the shape of flexibility and N is the number of flexibility modes. The literature reports a number of approaches to expressing the shape of flexibility, either using eigenvalue problem as by Meirovitch (1967) or polynomial shape as by Du and Agrawal (2015).

To represent the shape of the flexibility, we choose a polynomial basis of the from $a_0 + a_1 \, x + a_2 \, x^2 + \ldots + a_N \, x^N$. The constant term was not considered because the displacement is null at the point of contact with the drum. The linear term is also not considered as a mode of flexibility but as an orientation. Then, the polynomial function that we have chosen for this work starts from the term of order 2. By

50

(a) Cable lateral displacement.

(b) Cable representation in new reference frame.
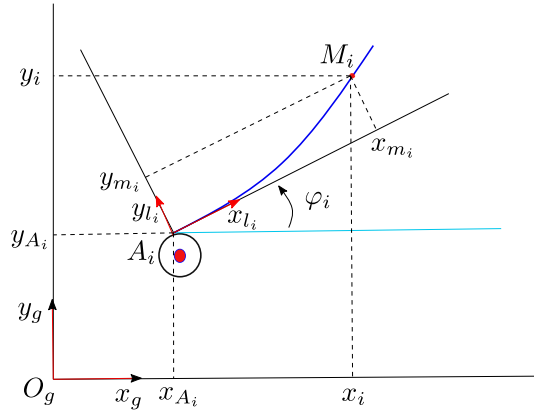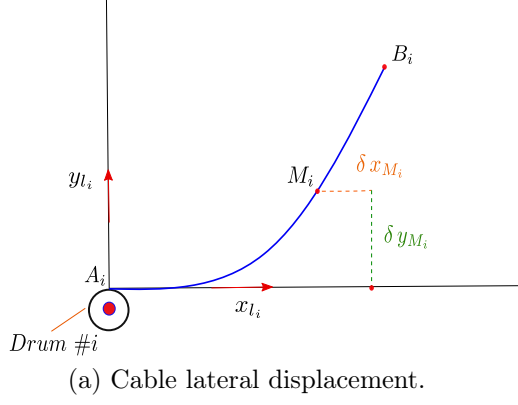
Figure 3.3: Displacement of the flexible cable.

considering only one mode of flexibility $a_{ij}(t) \triangleq a_i(t)$ and by taking $a_i(t) = \frac{w_i(t)}{l_i}$, then the considered polynomial shape of flexibility is given as: $\Phi_j(x) = x^{j+1}$ so that the displacement along the direction $\boldsymbol{y_i}$ is represented as:

$$\delta y_{m_i}(x,t) = \frac{x^2}{l_i}w_i(t). \tag{3.2}$$

where w_i is a new representation of the flexibility modes.

Other shapes of flexibility have been chosen in the literature. For instance, Godbole et al. (2019) used the trigonometric shape of flexibility for the case of a model with 2 cables and 1DOFs. We have chosen not to consider this form of flexibility since it is more challenging to master it in the case of a model with a higher number of cables and DOFs.

Considering the principle of length conservation presented by Shi et al. (2000), the displacement along the direction $\boldsymbol{x_i}$ can be expressed as:

$$\delta x_{m_i} = -\frac{1}{2}\int_0^x (\frac{\partial\,\delta y_{m_i}(\zeta,t)}{\partial x})^2\,d\zeta = -\frac{2x^3}{3l_i^2}w_i^2(t). \tag{3.3}$$

A detailed presentation of the derivation of the equation (3.3) has been relegated to the appendix A.1.

The configuration of cable #i is defined using the local reference frame $\mathcal{R}_i = (A_i, \boldsymbol{x_{l_i}}, \boldsymbol{y_{l_i}})$ whose $\boldsymbol{x_i}$ axis is the tangent to the output pulley of the transmission unit and the cable at point A_i. The fixed global reference frame is denoted $\mathcal{R}_g = (O_g, x_g, y_g)$, where the orientation angle of cables φ_i is the angle between the two references $(\mathcal{R}_i, \mathcal{R}_g)$ (see Figure 3.3b).

Considering the translation shift (the position of the winch drum) between the two reference frames, then we realize the transformation between the two reference frames with the homogeneous matrix to express the coordinates of point M_i in the new global frame as:

$$
\begin{bmatrix} x_i \\ y_i \\ 1 \end{bmatrix} = \begin{bmatrix} cos(\varphi_i) & -sin(\varphi_i) & x_{A_i} \\ sin(\varphi_i) & cos(\varphi_i) & y_{A_i} \\ 0 & 0 & 1 \end{bmatrix} \begin{bmatrix} x_{m_i} \\ y_{m_i} \\ 1 \end{bmatrix}. \tag{3.4}
$$

The position of the moving point M_i in $\mathcal{R}_g$ can therefore be expressed as:

$$
\begin{cases} x_i(\tilde{q}_i) = cos(\varphi_i)\, x_{m_i} - sin(\varphi_i)\, y_{m_i} + x_{A_i} \\ y_i(\tilde{q}_i) = sin(\varphi_i)\, x_{m_i} + cos(\varphi_i)\, y_{m_i} + y_{A_i} \end{cases} \quad \text{for } i = 1, \dots, n \tag{3.5}
$$

where $\tilde{q}_i = \begin{bmatrix} x & w_i & \varphi_i \end{bmatrix}^T$ corresponds to $N + 2 = 3$ independent variables. During the movement we consider x equals l_i, then we obtain the vector $q_i = \begin{bmatrix} l_i & w_i & \varphi_i \end{bmatrix}^T$ that gathers the variables of cable #i.

Note that l_i, w_i, and φ_i are functions of time.

By gathering the platform coordinates and orientation and the 3 variables of each n cable, then the generalized coordinate vector of the flexible CDPR is expressed as $q = \begin{bmatrix} q_1^T \dots q_n^T & x_p & y_p & \alpha \end{bmatrix}^T$ with $3n + 3$ entries [1].

3.2.2 Velocity analysis of a flexible cable

The position vector of point M_i in the fixed reference $\mathcal{R}_g$ depends on the three variables l_i, w_i and φ_i, then its velocity vector has its components along the direction $\boldsymbol{x_g}$ and along $\boldsymbol{y_g}$ as:

$$
v_{x_i} = \frac{\partial x_{l_i}}{\partial l_i}\, \dot{l}_i + \frac{\partial x_{l_i}}{\partial w_i}\, \dot{w}_i + \frac{\partial x_{l_i}}{\partial \varphi_i}\, \dot{\varphi}_i. \tag{3.6}
$$

$$
v_{y_i} = \frac{\partial y_{l_i}}{\partial x}\, \dot{l}_i + \frac{\partial y_{l_i}}{\partial w_i}\, \dot{w}_i + \frac{\partial y_{l_i}}{\partial \varphi_i}\, \dot{\varphi}_i. \tag{3.7}
$$

3.2.3 Geometric constraints

To mitigate equation complexity, we choose a redundant parametrization which results in algebraic constraints rather than minimal parametrization. These geometric constraints appear since CDPRs are closed kinematic chain systems. These algebraic (holonomic) constraints impose that the position of the end of each cable coincides with the platform's attachment points. Considering the position of the attachment point P_{B_i} and the position of the end-cable from equation (3.5), then we can form the two constraints provided by each cable as follows:

---

[1]The generalized coordinate vector presented in this section $q \in \mathbb{R}^{3n+3}$ is different than the one $q \in \mathbb{R}^3$ presented in the previous section (2.3.5).

$$h : \begin{cases} x_i(q_i) - x_{B_i} \\ y_i(q_i) - y_{B_i} \end{cases} \quad (i = 1, \ldots, n) \tag{3.8}$$

These equations can be gathered into a single vector equation $h(q) = 0$. Upon time differentiation of h, the Jacobian matrix A of the constraints can be calculated as:

$$\frac{\partial h(q)}{\partial q} \dot{q} = A(q)\dot{q} = 0. \tag{3.9}$$

The Jacobian matrix of the constraints equation concerning the generalized coordinates is given as follows:

$$A = \begin{bmatrix} \frac{\partial h_1(q)}{\partial q_1} & \cdots & \frac{\partial h_1(q)}{\partial q_{3n+3}} \\ \vdots & \cdots & \vdots \\ \frac{\partial h_{2n}(q)}{\partial q_1} & \cdots & \frac{\partial h_{2n}(q)}{\partial q_{3n+3}} \end{bmatrix} \tag{3.10}$$

3.2.4 Dynamic model

The aim is to find the dynamic model of a flexible cable parallel robot. Cable parallel robots are systems submitted to kinematic constraints. For the modeling of systems under constraints, the geometric or kinematic relations of its constraints are not always obvious, and obtaining their expressions is very complicated and sometimes impossible. Then in this case of complex systems, an alternative method of modeling based on the multipliers of Lagrange can be used as reported by Goldstein et al. (2002).

In the case of planar parallel cable robot that moves on the vertical plane, the gravity is not neglected, and the gravitational potential energy is considered in the Lagrange function $\mathcal{L} = K - V$ calculation. In the case of planar parallel cable robot that moves on the horizontal plane, the gravity is neglected (as we assumed that all off-plane movements are neglected), and the Lagrange function is calculated only with the kinetic energy $\mathcal{L} = K$ in the section 2.3.2. In the following, we will present the model for the vertical case where the effect of gravity is not neglected and the gravitational potential energy is considered.

Gravitational potential energy

The gravitational potential energy of each cable is given by the equation:

$$V_{p_i} = \int_0^{l_i} \rho \, g \, y_i(s_i) \, dx \quad (i = 1, \ldots, n) \tag{3.11}$$

The gravitational potential energy of the whole system is the sum of the gravitational potential energies of the platform and of each cable, and also the potential energy associated with the conservative forces exerted by the springs of the transmission units. It is given as follows:

$$V(q) = -m \, g \, y_p + \sum_{i=1}^{n} V_{p_i} + \sum_{i=1}^{n} \frac{1}{2} k_t \left(\frac{r_t}{r}\right)^2 l_i^2 \quad (i = 1, \ldots, n). \tag{3.12}$$

Kinetic energy

- The kinetic energy of each cable can be expressed as:

$$K_{c_i} = \frac{1}{2} \int_0^{l_i} \rho\, v_i^2 \, dx. \tag{3.13}$$

- The kinetic energy of the whole system (cables, winch drums (equation 2.13) and platform (equation 2.19)) is given as follows:

$$K = \sum_{i=1}^{n} (K_{c_i} + K_{w_i}) + K_p = \frac{1}{2}\dot{q}^T M \dot{q} \tag{3.14}$$

where $M(q) = \mathrm{diag}(M_0, M_1, \ldots, M_n)$ represents the total inertia matrix of the system, with M_0 is the inertia matrix of the platform and M_i is the inertia matrix relative to each cable $\#i$.

Generalized forces

The generalized forces acting on the system are only the external actions exerted by the actuators and the springs in the transmission units. The single non zero generalized forces corresponding to the generalized coordinates $(l_1 \ldots l_n)$ can be calculated as:

$$Q_i = -\frac{\partial V}{\partial q_i} - \frac{\tau_i}{r} = -\frac{1}{2}k_t \left(\frac{r_t}{r}\right)^2 l_i - \frac{\tau_i}{r} \qquad (i = 1 \ldots n) \tag{3.15}$$

Lagrange's equations

To introduce the constraints of the Euler-Lagrange equation, we use the Lagrange multipliers λ_i for each constraint (Bertsekas (1982)). Therefore, the Euler-Lagrange equations is given as follows:

$$\frac{\mathrm{d}}{\mathrm{d}t}\left(\frac{\partial K}{\partial \dot{q}_k}\right) - \frac{\partial K}{\partial q_k} = Q_k + \sum_{r=1}^{2n} \lambda_r A_{rk}. \qquad (k = 1 \ldots 3n+3, \quad r = 1 \ldots 2n) \tag{3.16}$$

DAE model

Considering the quadratic form of the kinetic energy $\dfrac{\partial K}{\partial \dot{q}} = M\dot{q}$, the matrix form of the $3n + 3$ Lagrange equations is expressed as :

$$\dot{M}(q,\dot{q})\dot{q} + M(q)\ddot{q} = \underbrace{\frac{\partial K(q,\dot{q})}{\partial q}}_{C} + Q(q,\tau) + A(q)^T \lambda \tag{3.17}$$

where $\lambda = \begin{bmatrix} \lambda_1, \ldots, \lambda_{2n} \end{bmatrix}^T$ is the vector of the Lagrange multipliers, $Q = \begin{bmatrix} Q_1, \ldots, Q_{3n+3} \end{bmatrix}^T$ is the column matrix of generalized forces, and $C = \begin{bmatrix} \frac{1}{2}\, q^T \frac{\partial M}{\partial q_1}\, q^T & \cdots & \frac{1}{2}\, q^T \frac{\partial M}{\partial q_{3n+3}}\, q^T \end{bmatrix}^T$.

By gathering the time derivative of the equation (3.9) with the dynamic equation (3.17), the dynamic model expressed as a differential-algebraic equation (DAE), is given as:

$$\underbrace{\begin{bmatrix} M(q) & -A(q)^T \\ A(q) & \mathbb{O}_{2n \times 2n} \end{bmatrix}}_{H} \begin{bmatrix} \ddot{q} \\ \lambda \end{bmatrix} = \underbrace{\begin{bmatrix} C(q,\dot{q}) + Q(q,\tau) - \dot{M}(q,\dot{q})\,\dot{q} \\ -\dot{A}(q,\dot{q})\,\dot{q} \end{bmatrix}}_{F}. \qquad (3.18)$$

Remark 1. *For the implementation of this model, the algebraic expressions have been calculated with* `Maple`*. The simulation of this non-linear DAE model with* `Matlab` *has been done by inverting the matrix H numerically.*

3.2.5 Linearization of the DAE model

The research aim of this thesis is to find an $\mathcal{H}_\infty$ controller for the flexible CDPR model. The $\mathcal{H}_\infty$ synthesis requires a model linearization. We considered the DAE model and used two approaches to get a linear model suitable for control. The scheme in Figure (3.4) presents the methodology followed for the two approaches. The first method was based on the direct linearization of the DAE model as a descriptor linear model and then testing the controllability and observability of the obtained model to synthesize the $\mathcal{H}_\infty$ controller. The second method was based on the inversion of the matrix H of the DAE model and after the linearization of the model, we tried also to reduce the order of the model in the idea that it can resolve the problem of the non-controllability and non-observability of the linear model.
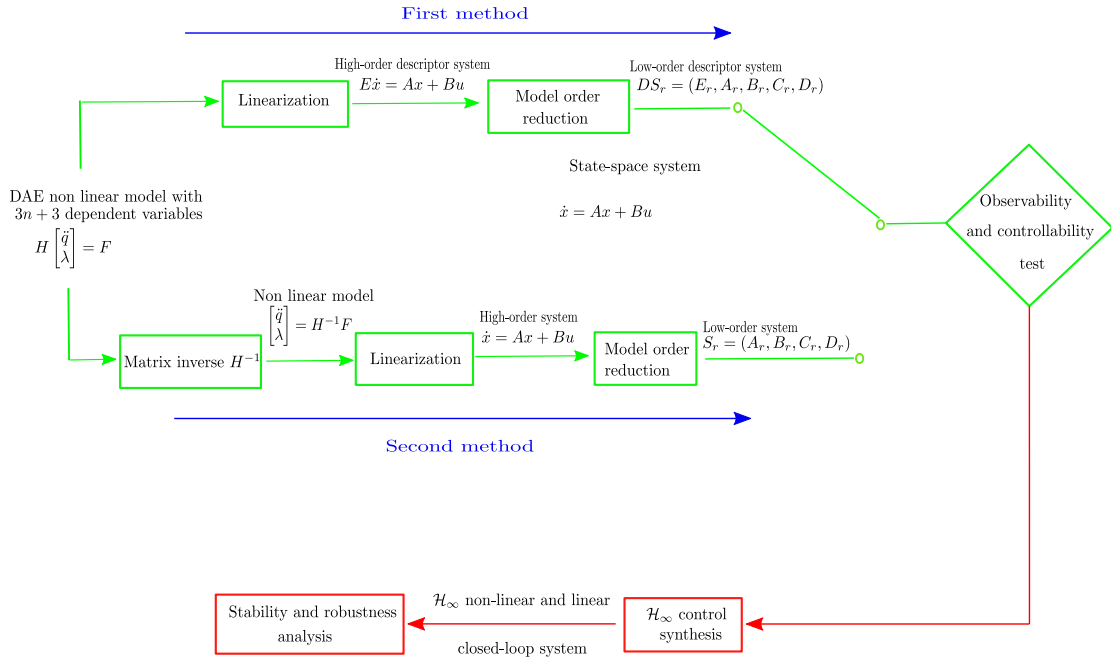
Figure 3.4: Control and linearization methodology for the DAE model.

First method: direct linearization of DAE model

The left-hand side matrix H in the model (3.18) is an invertible matrix:

$$\begin{bmatrix} \ddot{q} \\ \lambda \end{bmatrix} = \underbrace{\begin{bmatrix} M^{-1}\left(I + A^T P^{-1} A M^{-1}\right) & M^{-1} A^T P^{-1} \\ -P^{-1} A M^{-1} & P^{-1} \end{bmatrix}}_{H^{-1}} \underbrace{\begin{bmatrix} F1 \\ F2 \end{bmatrix}}_{F} = \Gamma(q, \dot{q}, \tau) \qquad (3.19)$$

in which $P = -A M^{-1} A^T$ and $\tau = [\tau_i, \dots, \tau_n]^T$.

This possibility of matrix inversion reveal a second-order ODE model $\ddot{q} = f(q, \dot{q}, u)$ depending on $3n + 3$ state variables as follows:

$$\ddot{q} = \left(M^{-1}\left(I + A^T P^{-1} A M^{-1}\right)\right) F_1 + \left(M^{-1} A^T P^{-1}\right) F_2. \qquad (3.20)$$

In our study, the calculation of the inverse matrices M^{-1} and H^{-1} was not possible algebraically due to the complexity of the expressions of the elements of the matrix P. To avoid the calculation of the inverse of matrix H algebraically we evaluate the matrix at the operation point q_e, and afterward, we calculate numerically the inverse of the matrix as $(H(q_e))^{-1}$. The linearization of the model (3.19) can be performed directly as follows:

$$\begin{bmatrix} \delta \ddot{q} \\ \delta \lambda \end{bmatrix} = \underbrace{\frac{\partial \Gamma}{\partial q} \Big|_{x_e}}_{A_1} \delta q + \underbrace{\frac{\partial \Gamma}{\partial \dot{q}} \Big|_{x_e}}_{A_2} \delta \dot{q} + \underbrace{\frac{\partial \Gamma}{\partial \tau} \Big|_{x_e}}_{B_1} \delta \tau \qquad (x_e = q_e, \dot{q}_e, \tau_e) \qquad (3.21)$$

The terms of the equation (3.21) can be calculated as:

- $\frac{\partial \Gamma}{\partial q} = (H(q_e))^{-1} \frac{\partial F}{\partial q} - (H(q_e))^{-1} \frac{\partial (H(q_e))}{\partial q} (H(q_e))^{-1} F$ that provides a matrix A_1 of dimension $((\tilde{g} + 2n) \times \tilde{g})$.

- $\frac{\partial \Gamma}{\partial \dot{q}} = (H(q_e))^{-1} \frac{\partial F}{\partial \dot{q}}$ that provides a matrix A_2 of dimension $((\tilde{g} + 2n) \times \tilde{g})$.

- $\frac{\partial \Gamma}{\partial \tau} = (H(q_e))^{-1} \frac{\partial F}{\partial \tau}$ that provides a matrix B_1 of dimension $((\tilde{g} + 2n) \times n)$.

where $\tilde{g} = (3n + 3)$ is the number of the system variables. Then, the linear direct kinematic model can be written as:

$$\ddot{q} = A_{11} q + A_{12} \dot{q} + B_{11} \tau \qquad (3.22)$$

in which $A_{11} = A_{1_{(\tilde{g} \times \tilde{g})}}$, $A_{12} = A_{2_{(\tilde{g} \times \tilde{g})}}$, and $B_{11} = B_{1_{(\tilde{g} \times n)}}$.

Considering $x = \begin{bmatrix} q^T & \dot{q}^T \end{bmatrix}^T$, the linear model can be expressed by the following state-space representation:

$$\begin{bmatrix} \dot{q} \\ \ddot{q} \end{bmatrix} = \underbrace{\begin{bmatrix} \mathbb{O}_{\tilde{g} \times \tilde{g}} & \mathbb{I}_{\tilde{g} \times \tilde{g}} \\ A_{11} & A_{12} \end{bmatrix}}_{A} \begin{bmatrix} q \\ \dot{q} \end{bmatrix} + \underbrace{\begin{bmatrix} \mathbb{O}_{\tilde{g} \times n} \\ B_{11} \end{bmatrix}}_{B} \tau. \qquad (3.23)$$

After the linearization, the controllability and observability of the state space representation were tested using the Popov-Belevitch-Hautus (PBH) test (condition (iii) in Theorem (1) and Theorem (2) in Appendix (B.1)). The linear state-space representation was found non-controllable and non-observable due to the variables' dependency. Even the reduced order linear model was also found non-controllable and non-observable, implying that the linear model is no longer valid for the synthesis. We tested also the conditioning of the matrices and we found that there exists an ill-conditioning of matrices that can be caused by numerical issues.

Second method: linearization as a descriptor model

The model in (3.18) was rewritten in the following form:

$$\underbrace{\begin{bmatrix} M & -A^T \\ A & \mathbb{O} \end{bmatrix}}_{H} \begin{bmatrix} \ddot{q} \\ \lambda \end{bmatrix} = \begin{bmatrix} F_1 \\ F_2 \end{bmatrix} \Rightarrow \begin{cases} M\,\ddot{q} = \underbrace{F_1 + A^T\,\lambda}_{\tilde{F_1}} \\ A\,\ddot{q} = F_2 \end{cases} \tag{3.24}$$

and then the model in (3.24) was linearized directly without inverting the matrix H as follows:

$$\underbrace{M|_{x_e}}_{N_0}\, \delta\ddot{q} = \underbrace{\frac{\partial F_1}{\partial q}\bigg|_{x_e}}_{A_1}\delta q + \underbrace{\frac{\partial F_1}{\partial \dot{q}}\bigg|_{x_e}}_{A_2}\delta\dot{q} + \underbrace{\frac{\partial F_1}{\partial \lambda}\bigg|_{x_e}}_{A_3}\delta\lambda + \underbrace{\frac{\partial F_1}{\partial \tau}\bigg|_{x_e}}_{B_1}\delta\tau \tag{3.25}$$

$$\underbrace{A\,|_{x_e}}_{A_0}\, \delta\ddot{q} = \underbrace{\frac{\partial F_2}{\partial q}\bigg|_{x_e}}_{A_4}\delta q + \underbrace{\frac{\partial F_2}{\partial \dot{q}}\bigg|_{x_e}}_{A_5}\delta\dot{q} \qquad (x_e = q_e, \dot{q}_e, \lambda_e, \tau_e) \tag{3.26}$$

The obtained linearized model is a descriptor model with state-space vector $\dot{x} = \begin{bmatrix} q & \dot{q} & \lambda \end{bmatrix}^T$ expressed in the following equation:

$$\underbrace{\begin{bmatrix} \mathbb{I} & \mathbb{O} & \mathbb{O} \\ \mathbb{O} & N_0 & \mathbb{O} \\ \mathbb{O} & A_0 & \mathbb{O} \end{bmatrix}}_{E} \begin{bmatrix} \dot{q} \\ \ddot{q} \\ \dot{\lambda} \end{bmatrix} = \underbrace{\begin{bmatrix} \mathbb{O} & \mathbb{I} & \mathbb{O} \\ A_1 & A_2 & A_3 \\ A_4 & A_5 & \mathbb{O} \end{bmatrix}}_{A} \begin{bmatrix} q \\ \dot{q} \\ \lambda \end{bmatrix} + \underbrace{\begin{bmatrix} \mathbb{O} \\ B_1 \\ \mathbb{O} \end{bmatrix}}_{B} \tau. \tag{3.27}$$

Analysis and control synthesis methods for descriptor models are available and presented by Duan (2010). Nonetheless, the PHB test of controllability and observability failed also for the same reason as in the first approach.

To solve the problem of variables' dependency, we then had no other choice than to reduce the redundant states (variables) to obtain an ordinary differential equation model (ODE model) with a minimal state-space representation. Matrix expressions of the reduced model are derived from the DAE model to simplify both symbolic and numerical calculations. Before performing this transformation on the complex flexible cable robot model, we tested this approach of transformation on a simple model (Slider-crank mechanism) to verify if it solve the problem of the non-controllability and non-observability of the linear DAE model. We found that in the case of this simple model the linearization of the DAE model provided a non-controllable and non observable model whereas the linear ODE model obtained after transformation was found controllable and observable (see Appendix (A.2).

3.2.6 Transformation into an ODE model

Due to the geometric constraints, some variables can be expressed according to others using their dependency relationship. Considering the 3n+3 variables of the system and assuming that the translation and orientation variables of the platform must remain in the new generalized coordinates vector, there are three possible solutions to perform this reduction of constraints:

- Express the lengths l_i and the flexibility modes w_i of cables as functions of the orientations φ_i and the platform pose (x_p, y_p, α). Solving the problem appeared intractable with standard mathematical tools.

- Express the orientations φ_i and the flexibility modes w_i of cables as functions of the lengths l_i and the platform pose (x_p, y_p, α). This solution has been discarded even if tractable, as the flexibility modes can take two possible values (positive or negative) for a given cable length.

- Express the lengths l_i and the orientations φ_i of cables as a function of the flexibility modes w_i and the platform pose (x_p, y_p, α). This solution is unique and tractable which makes it suitable to perform the reduction of constraints.

Considering the last suitable solution for the reduction, we obtain the new generalized coordinates vector of the ODE model that includes only the platform pose and cables' flexibility modes as: $q_r = \begin{bmatrix} w_1 \dots w_n & x_p & y_p & \alpha \end{bmatrix}^T$ with $n + 3$ entries as presented in the following section.

3.2.7 Reduction constraints

Geometric model
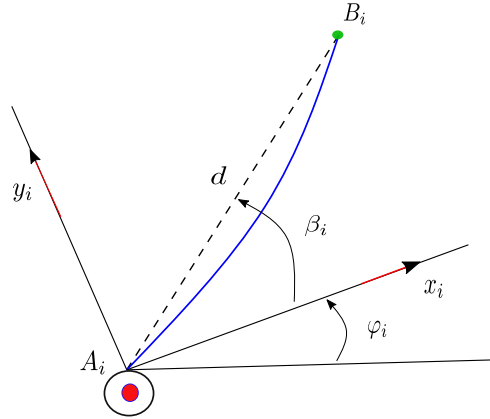
Figure 3.5: Geometry of the cable #i.

As represented in Figure (3.5), we can express the distance d between the winch drum's positions A_i and the platform attachment points B_i as follows:

$$(x_{B_i} - x_{A_i})^2 + (y_{B_i} - y_{A_i})^2 = (l_i + \delta x_i)^2 + (\delta y_i)^2. \qquad (3.28)$$

Using the equations (3.3) and (3.2), and considering that $x = l_i$ we obtain:

$$(x_{B_i} - x_{A_i})^2 + (y_{B_i} - y_{A_i})^2 = l_i^2 \left(1 - \frac{1}{3} w_i^2 + \frac{4}{9} w_i^4\right) \qquad (3.29)$$

The length of the cable can be expressed as a function of the variables (w_i, x_p, y_p, α) as:

$$l_i(w_i, x_p, y_p, \alpha) = 3 \sqrt{\frac{(x_{B_i}(x_p, \alpha) - x_{A_i})^2 + (y_{B_i}(y_p, \alpha) - x_{A_i})^2}{9 - 3\,w_i^2 + 4\,w_i^4}} \quad (i = 1 \dots n). \tag{3.30}$$

From Figure (3.5), we can also express the orientations of the cables as a function of the new generalized coordinates vector (w_i, x_p, y_p, α) as follows:

$$\varphi_i(w_i, x_p, y_p, \alpha) = atan2(y_{B_i} - y_{A_i}, x_{B_i} - x_{A_i}) - \beta_i \tag{3.31}$$

with:

$$\beta_i = atan2(\delta y_i, l_i - \delta x_i) \tag{3.32}$$

Kinematic model

The time derivatives of the two last expressions can be calculated as follows:

$$\dot{l}_i(q_r, \dot{q}_r) = \frac{\partial l_i}{\partial w_i} \dot{w}_i + \frac{\partial l_i}{\partial x_p} \dot{x}_p + \frac{\partial l_i}{\partial y_p} \dot{y}_p + \frac{\partial l_i}{\partial \alpha} \dot{\alpha} \tag{3.33}$$

$$\dot{\varphi}_i(q_r, \dot{q}_r) = \frac{\partial \varphi_i}{\partial w_i} \dot{w}_i + \frac{\partial \varphi_i}{\partial x_p} \dot{x}_p + \frac{\partial \varphi_i}{\partial y_p} \dot{y}_p + \frac{\partial \varphi_i}{\partial \alpha} \dot{\alpha}. \tag{3.34}$$

The generalized coordinates vector q can be computed as function of the new generalized coordinates vectors q_r using the following relation:

$$\dot{q} = \tilde{B}(q_r)\,\dot{q}_r \tag{3.35}$$

where the matrix $\tilde{B}$ is calculated as follows:

$$\underbrace{\begin{bmatrix} \dot{l}_1 \\ \dot{w}_1 \\ \dot{\varphi}_1 \\ \vdots \\ \dot{l}_n \\ \dot{w}_n \\ \dot{\varphi}_n \\ \dot{x}_p \\ \dot{y}_p \\ \dot{\alpha} \end{bmatrix}}_{\dot{q}} = \underbrace{\begin{bmatrix} \frac{\partial l_1}{\partial w_1} & \cdots & \cdots & \frac{\partial l_1}{\partial x_p} & \frac{\partial l_1}{\partial y_p} & \frac{\partial l_1}{\partial \alpha} \\ 1 & \cdots & \cdots & 0 & 0 & 0 \\ \frac{\partial \varphi_1}{\partial w_1} & \cdots & \cdots & \frac{\partial \varphi_1}{\partial x_p} & \frac{\partial \varphi_1}{\partial y_p} & \frac{\partial \varphi_1}{\partial \alpha} \\ \vdots & \cdots & \cdots & \cdots & \cdots & \vdots \\ 0 & \cdots & \frac{\partial l_n}{\partial w_n} & \frac{\partial l_n}{\partial x_p} & \frac{\partial l_n}{\partial y_p} & \frac{\partial l_n}{\partial \alpha} \\ 0 & \cdots & 1 & 0 & 0 & 0 \\ 0 & \cdots & \frac{\partial \varphi_n}{\partial w_n} & \frac{\partial \varphi_n}{\partial x_p} & \frac{\partial \varphi_n}{\partial y_p} & \frac{\partial \varphi_n}{\partial \alpha} \\ 0 & \cdots & \cdots & 1 & 0 & 0 \\ 0 & \cdots & \cdots & 0 & 1 & 0 \\ 0 & \cdots & \cdots & 0 & 0 & 1 \end{bmatrix}}_{\tilde{B}(q_r)} \underbrace{\begin{bmatrix} \dot{w}_1 \\ \vdots \\ \dot{w}_n \\ \dot{x}_p \\ \dot{y}_p \\ \dot{\alpha} \end{bmatrix}}_{\dot{q}_r}. \tag{3.36}$$

Dynamic model (ODE model)

Using the equation (3.36), then the kinetic energy in equation (3.14) can be expressed with the minimal parametrization as follows:

$$K_r(q_r, \dot{q}_r) = \frac{1}{2} \dot{q}_r^T \underbrace{\tilde{B}^T M \tilde{B}}_{M_r} \dot{q}_r. \tag{3.37}$$

The generalized forces relative to the new generalized coordinates q_r are expressed as:

$$Q_{r_j} = -\frac{\partial V(q_r)}{\partial q_{r_j}} - \frac{\tau_i}{r} \sum_{i=0}^{n} \frac{\partial \dot{l}_i(q_r)}{\partial \dot{q}_{r_j}} \quad (j = 1, \dots, n+3). \tag{3.38}$$

Then, the dynamic model in (3.17) is expressed in the ODE form as follows:

$$M_r(q_r)\, \ddot{q}_r = \underbrace{\frac{\partial K_r(q_r, \dot{q}_r)}{\partial q_r}}_{C_r} + \ Q_r - \dot{M}_r(q_r, \dot{q}_r)\, \dot{q}_r \tag{3.39}$$

where $Q_r(q_r, \tau)$ is the column matrix of generalized forces, and
$C_r = \left[\frac{1}{2}\, q_r^T\, \frac{\partial M_r}{\partial q_{r_1}}\, q_r^T \quad | \dots | \quad \frac{1}{2}\, q_r^T\, \frac{\partial M_r}{\partial q_{r_{n+3}}}\, q_r^T \right]^T$.

In terms of input-output behavior, the DEA model (3.39) and the ODE model (3.18) are equivalent.

3.2.8 Linearization of the ODE model

According to the following control and linearization scheme presented in Figure (3.6), we linearized the ODE model for synthesizing the $\mathcal{H}_\infty$ controller.
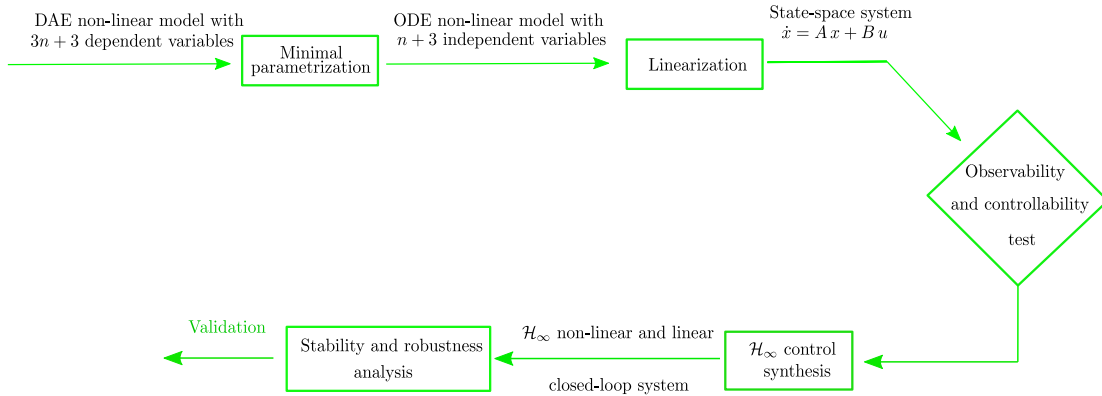

Figure 3.6: Control and linearization methodology for the ODE model.

The matrix M_r is invertible as long as we remain in the workspace, then the accelerations $\ddot{q}_r$ in equation (3.39) can be expressed as follows:

$$\ddot{q}_r = M_r^{-1} \underbrace{(C_r + Q_r - \dot{M}_r\, \dot{q}_r)}_{F_r} = \Gamma_r. \tag{3.40}$$

We can obtain the linear ODE model with the following equation:

$$\delta\ddot{q}_r = \underbrace{\frac{\partial\Gamma_r}{\partial q_r}\Big|_{x_{r_e}}}_{A_{r_1}}\delta q_r + \underbrace{\frac{\partial\Gamma_r}{\partial\dot{q}_r}\Big|_{x_{r_e}}}_{A_{r_2}}\delta\dot{q}_r + \underbrace{\frac{\partial\Gamma_r}{\partial\tau}\Big|_{x_{r_e}}}_{B_{r_1}}\delta\tau \qquad (x_{r_e} = q_{r_e}, \dot{q}_{r_e}, \tau_{r_e}). \qquad (3.41)$$

We confront the same difficulties of calculating the inverse of the matrix M_r algebraically as for the case of the DEA model in section (3.2.5). The matrix M_r is evaluated for the operating point q_{r_e}, and then the inverse of the matrix is computed numerically. The terms in the equation (3.41) can be calculated as:

- $\frac{\partial\Gamma_r}{\partial q_r} = (M_r(q_{r_e}))^{-1}\frac{\partial F_r}{\partial q_r} - (M_r(q_{r_e}))^{-1}\frac{\partial(M_r(q_{r_e}))}{\partial q_r}(M_r(q_{r_e}))^{-1}F_r$ that provides a matrix A_{r_1}.

- $\frac{\partial\Gamma_r}{\partial\dot{q}_r} = (M_r(q_{r_e})^{-1}\frac{\partial F_r}{\partial\dot{q}_r}$ that provides a matrix A_{r_2}.

- $\frac{\partial\Gamma_r}{\partial\tau} = (M_r(q_{r_e}))^{-1}\frac{\partial F_r}{\partial\tau}$ that provides a matrix B_{r_1}.

Considering the state-space vector $\dot{x} = \begin{bmatrix} q_r & \dot{q}_r \end{bmatrix}^T$, the ODE linear model can be expressed by the following state-space representation as follows:

$$\begin{bmatrix} \dot{q}_r \\ \ddot{q}_r \end{bmatrix} = \underbrace{\begin{bmatrix} \mathbb{O} & \mathbb{I} \\ A_{r_1} & A_{r_2} \end{bmatrix}}_{A_r}\begin{bmatrix} q_r \\ \dot{q}_r \end{bmatrix} + \underbrace{\begin{bmatrix} \mathbb{O} \\ B_{r_1} \end{bmatrix}}_{B_r}\tau. \qquad (3.42)$$

The linear ODE state-space representation was found controllable and observable using the PBH test (see appendix B.1), implying that the linear model is valid for the synthesis of the $\mathcal{H}_\infty$ controller.

3.3 Geometric validation of the flexible cable model

It should be noted that the work in this section was developed as part of the supervision of a project presented by Alexis Boulay and Vincent Daniele, students in their 3rd year of engineering, and an internship by Frédéric Le Quillio, a student in 2nd year of engineering in Telecom Physique Strasbourg.

When observing a cable during movements with fast dynamics, the flexibilities of cables can be perceived by the human eye. The objective of the validation is to calculate the positions of the cable points in the INCA plan from a video and compare these cable points to the model of the cable with flexibility presented in section (3.2). This validation verifies that this model matches well the real behavior of the cable during movement. This video must be recovered from an experimental test during the operation of the INCA cable robot prototype.

The validation was performed by estimating the evolution of the model's variables: deformation, orientation, and length of the cables. This identification of the model was accomplished in three steps:

- Taking pictures and video by a fixed position of a smartphone.

- Extraction of the cable's points from images.

- Calibration of the cameras to obtain the intrinsic and extrinsic parameters to calculate the projection matrix which performs the reconstruction of the cable variables in the INCA plan.

- Estimation of the cable variables by minimizing cost functions which are least squares between the cable model and the reconstructed cable point obtained from the experimental tests (the video).

The sequence of this algorithm is illustrated in the scheme in Figure (3.7).
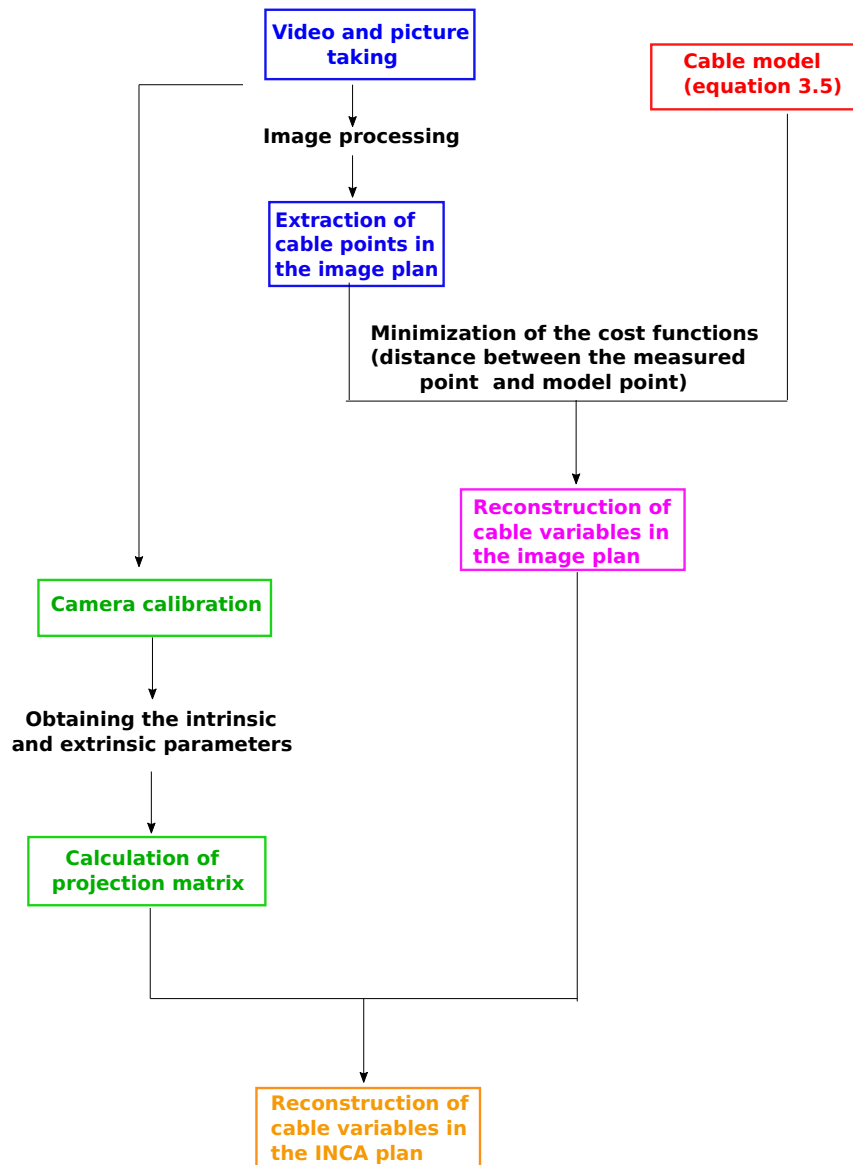
Figure 3.7: Steps of the algorithm of model geometric validation.

3.3.1   Video and pictures acquisition

Several considerations were taken into account to record during the experimental tests. These considerations using simple equipment to obtain a good quality of video and pictures that must be with the same resolutions:

- To enhance contrast and facilitate cable detection in the video, we placed a black tablecloth on the floor (see Figure (3.10)).

- To avoid the appearance of light flickering in the video, we used LED light projectors with high-frequency ($\approx$ 100 Hz) (see Figure (3.8b)) for the room lighting. Notice that the light flickering happened due to the frequency of the acquisition in slow motion, which is higher than the frequency of neon light that was in the room.

- To acquire images with a clearer deformation of the cables, we used an iPhone to take the video in slow motion with a frequency of 240 FPS (Frames Per Second) (this mode is now generally available with standard smartphones).

- To maintain the camera in a fixed position during the whole experiment, we fixed the iPhone to a stand (see Figure (3.8a)).

- To obtain pictures (to calibrate the camera) and video (to perform model validation) with the same resolution, we recorded the video and used the VLC video player to take screenshots (pictures).

- To perform the calibration step, we take the pictures of the cable that consider checkerboard pattern (see Figure 3.10). Note that we assume that the cable is located in the plane where the checkerboard is placed (the real distance of 1.2 cm along the Z axis is therefore assumed to be null).
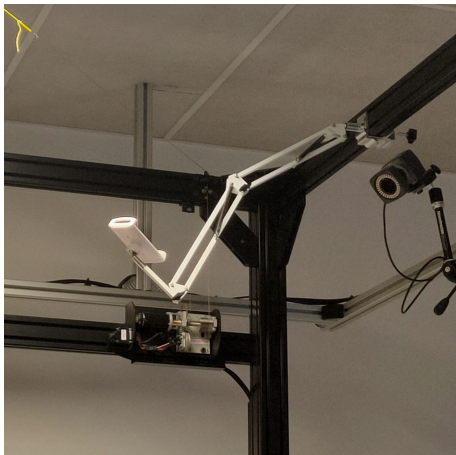
(a) The camera stand.   (b) The continuous light projector.

Figure 3.8: The camera stand and continuous light projector.

3.3.2 Extraction of cable points using image processing

To extract points of the cable from a an image, a preprocessing was performed first on the original image (see Figure 3.9) to transform it into a binary image. Then, to extract the cables from the binarized image, we go through three steps: adaptive thresholding, dilation, and erosion of the image. To accomplish that, we start by isolating each group of pixels with an 8-neighborhood using the `bwlabel`

Matlab function[2] to obtain a list of the different grouped pixels. Then, we used the `regionsprop` Matlab function [3] with the options `Perimeter` and `Area`, which allows associating with each of these groups of pixels the perimeter and the area of the groups. After that, the group of pixels with the largest perimeter is selected to represent the shape of the cable (see Figure (3.9)).

For the extraction of the intersection point of cables, we use the same principle as previously, with the difference here, we will not seek to detect a single cable but two. Once our two cables are extracted, we aim to slenderize the cable into a single-pixel thick line, extract the coordinates of these cables, and then select the intersection between the cables by defining the lines resulting from these two sets of points using the `polyfit` and `polyval` Matlab functions[4].
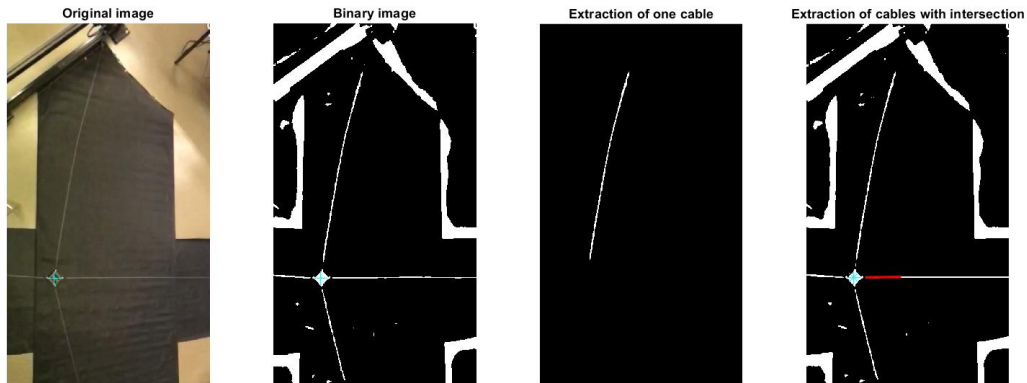
Figure 3.9: Extraction of cable from stream video (a. original image b. binary image c. extraction of one cable d. extraction of cables with intersection).

3.3.3 Camera calibration

To validate experimentally our results, it is necessary to transform the cable data obtained previously in section (3.3.2) in the image plane into a real space frame (in INCA plane).

To establish that, we modeled the camera considering the perspective projection[5] based on the pinhole camera model (Forsyth and Ponce (2011)). To perform this projection, we calibrate the camera to calculate the projection matrix M_P, which requires prior knowledge of the camera's intrinsic and extrinsic parameters (for more details about pinhole camera model see Appendix (A.4)).

To estimate the intrinsic and extrinsic parameters of the camera we used `cameraCalibrator` Matlab app [6] from the Vision toolbox. The calibration was performed considering a set of pictures of the environment taken from different angles and containing the calibration checkerboard pattern (see Figure 3.10 and

---

[2]To label the image with the 8 connectivity, each group of pixels is identified by a specific number.

[3]To calculate the perimeter and the area of each group.

[4]To retrieve the polynomial coefficients which represent the intersection and then draw this line.

[5]A geometric transformation performed by an optical system forms the picture of objects located in space and is used to represent objects in a picture.

[6]The app can be used to estimate camera intrinsic and extrinsic parameters by simply calling the app in the Matlab Command window and adding the set of pictures.

Figure 3.11). We can see in Figure 3.10 the detected points in 2D (in green) and the respectively reconstructed points in 3D (in red).

a. Picture 1.   b. Picture 2.   c. Picture 3.
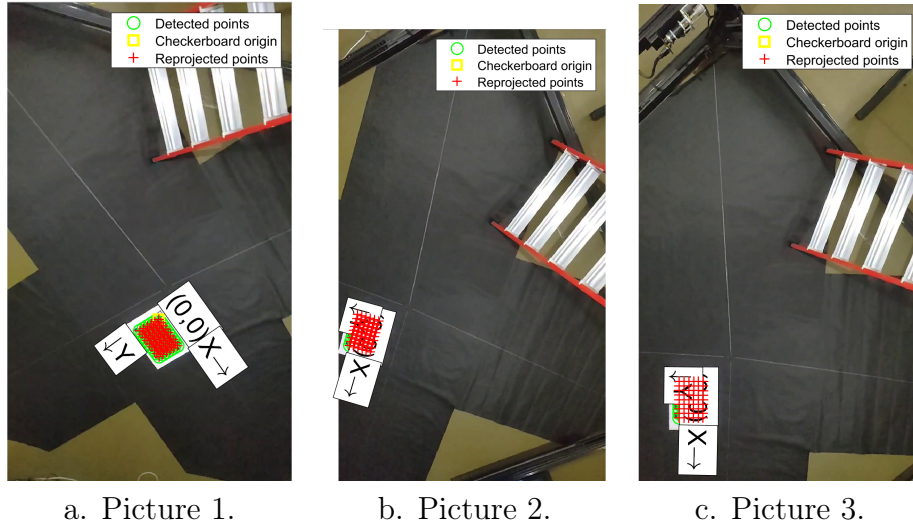
Figure 3.10: Set of pictures used for the calibration.

a. 3D view.   b. 2D x-z view.   c. 2D y-x view.
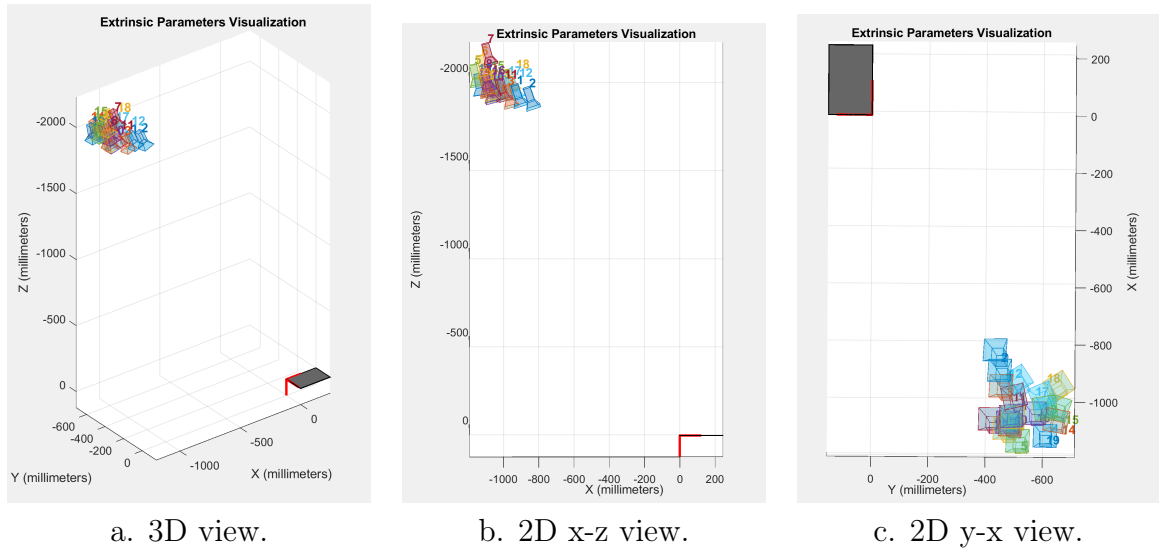
Figure 3.11: 3D representation of the position of our mobile camera in relation to the different views of the fixed calibration pattern.

The obtained intrinsic parameters matrix is given as follows:

$$M_{int} = \begin{pmatrix} 828.5979 & 0 & 0 \\ 0 & 831.3362 & 0 \\ 649.0655 & 358.5102 & 1 \end{pmatrix}$$

Once the projection matrix is obtained (for more details about the approach used of the projection matrix see appendix (A.4)), then the heterogeneous 3D coordinates $(X, Y, Z, 1)$ can be calculated using the matrix and homogeneous 2D coordinates $(u, v, 1)$ as:

65

$$\begin{bmatrix} u \\ v \\ 1 \end{bmatrix} = M_P^T \begin{bmatrix} X \\ Y \\ Z \\ 1 \end{bmatrix} \tag{3.43}$$

As we assumed that the cable is on the plane we can simplify the dimension of the projection matrix of dimension $M_P(4 \times 3)$ and into dimension $M_{PR}(3 \times 3)$ matrix by deleting the 3rd column ($Z = 0$).

$$\begin{bmatrix} X \\ Y \\ 1 \end{bmatrix} = M_{PR}^{T}{}^{-1} \begin{bmatrix} u \\ v \\ 1 \end{bmatrix} \tag{3.44}$$

3.3.4 Reconstruction of the cable variables

The extraction of the cable points allows us to obtain two sets of experimental coordinates (x_{data}, y_{data}) of the extracted cable. The cable starting point is considered to be known, either provided by the user or obtained via a pattern. The variable estimation is an optimization problem that aims to minimize a difference criterion between the measured cable points (x_{data}, y_{data}) and the model cable points (x_{model}, y_{model}) (calculated from the model in the equation (3.5)).

For the estimation of the cable's variables, two cost functions to be minimized have been implemented, these functions use the least squares criterion. In an internal step, we aim to find the optimal longitudinal position sk that minimizes the first Least Squares cost function (the distance between N of the cable model and the N of the measured point) in equation (3.45), while estimating flexibility w and orientation data φ by minimizing a second Least Squares cost function in external step in equation (3.46).

$$\underset{sk}{minimaze} \quad \frac{1}{N} \sum_{k=1}^{N} d_k. \tag{3.45}$$

$$\underset{w,\varphi}{minimaze} \quad \frac{1}{N} \sum_{k=1}^{N} d_k \tag{3.46}$$

where $d_k = (x_{data_k} - x_{model}(sk, w, \varphi))^2 + (y_{data_k} - y_{model}(sk, w, \varphi))^2$.

For this step of optimization, we used two Matlab functions, such as `pdist` with the option `euclidean` to calculate the euclidean distance between pairs of observations points and the Matlab function `fminseach` for minimizing the cost function.

3.3.5 Verification of the obtained results

The optimization results are represented in Figure (3.12), where the experimental points are in black, The model is in red and the cable's ends are in blue.

We estimate a cable length of 1.83 m, and we measure, using a meter, a length of 1.77 m, so we find a relative difference of about 3% and an RMS of 0.04 m. This discrepancy is due to uncertainty in selecting the points of the image whose distance is known. However, the cable optimization results show that the proposed theoretical model approximates well the actual behavior of the prototype robot.
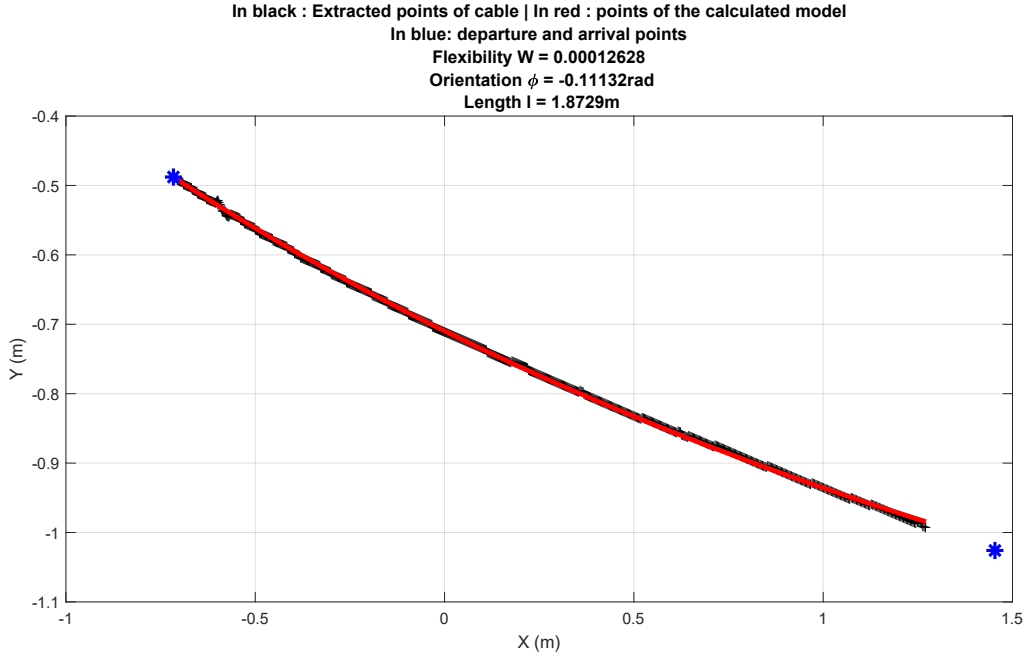
Figure 3.12: The validation of the geometric model of flexible cable from the video stream.

To verify the estimation of the cable's orientation and assess the accuracy, we filmed different videos of the cable with different orientations but in a static state without movement. We repeat the experience three times for the following manually measured orientations 3.5^o, 8.5^o, and 9.5^o. Using the validation algorithm and for the three different considered scenarios, we obtained the following estimated orientation values 4.4^o, 8.4^o and 10.5^o, respectively with RMS of 0.7789^o.

The time evolution of the estimated cable's variables is presented in Figure (3.13). The continuity of the evolution of the variable in the results proves the hypothesis that assumes the continuity of the evolution of the cable's variables due to the fact that the video is analyzed frame by frame when the cable is in motion.

3.4   Conclusion

The modeling process presented in the chapter (2) was extended in this chapter to take into account the flexibility of the cables and modeled it using the assumed modes approach to obtain a DAE model. Geometric validation using a video taken during the operation of the INCA robot was performed to verify and confirm that the considered flexible cable robot geometric model represents the real behavior of the INCA cable robot.

A transformation of the DAE model into an ODE model considering a minimal parametrization has been taking place to avoid the dependency between variables that causes the non-controllability and non-observability of the linear model. After linearization of the dynamic model about the center of the workspace, the obtained nominal open-loop system was found controllable and observable, which makes it suitable for the $\mathcal{H}_\infty$ synthesis of the controller, the object of the next chapter (4).
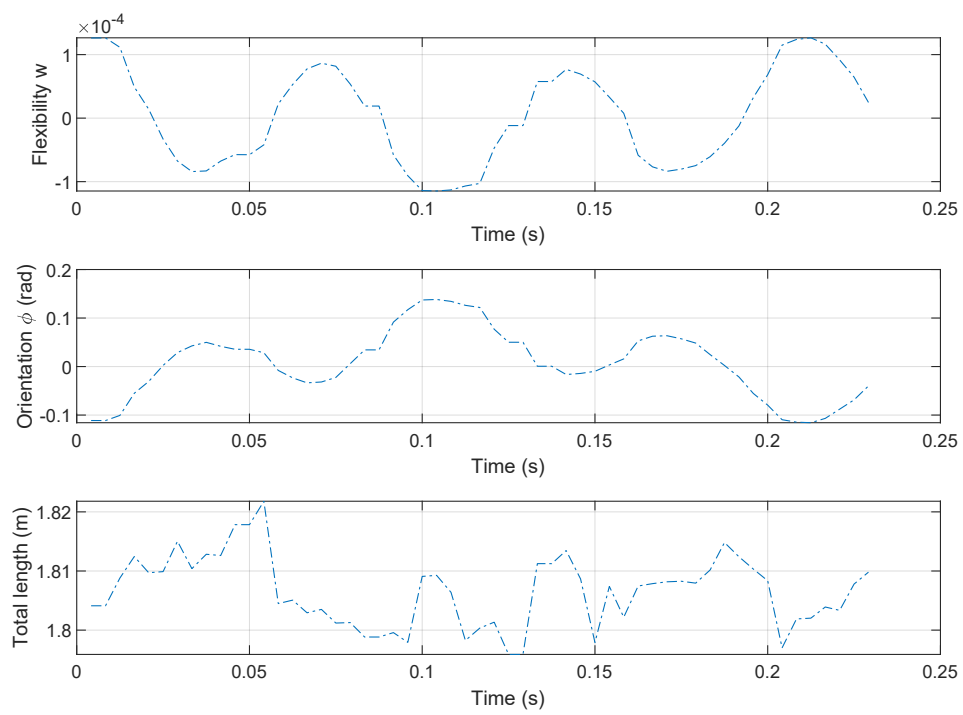
Figure 3.13: The time evolution of the estimated cable's variables (l, φ, w)

Chapter 4

$\mathcal{H}_\infty$ synthesis

4.1 Introduction

Since cable parallel robots are subject to variations in their own inertia as well as external disturbances, it is necessary to choose a control design method that can ensure good robustness. The $\mathcal{H}_\infty$ control is a synthesis method that was introduced by Zames and Helton in early 80s by (Helton (1978), Zames (1981)). This method deals with linear multi-variable systems for the purpose of ensuring the desired performance of the closed-loop system while ensuring good properties of disturbance rejection, trajectory tracking and robustness with respect to neglected dynamics.

In this chapter, the mathematical tools necessary for the definition of $\mathcal{H}_\infty$ synthesis will be briefly exposed. Then, we mainly expose the theoretical approach to follow for the calculation of the $\mathcal{H}_\infty$ controller based on the solution of the Riccati equations. Finally, we illustrate the results of the frequency response and the simulation of the closed-loop systems with the obtained $\mathcal{H}_\infty$ controller in order to control the pose of the platform and the mean tensions of cables for the case of 3 flexible cables robot with mass-point and a for the case of 4 flexible cable robot with a platform.

4.2 Performance and stability of feedback systems

The $\mathcal{H}_\infty$[1] synthesis submits a general framework for the control of linear time-invariant (LTI) systems by manipulating some frequency concepts. Its interest is to design a dynamic controllers by considering the objectives of the closed-loop performance, such as stability, rapidity, precision in tracking trajectories and robustness, all by tuning the different transfert dynamics between signals as reported by Duc (2022).

The standard control feedback scheme is illustrated in Figure (4.1). The system $G(s)$ that includes n_u controlled inputs and n_y measured outputs is controlled by means of the controller $K(s)$ with output feedback. The other signals are expressed as: the reference $r(t)$, the error $e(t)$, the control signal $u(t)$, the disturbance on the input of the system $d(t)$, the controlled signal $y(t)$, the measurement noise $b_m(t)$ and the measurement signal $y_m(t)$.

---

[1]The $\mathcal{H}_\infty$ norm is the maximum singular value of $G(j\omega)$ $\forall \omega \in \mathbb{R}^+$ see Appendix (B.2.1) and (B.2.3).
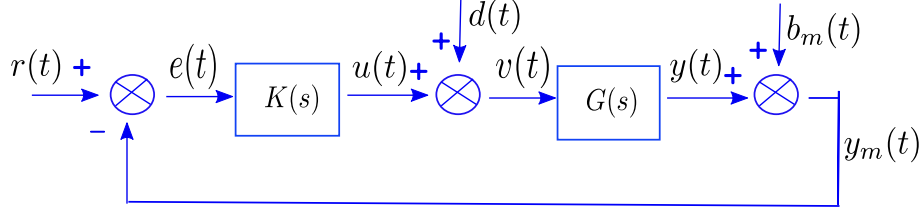
Figure 4.1: Standard control feedback scheme

The objective of the control is to make $y(t)$ tend asymptotically to $r(t)$ in the presence of disturbances $d(t)$ and measurement noise $b_m(t)$. The performances of the closed-loop system can be characterized by some transfer matrices. Generally, we notice the closed-loop transfer $T_{zw}(s)$ between the exogenous inputs w and the performance outputs z, the sensibility on the input which is the closed-loop transfer $S_u(s) = T_{vd}(s) = (\mathbb{I}_{ny} + K(s)\,G(s))^{-1}$ and the sensibility on the output which is the closed-loop transfer $S_y(s) = T_{er}(s)$. We can calculate the different closed-loop transfers as:

$$
\begin{bmatrix} e \\ u \\ v \\ y \\ y_m \end{bmatrix} = \begin{bmatrix} S_y(s) & -S_y(s)\,G(s) & -S_y(s) \\ S_u(s)\,K(s) & -S_u(s)\,K(s)\,G(s) & -S_u(s)\,K(s) \\ S_u(s)\,K(s) & S_u(s) & -S_u(s)\,K(s) \\ S_y(s)\,G(s)\,K(s) & S_y(s)\,G(s) & -S_y(s)\,G(s)\,K(s) \\ S_y(s)\,G(s)\,K(s) & S_y(s)\,G(s) & -S_y(s) \end{bmatrix} \begin{bmatrix} r \\ d \\ b_m \end{bmatrix} \qquad (4.1)
$$

The different performance criteria can be described as follows:

- **Stability margin**

  The gain, phase and, delay margins are not sufficient to ensure good robustness. Then, to ensure stability it is therefore essential that the minimal distance from the Nyquist locus to critical point -1 be sufficient. This distance is the modulus margin and is calculated for multivariable case as:

  $$
  \Delta_M = \frac{1}{\|S_y(s)\|_\infty} \qquad (4.2)
  $$

- **Precision**

  The static error against the unit step on the reference $r(t)$ (error of position) is given by $\bar{\sigma}(S_y(0))$. The computation of this static error is performed using the theorem of the final value as:

  $$
  \varepsilon_p = \lim_{s \to 0} s\,E(s) = \lim_{s \to 0} s\,T_{er}(s)\,R(s) = S_y(0). \qquad (4.3)
  $$

- **Bandwidth**

  To obtain a good trajectory tracking behavior, the transfer $T_{er}(s)$ must behave like a low-pass filter with a cut-off frequency sufficiently high at the axis -3 dB. We note that from the bandwidth of this transfer between the reference $r(t)$ and the error $e(t)$, we can conclude on the closed-loop system rapidity.

70

- **Disturbance rejection**

  In order to have a good disturbance rejection behavior, it is necessary that the transfer $T_{ed}(s) = -S_y(s)\,G(s)$ between the disturbance $d(t)$ and the error $e(t)$ be the weakest possible in low frequency. For this transfer, a band-pass filter shape provides a good performance in presence of input disturbances.

- **Measurement noise attenuation**

  The measurement noise $b_m(t)$ adversely impacts the control signal. Then to limit this amplification of the effect of measurement noise on the control signal, the closed-loop transfer $T_{ur}(s) = -K(s)\,S_y(s)\,G(s)$ must have a decreasing gain of the controller in high frequencies that is what we call the "roll-off effect". The attenuation of the gain at high frequencies leads to good robustness concerning unmodeled high-frequency dynamics that can cause stability issues.

4.3 Standard $\mathcal{H}_\infty$ synthesis

4.3.1 Standard scheme of the $\mathcal{H}_\infty$ synthesis

The standard scheme of the $\mathcal{H}_\infty$ synthesis is illustrated in Figure (4.2), where the plant $P(s)$ system and the controller $K(s)$ are connected through feedback called the linear fractional transformation (LFT).
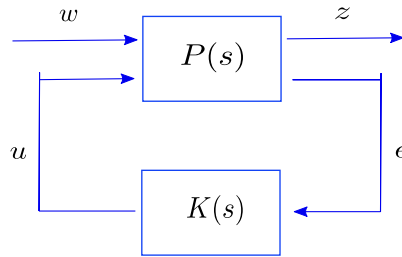
Figure 4.2: Standard scheme of the $\mathcal{H}_\infty$ synthesis

The state-space representation of the plant system is described as:

$$P : \begin{cases} \dot{x}(t) = A\,x(t) + B_1\,w(t) + B_2\,u(t) \\ z(t) = C_1\,x(t) + D_{11}\,w(t) + D_{12}\,u(t) \\ e(t) = C_2\,x(t) + D_{21}\,w(t) + D_{22}\,u(t) \end{cases} \tag{4.4}$$

where $x(t) \in \mathbb{R}^{n_x}$ is the state space vector while n_x is the order of the system, $w(t) \in \mathbb{R}^{n_w}$ is the exogenous input vector, $z(t) \in \mathbb{R}^{n_z}$ is the vector of the performance outputs, $e(t) \in \mathbb{R}^{n_y}$ is the vector of error and the $u(t) \in \mathbb{R}^{n_u}$ is the control input vector. Notice that signals $w(t)$ and $z(t)$ define the performance channels guaranteeing the desired performance and the signals $e(t)$ and $u(t)$ describe the control channel that connects the plant $P(s)$ to the controller $K(s)$.

The transfer matrix $P(s)^2$ which models the dynamic interconnections between the two inputs and the two outputs (w, u, z, e) is represented as follows:

---

[2]s denotes the variable of Laplace.

$$\begin{bmatrix} z(s) \\ e(s) \end{bmatrix} = \underbrace{\begin{bmatrix} P_{zw}(s) & P_{zu}(s) \\ P_{ez}(s) & P_{eu}(s) \end{bmatrix}}_{P(s)} \begin{bmatrix} w(s) \\ u(s) \end{bmatrix}. \tag{4.5}$$

The state-space representation of the controller $K(s)$ is described as follows:

$$K : \begin{cases} \dot{x}_K(t) = A_K x_K(t) + B_K \, e(t) \\ u(t) = C_K x_K + D_K \, e(t) \end{cases} \tag{4.6}$$

and the transfer matrix of the controller $K(s)$ is described as following:

$$K(s) : \left[\begin{array}{c|c} A_K & B_K \\ \hline C_K & D_K \end{array} \right] = C_K (sI - A_K)^{-1} B_K + D_K \tag{4.7}$$

with $x_K \in \mathbb{R}^{n_k}$ is the state vector of the controller K, n_k the order of the controller and A_K, B_K, C_K and D_K are a real constant matrices.

The aim to design the controller is to find the matrices (A_K, B_K, C_K, D_K) that satisfy the design requirements of the closed-loop.

The closed-loop transfer function from w to z is given by the following LFT (Zhou et al. (1996)):

$$T_{z \to w}(K) = P_{zw} + P_{zu} K (I - P_{eu} K)^{-1} P_{ez} \tag{4.8}$$

4.3.2 Problem of the $\mathcal{H}_\infty$ synthesis

The aim of the $\mathcal{H}_\infty$ synthesis is in addition to stabilizing the system, to minimize the impact of the exogenous inputs w on the performance outputs z. This minimization is performed by a control law $u = K(s) \, e$. This impact on the system is measured by the $\mathcal{H}_\infty$ norm, i.e. the norm on the system induced by the l_2 norm of signals z and w (see Appendix (B.2.2)):

$$\|T_{zw}(K)\|_\infty = \sup_{w \neq 0} \frac{\|z\|_2}{\|w\|_2} \tag{4.9}$$

The optimal standard $\mathcal{H}_\infty$ control problem consists of finding the stabilizing controller $K(s)$ that makes the closed-loop system internally stable and minimizes the $\mathcal{H}_\infty$ norm of the transfer function $T_{z \to w}(K)$ as follows:

$$\min_{K(s) \quad stabilizes \quad (4.5)} \|T_{z \to w}(K)\|_\infty \tag{4.10}$$

and the sub-optimal standard $\mathcal{H}_\infty$ control problem is represented as follows:

$$\|T_{z \to w}(K)\|_\infty < \gamma \tag{4.11}$$

for a fixed performance $\gamma > 0$.

There exist essentially two approaches to solve the standard $\mathcal{H}_\infty$ problem. These two approaches are the approach based on Riccati's algebraic equations proposed by Doyle et al. (1989), also called DGKF, from the abbreviation of the authors' names (Doyle, Glover, Khargonekar, and Francis) and the second approach uses

linear matrix inequality (LMI) presented by Gahinet and Apkarian (1994). The two approaches provide a controller of full order.

To perform the $\mathcal{H}_\infty$ synthesis, Matlab's Robust Control Toolbox has an available function which is the `hinfsyn` with as on option the different optimization algorithms for the resolutions of equations (Riccati or LMI), the two optimization algorithms are explained in details in Appendix (B.3) and Appendix (B.4) respectively.

Other functions are also available in this Toolbox as `hinfstruct` proposed by Apkarian and Noll (2006) and the `Hifoo` package proposed by Burke et al. (2006) used for the $\mathcal{H}_\infty$ tuning of fixed-structure controllers.

4.3.3 $\mathcal{H}_\infty$ synthesis objectives and methodology

To achieve the synthesis objectives, the $\mathcal{H}_\infty$ synthesis method consists in introducing weightings functions on the input and output signals as a form of linear filters and tuning them to achieve the synthesis objectives (see Figure (4.3)). This design problem of the $\mathcal{H}_\infty$ synthesis is usually called the $\mathcal{H}_\infty$ mixed sensitivity problem as presented by Duc (2022). Another design problem of the $\mathcal{H}_\infty$ synthesis is the loop-shaping problem that is based on using a pre-compensator and/or a post-compensator and the singular values of the nominal plant are shaped to give a desired open-loop shape as reported by Zhou et al. (1996). This design is well known for SISO systems and extended to MIMO systems by Doyle and Stein (1981) using LQG design technique.
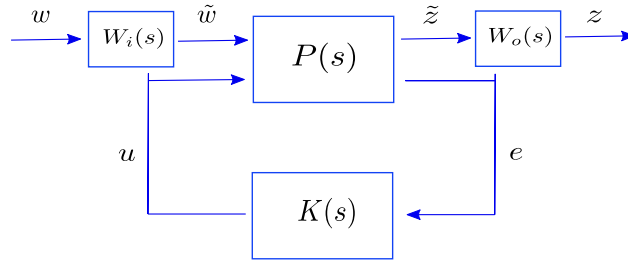
Figure 4.3: Standard $\mathcal{H}_\infty$ synthesis scheme with introduction of weighting functions

In the Figure (4.3), the extended plant is $P(s)$ with performance channel $\tilde{w} \to \tilde{z}$ and control channel $u \to e$, $(W_i(s), W_o(s))$ are the diagonal inputs and outputs weighting functions, i.e. $W_i(s) = W_{ip}.\mathbb{I}_{n_w}$, $p = 1, ..., n_w$ and, $W_o(s) = W_{ol}.\mathbb{I}_{n_z}$, $l = 1, ..., n_z$, where n_w and n_z are the dimensions of the exogenous inputs w and the performance outputs z respectively.

The $\mathcal{H}_\infty$ synthesis aims to design a controller $K(s)$ that stabilizes the closed-loop function while minimizing the impact of w on z. This impact is represented by the $\mathcal{H}_\infty$ norm of the closed-loop transfer function $\|T_{zw}(s)\|_\infty = \|W_o(s).T_{\tilde{z}\tilde{w}}(s).W_i(s)\|_\infty$ [3] that must be less then a performance criteria γ. The previous condition can be satisfied by tuning the weighting functions until meeting the required specifications. Thus the $\mathcal{H}_\infty$ synthesis enables the closed-loop transfer function to satisfy the following templates:

$$|T_{\tilde{z}\tilde{w}}(jw))| \leq \frac{\gamma}{|W_{ip}(jw)| . |W_{ol}(jw)|} \qquad \forall \ w \in \mathbb{R}^+ \qquad (4.12)$$

---

[3]Let $T_{\tilde{z}\tilde{w}}(s)$ denote the transfer of the system with $\tilde{w}$ and $\tilde{z}$ and is calculated by the linear fractional transformation as $T_{\tilde{z}\tilde{w}}(s) = \text{lft}(P(s), K(s))$.

where the frequency template is represented in the right-hand side of the inequality (4.12).

The obtained value of the performance criteria γ decides if the fixed performances through the frequency templates will be more or less achieved, then for a value less than 1 ($\gamma < 1$) the transfers carried out respect their templates and the fixed performances are improved and if the value is greater than 1 ($\gamma > 1$) then the templates are exceeded and the fixed performances will be degraded. So it is more convenient to choose the weighting functions by considering a performance criterion value lower than 1 or slightly higher than 1.

4.3.4 Different $\mathcal{H}_\infty$ synthesis schemes and choice of weighting functions

Several $\mathcal{H}_\infty$ synthesis schemes are possible, depending on the desired objectives and the difficulties encountered in practice. The idea is to choose the simplest scheme that can meet the specifications and analyze the obtained results. If the performance criteria are not achieved, we choose to move to a more complex scheme by adding performance signals and introducing them into the synthesis. The Figure (4.4) presents the four-block $\mathcal{H}_\infty$ synthesis scheme where $G(s)$ is a multi-variable system controlled by the controller $K(s)$ with output feedback, the input signals are $w(t) = [r(t)^T, d(t)^T]^T$, the output signals are $z(t) = [e(t)^T, u(t)^T]^T$, the input weighting functions are $W_i(s) = diag(\mathbb{I}_{ny \times ny}, W_d(s))$ and the output weighting functions are $W_o(s) = diag(W_e(s), W_u(s))$.
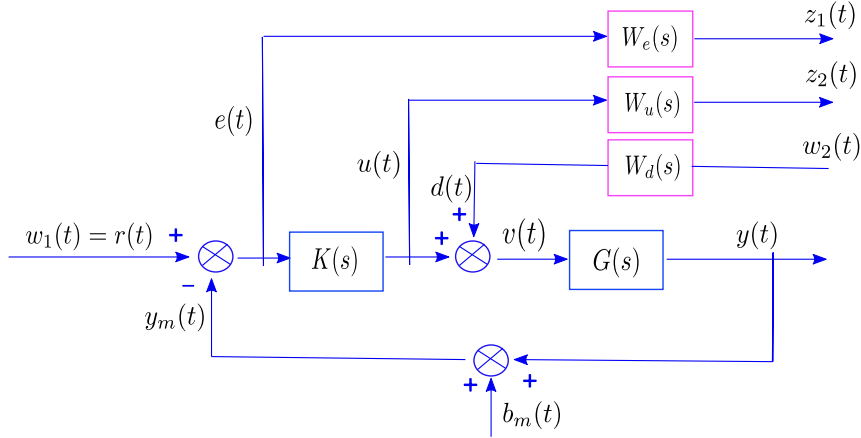
Figure 4.4: Four-block standard $\mathcal{H}_\infty$ synthesis scheme with weighting functions

The standard $\mathcal{H}_\infty$ problem can be written considering the closed-loop transfer as:

$$\left\| \underbrace{\begin{pmatrix} W_e(s)\, S_y(s) & -W_e(s)\, S_y(s)\, G(s)\, W_d(s) \\ W_u(s)\, K(s)\, S_y(s) & -W_u(s)\, K(s)\, S_y(s)\, G(s)\, W_d(s) \end{pmatrix}}_{T_{zw}(s)} \right\|_\infty \leq \gamma \qquad (4.13)$$

The $\mathcal{H}_\infty$ optimal corrector $K(s)$ allows the minimization of the different weighting transfers as follows:

$$\forall \omega \in \mathbb{R}: \begin{cases} |W_e(s)\,S_y(s)| \le \gamma \Leftrightarrow |S_y(s)| \le \dfrac{\gamma}{|W_e(s)|} \\[2mm] |W_u(s)\,K(s)\,S_y(s)| \le \gamma \Leftrightarrow |K(s)\,S_y(s)| \le \dfrac{\gamma}{|W_u(s)|} \\[2mm] |W_e(s)\,S_y(s)\,G(s)\,W_d(s)| \le \gamma \Leftrightarrow |S_y(s)\,G(s)| \le \dfrac{\gamma}{|W_e(s)\,W_d(s)|} \\[2mm] |W_u(s)\,K(s)\,G(s)\,W_d(s)| \le \gamma \Leftrightarrow |K(s)\,G(s)| \le \dfrac{\gamma}{|W_u(s)\,W_d(s)|} \end{cases} \tag{4.14}$$

The various synthesis schemes considered to describe the performances are presented in the following.

One-block synthesis scheme

The crucial transfer is the sensitivity $S_y(s)$ transfer which makes it possible to manage the rapidity (bandwidth), the stability margin, and the precision to achieve the performance of trajectory tracking. Thus, the simplest synthesis scheme consists in involving only the weighting function $W_e(s)$ during the synthesis. The weighting function $W_e(s)$ is chosen so that the frequency template $\frac{1}{W_e(s)}$ on the transfer $T_{er}(s)$ has low-pass characteristics.

To obtain a null position error, then the form of the considered weighting function is represented as:

$$W_1(s) = \frac{s+a}{k_1\,(s+b)} \qquad \text{for} \ \ (b < a \ \ \text{and} \ \ k \ge 1) \tag{4.15}$$

where the modulus margin, the precision, and the bandwidth are determined according to the parameters K_1, a, and b as:

- The bandwidth $w_c > \sqrt{\frac{a^2 - 2\,k_1^2\,b^2}{2k_1^2 - 1}}$.

- The gain margin $(\Delta_M > \frac{1}{k_1})$.

- The steady-state error as $\varepsilon_p < K_1 \frac{b}{a}$

Let $W_e(s)$ be a diagonal multi-variable weighting function:

$$W_e(s) = W_1(s)\,\mathbb{I}_{n_y}. \tag{4.16}$$

Two-block synthesis scheme

In order to force the gain of the controller to decrease beyond the bandwidth of the system (roll-off effect), then, reduce the amplification of the control and the influence of the measurement noise, it may be useful to add a weighting function $W_u(s)$ on the control signal $u(t)$. The weighting filter $W_u(s)$ is chosen so that the frequency template $\frac{1}{W_u(s)}$ on the transfer T_{ur} has a low-pass shape.

This weighting function $W_u(s)$ is generally a truncated derivative filter that amplifies the high frequencies. Then the considered weighting function is represented as:

$$W_2(s) = \frac{s}{k_2\,(cs+1)} \tag{4.17}$$

with $cw_c << 1$ and a lower k_2 value corresponds to roll-off effect in lower frequencies.

Let $W_u(s)$ be a diagonal multi-variable weighting function: $W_u(s) = W_2(s)\,\mathbb{I}_{n_u}$.

The two weighting transfer functions on the control signal $W_u(s)$ and on the output $W_y(s)$ are used to specify the performance requirements and are chosen so that the $\mathcal{H}_\infty$ norm of the closed-loop system condition

$$\|T_{zw}(K)\|_\infty = \left\| \begin{matrix} W_e S_y \\ W_u K S_y \end{matrix} \right\|_\infty \leq 1 \tag{4.18}$$

is fulfilled.

Four-block synthesis scheme

The four-block scheme include all the transfers $T_{er}(s)$, $T_{ur}(s)$ and $T_{ed}(s)$.

To enhance disturbance rejection the weighting function W_d is considered. A constant weighting function W_d leads to a frequency template with a high-pass shape that is sufficient to adjust the attenuation at low frequencies. A variable weighting function W_d leads to a frequency template with a pass-band shape to guarantee a good transient behavior in the face of an input disturbance.

The shape of the weighting function W_d can be modified to impose an attenuation of the frequency templates $\frac{1}{W_u(s)\,W_d}$ at high frequencies on the transfer $T_{ud}(s)$, to guarantee the robustness of the stability with respect to unmodeled high-frequency dynamics as in the works of Chellal (2016).

Let W_d be a diagonal multi-variable weighting function: $W_d = W_3(s)\,\mathbb{I}_{n_u}$.

4.4 Synthesis of the $\mathcal{H}_\infty$ controller

We aim to synthesize an $\mathcal{H}_\infty$ controller that controls the pose of the platform and the mean tension of the cables T_m. To perform this $\mathcal{H}_\infty$ synthesis we used the `hinfsyn` Matlab function with the Riccati optimization algorithm. A linearization of the ODE model must be performed first in order to synthesize the $\mathcal{H}_\infty$ controller.

The Figure (4.5) presents the LFT interconnection between the system $G(s)$ and the interconnection transfer matrix M. With this interconnection, we obtained the extended plant $P(s)$ by considering the performance and the control channels.
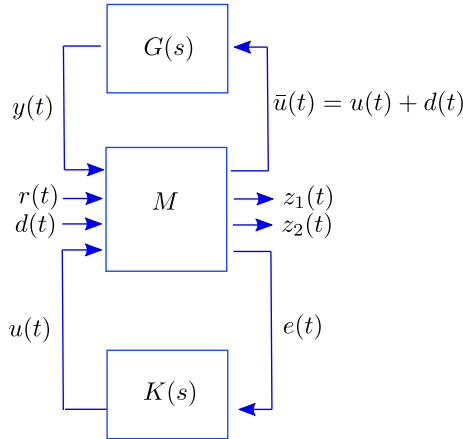

Figure 4.5: The interconnection for the $\mathcal{H}_\infty$ synthesis

The interconnection transfer matrix M can be expressed as:

$$\begin{bmatrix} \bar{u} \\ e \\ u \\ e \end{bmatrix} = \underbrace{\begin{pmatrix} \mathbb{O}_{nu \times ny} & \mathbb{O}_{nu \times ny} & +\mathbb{I}_{nu \times nu} & +\mathbb{I}_{nu \times nu} \\ -\mathbb{I}_{ny \times ny} & +\mathbb{I}_{ny \times ny} & \mathbb{O}_{ny \times nu} & \mathbb{O}_{ny \times nu} \\ \mathbb{O}_{nu \times ny} & \mathbb{O}_{nu \times ny} & \mathbb{O}_{nu \times nu} & +\mathbb{I}_{nu \times nu} \\ -\mathbb{I}_{ny \times ny} & +\mathbb{I}_{ny \times ny} & \mathbb{O}_{ny \times nu} & \mathbb{O}_{ny \times nu} \end{pmatrix}}_{M} \begin{bmatrix} y \\ r \\ d \\ u \end{bmatrix}. \tag{4.19}$$

4.5 Synthesis of an $\mathcal{H}_\infty$ controller for a three-flexible cable

We consider that we have a robot with only 3 flexible cables and with a mass-point (see Figure (4.6)). In this section we consider the ODE model presented in equation (3.39), where we consider that we have three cables and a mass-point instead of a platform, so the mass-point has only two degrees of freedom, the translation $(x - y)$. We aim to synthesize an $\mathcal{H}_\infty$ controller that control the position of the mass-point (x_p, y_p) and the mean tension of the three cables $T_m = \frac{1}{3}(T_1 + T_2 + T_3)$. The linearization of the ODE model has been performed using `Maple` along the center of the workspace $q_0 = \begin{bmatrix} 0 & 0 & 0 & 0 & 0 \end{bmatrix}^T$ for a null acceleration and velocity. The nominal model has been found controllable and observable.
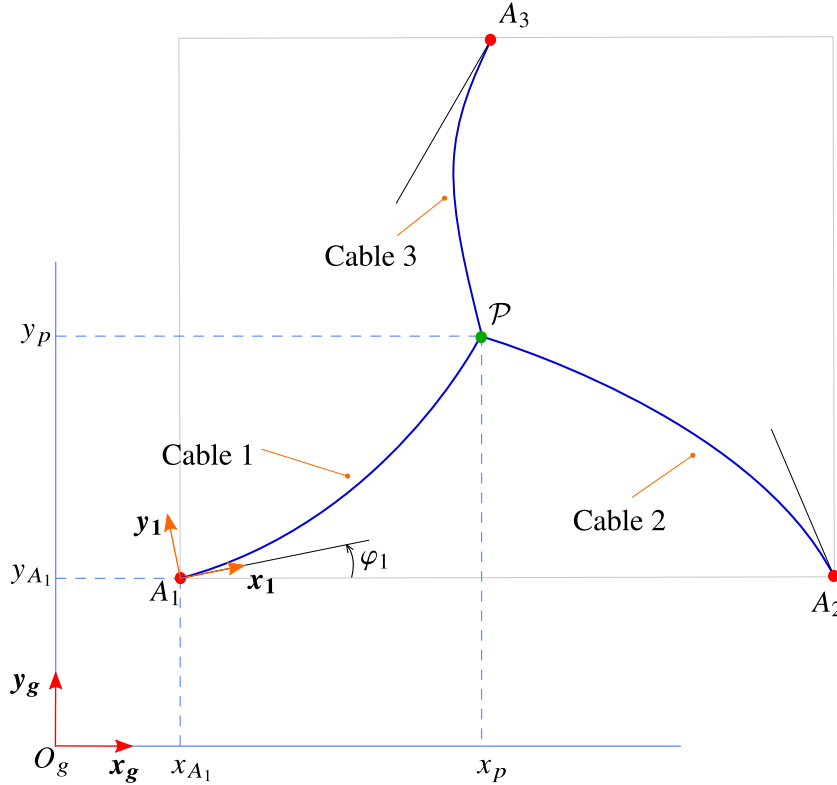

Figure 4.6: Schematic representation of a planar three flexible cable robot.

Three controlled outputs are considered: the two position coordinates and the mean value of the three tensions. Therefore, the obtained system can be separated into a position part and a tension part, $G(s) = \begin{bmatrix} G_p(s) \\ G_{Tm}(s) \end{bmatrix}$ with respectively 2 and 1

outputs. From the frequency responses in Figure (4.7), it appears that the position part behaves like a weakly-damped second-order system with resonance pulsations close to 3.5 rad/s whereas the tension part behaves like a gain. The next section presents the $\mathcal{H}_\infty$ controller design based on the obtained linear ODE model.
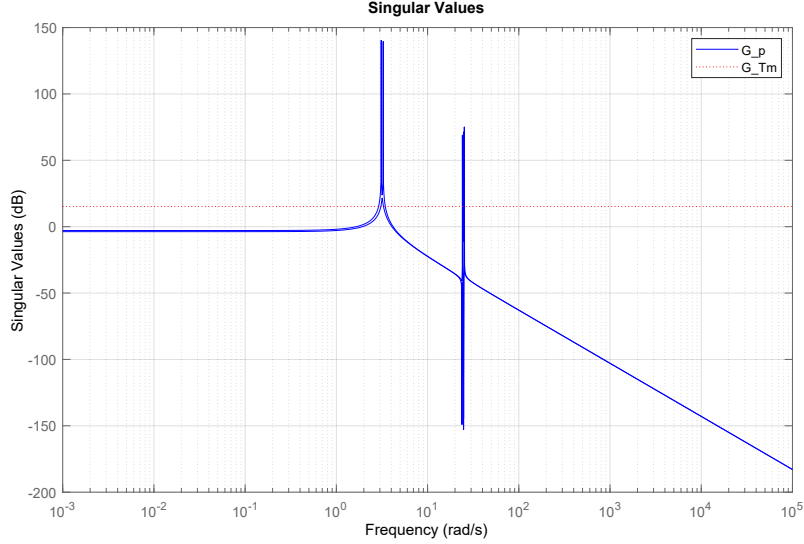
Figure 4.7: Frequency behavior of the open-loop nominal system

4.5.1 Two-block synthesis scheme

We choose a two-block synthesis scheme that considers only two weighting functions on the error and control signals. This scheme has been selected to meet the requirements of trajectory tracking and by relaxing the disturbance rejection constraints. The weighting function on the disturbance d has not been considered in the synthesis and is only used in the analysis step.

The considered weighting function $W_e(s)$ that manages the output sensitivity function $S_y(s)$ is shaped to satisfy the following specifications:

- a bandwidth of 3 rad/s.

- a modulus margin of 0.2 (maximal modulus of sensitivity function $\|S_y(s)\|_\infty \leq$ 2.50 dB).

- a negligible steady-state error.

Then, this weighting function has been chosen as:
$W_e(s) = \mathrm{diag}\left\{W_p(s), W_p(s), W_{Tm}(s)\right\}$ with $W_p(s) = W_{Tm}(s) = \dfrac{0.2\,s + 4.2}{s + 21 \cdot 10^{-5}}$. The weighting functions $W_p(s)$ and $W_{Tm}(s)$ can be taken as different from each other by choosing faster dynamics for the mean tensions or vice versa.

The weighting function $W_u(s)$ on the control signals is selected so as to ensure a slope of -80 dB/dec on the transfer from the reference to the control signal in order to decrease the gain of the controller for the frequencies higher than 10 rad/s. This roll-off effect decreases the measurement noise impact on the control signal

and improves the robustness with respect to unmodeled high-frequency dynamics. Then, this weighting function is given as:

$$W_u(s) = \text{diag} \left\{ W_{u1}(s), W_{u1}(s), W_{u1}(s) \right\} \text{ with } W_{u1} = (\frac{s + 10}{2\,s + 2000})^4.$$

The $\mathcal{H}_\infty$ obtained controller $K(s)$ can be separated into a position and a tension part as $K(s) = \begin{bmatrix} K_p(s) & K_{Tm}(s) \end{bmatrix}$. The synthesized $\mathcal{H}_\infty$ controller is of order 25 and its frequency response is depicted in Figure (4.8). This shows that the position part of the controller $K_p(s)$ provides a high gain in low frequency with some derivative effects from 3.25 rad/s to 182 rad/s and compensates the flexible modes at 25 rad/s. In addition, the controller gain nicely decreases in high frequency. The tension control part of the controller $K_{Tm}(s)$ behaves like a proportional-integral controller. The obtained $\mathcal{H}_\infty$ controller provides a closed-loop performance index $\gamma = 0.2668 < 1$.
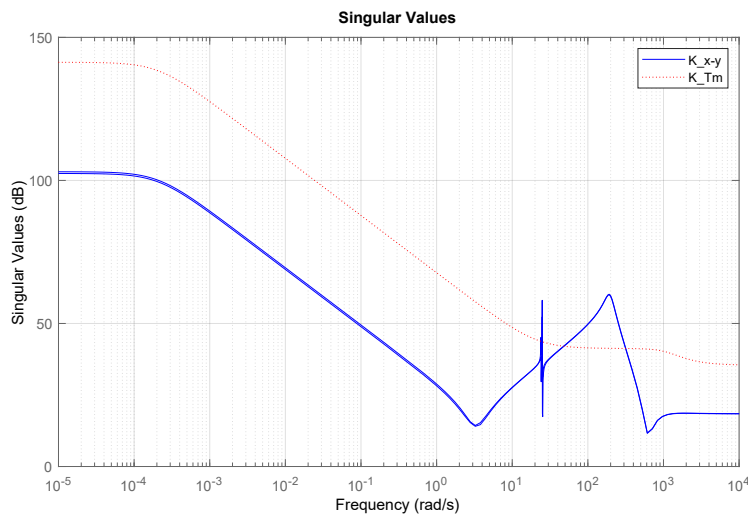
Figure 4.8: Frequency behavior of the controller

The Figure (4.9) presents the closed-loop transfers and their corresponding templates. The left-hand side of this figure shows that the templates on the sensitivity function $S_y(s)$ (upper-left) and on the transfer, $T_{ur}(s)$ are fully respected which means that the specifications are satisfied. On the right-upper plot $T_{ed}(s)$, we can check that the disturbance is well-rejected in low-frequency, with a slope of 20 dB/dec even if the disturbance input has not been included during the synthesis.

Using the balanced truncation method Laub et al. (1987) we can reduce the order of the controller to 17 (instead of 25 for the full order controller case) and with the expense of a performance index increasing from 0.2667 to 0.5678.

4.5.2 Simulation results

The obtained reduced-order $\mathcal{H}_\infty$ controller has been used to simulate the non-linear model in closed-loop for the set of parameters in Table (4.1). These parameters are considered first in the work by Ayala Cuevas et al. (2017). All the results of the simulation have been published by Saadaoui et al. (2021).

During the simulation, the mass-point is requested to follow a square of 1.5 m side with a speed of 0.5 m/s as a reference for the translation. The reference of
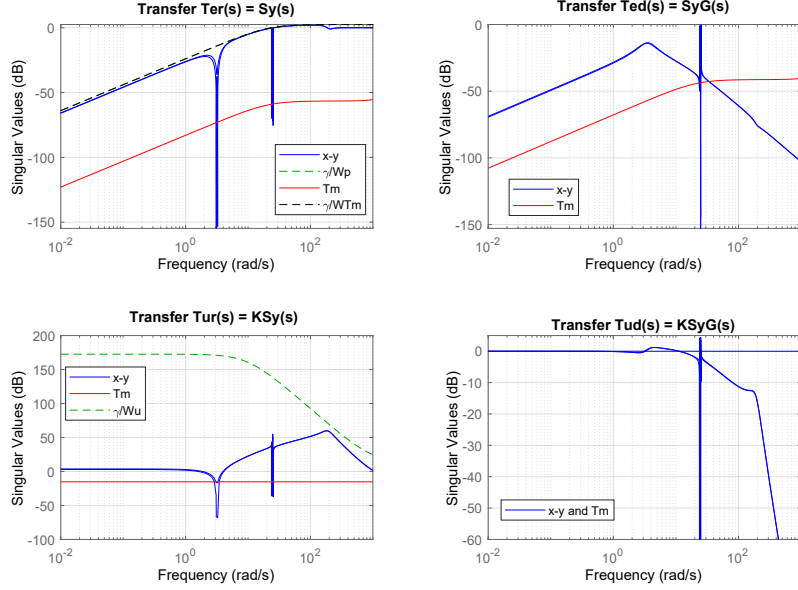
Figure 4.9: Closed-loop transfers (plain) and the corresponding templates (dashed)

| R	0.1 m	ρ	0.04 kg/m
J_0	$2.5 \cdot 10^{-3}$ kg·m^2	m_p	1 kg
l_t	5 m	D_1	$(-2.5\sqrt{2},\ 2.5)$ m
D_2	$(2.5\sqrt{2},\ 2.5)$ m	D_3	$(0,\ -5)$ m

Table 4.1: Numerical values of the three-flexible robot

mean tensions T_m^r is a step variation from 60 N to 70 N at $t = 10$ s to keep the cables always under tension. Starting from the center of the workspace, the mass-point runs through the square trajectory and then back to the workspace origin. White noise has been added to the measurement as well as a step disturbance of an amplitude 0.3 N·m has been also added to the three control signals at $t = 5$ s, $t = 10$ s, and $t = 15$ s respectively.

The obtained position trajectory tracking of the closed-loop system in the $x - y$ plane is illustrated in the Figure (4.10). Three points in time are captured in this figure, each displaying the geometry of the three cables. The displacement modes of the three cables are presented in Figure 4.11. The modes illustrate the flexibility to which the cables are subjected during the movement.

From the results in Figures (4.21) and (4.26), we notice that the trajectories of the mass-point (x_p, y_p) and the mean tension of the cables are well controlled with the obtained reduced-order $\mathcal{H}_\infty$ controller even in the presence of the disturbances and measurement noise. A high-precision of the (x_p, y_p) trajectory tracking is shown by the small error. Moreover, the tensions of the three cables remain positive.

Notice that the control signals (the winder torques) are proportional to the tensions with the relation $u_i = T_i \cdot R$. Even if the flexibilities of the cables are hardly visible on the cable shapes (Figure 4.10), the corresponding modes must be properly controlled in order to avoid instability in the mass-point positioning.
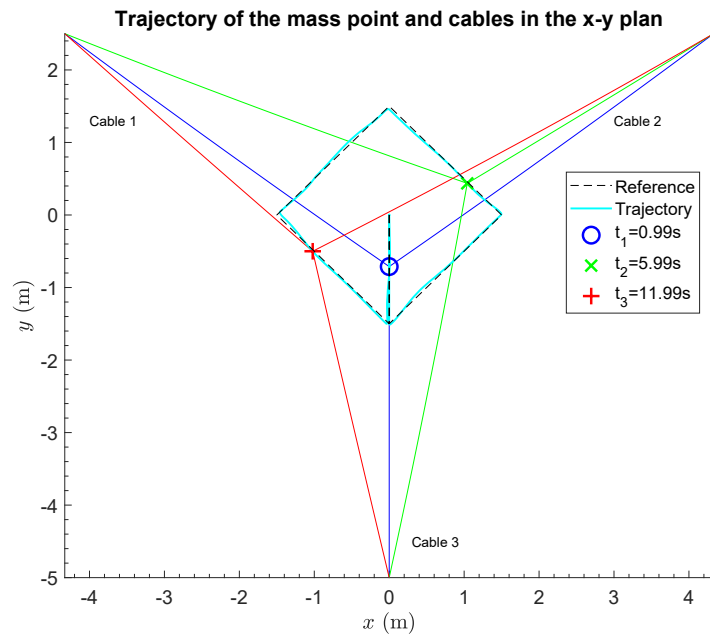
Figure 4.10: Trajectory of the mass point and cables in the $x - y$ plan
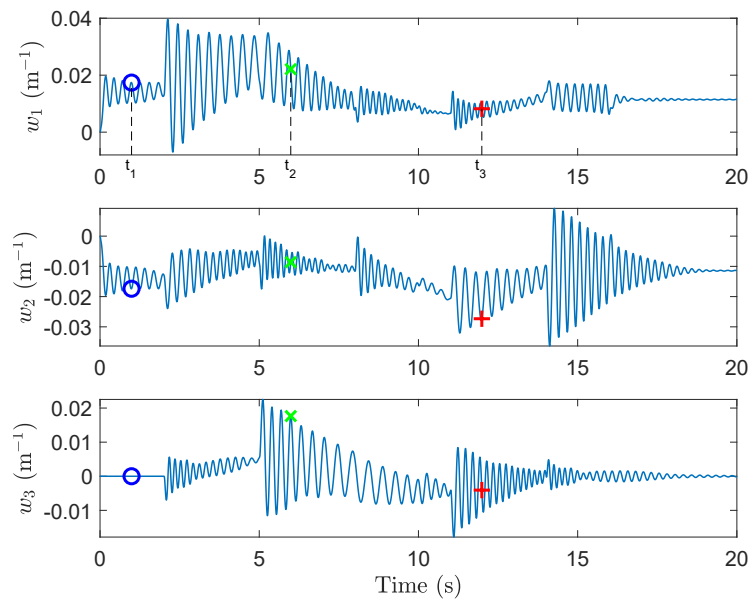

Figure 4.11: Modal coordinates for the displacements of the cables

81
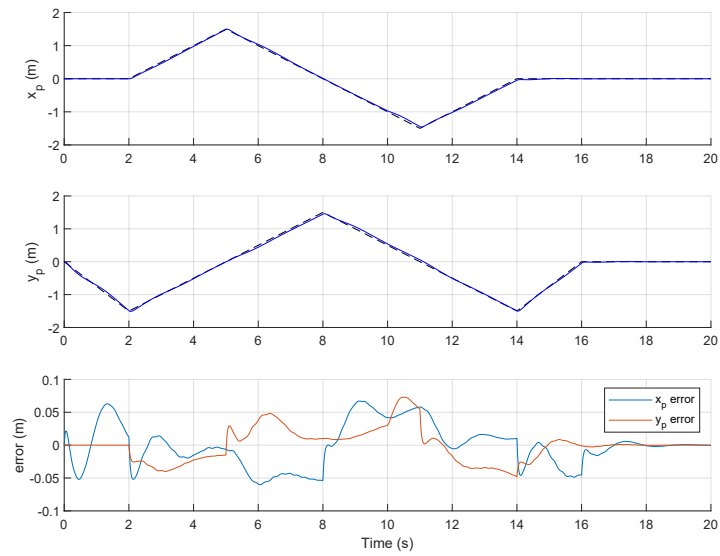
Figure 4.12: x_p and y_p trajectories tracking and error with $\mathcal{H}_\infty$ control
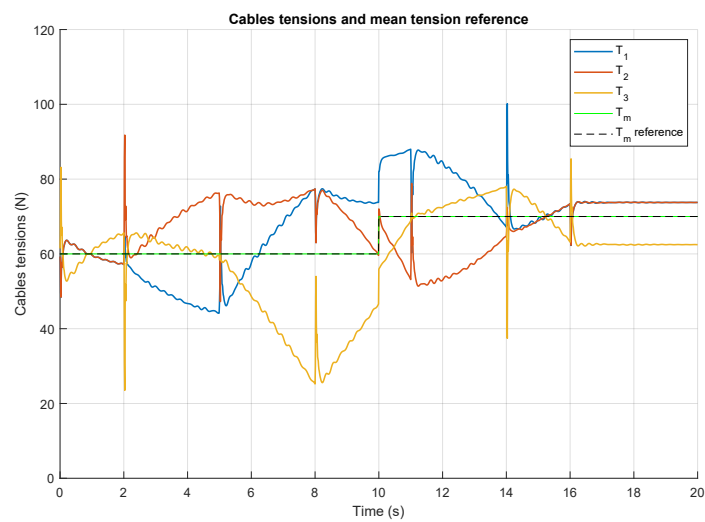

Figure 4.13: Cables tensions and mean tension reference
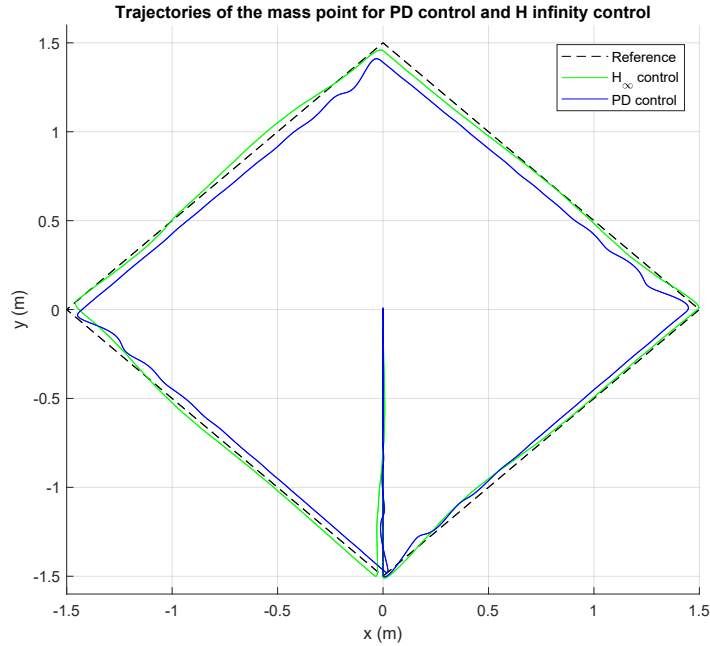
Figure 4.14: Trajectories of the mass point for PD control and $\mathcal{H}_\infty$ control

For comparison, we considered a PD control that has been taken from the literature (Ayala Cuevas et al. (2017)). The PD controller manages the position of the mass point, with the proportional gain $C_p = 400$ N, a derivative gain $C_d = 10$ N.s, and a filtering frequency $\omega_f = 100$ rad/s. In Figure (4.14), a comparison of the trajectory tracking has been shown for the non-linear model controller with the two controllers. The non-linear model controlled with the reduced-order $\mathcal{H}_\infty$ controller shows better trajectory tracking than the non-linear model controlled with the PD controller where some oscillations and an offset are noticed.

4.6 Synthesis of an $\mathcal{H}_\infty$ controller for a four-flexible cable

We consider that we have a robot with four-flexible cables and with a platform (the ODE model presented in the equation (3.39)). We aim to synthesize an $\mathcal{H}_\infty$ controller that controls the position and orientation of the platform (x_p, y_p, α) and the mean tension of the four cables $T_m = \frac{1}{4}(T_1 + T_2 + T_3 + T_4)$. The linearization of the ODE model has been performed using also `Maple` along the center of the workspace $q_0 = \begin{bmatrix} 0 & 0 & 0 & 0 & 0 & 0 & 0 & 0 \end{bmatrix}^T$. The nominal model has been found controllable and observable.

Four outputs will be controlled: the position (x_p, y_p) and orientation α of the platform and also the mean tension of the four cables $T_m = \frac{1}{4}(T_1 + T_2 + T_3 + T_4)$. According to this partitioning of the output vector, the open-loop system $G(s)$ is decomposed into three parts and each part is evaluated separately $G(s) = \begin{bmatrix} G_{x-y}(s) & G_\alpha(s) & G_{Tm}(s) \end{bmatrix}^T$. The frequency response of the open-loop nominal system is presented in Figure (4.15). The position part behaves like a weakly-damped second-order with a triple resonance around the frequencies 5.23 rad/s, 6.1 rad/s,

and 77.2 rad/s. The orientation part behaves as a weakly-damped second-order with multiple resonances around the frequencies 6.1 rad/s and 77.2 rad/s. The tension part behaves like a pure gain.
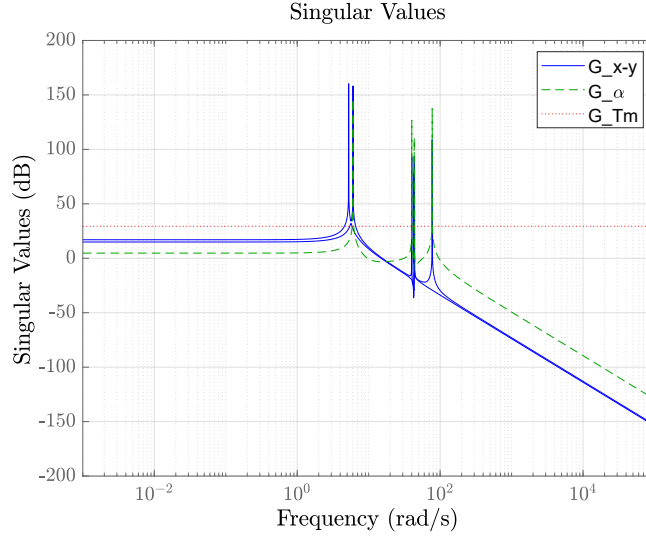
Figure 4.15: Open-loop frequency response of the linear system

4.6.1 Two-block synthesis scheme

We first start with a two-block synthesis scheme that favors the constraints of trajectory tracking, and where the disturbance d is considered only for analysis, in order to explain its limitations and justify why a four-bloc scheme is required.

The weighting function $W_e(s)$ on the output sensitivity function $S_y(s) = T_{er}(s)$ has been tuned to satisfy the following specifications:

- a bandwidth of 7 rad/s for the translation and 2 rad/s for the orientation.

- a modulus margin of 0.5 for the translation and 0.9 for the orientation.

- a negligible steady-state error.

The weighting function on the error signals has been given as: $W_x = W_y = W_{Tm} = \dfrac{0.5\,s + 9.26}{s + 4.63 \cdot 10^{-5}}$, and $W_\alpha(s) = \dfrac{0.9\,s + 2.182}{s + 1.091 \cdot 10^{-5}}$, where $W_e(s) = \text{diag}\left\{W_x(s), W_y(s), W_\alpha(s), W_{Tm}(s)\right\}$. The tension part of the linear system is a pure gain, which means that the adjustment of the transfer dynamics is simple.

From now on, we consider the weighting function on the mean tension to be identical to that on the position. The weighting function $W_u(s)$ on the control signals is selected to guarantee a slope of -60 dB/dec at high frequencies. This would decrease the effect of measurement noise on the control signal for frequencies higher than 10 rad/s. This roll-off effect improves the robustness with respect to unmodelled dynamics. The weighting function has the following shape: $W_u(s) = W_{u1}(s)\,\mathbb{I}_4$ with $W_{u1} = (\dfrac{s + 10}{2\,s + 2 \cdot 10^5})^3$.
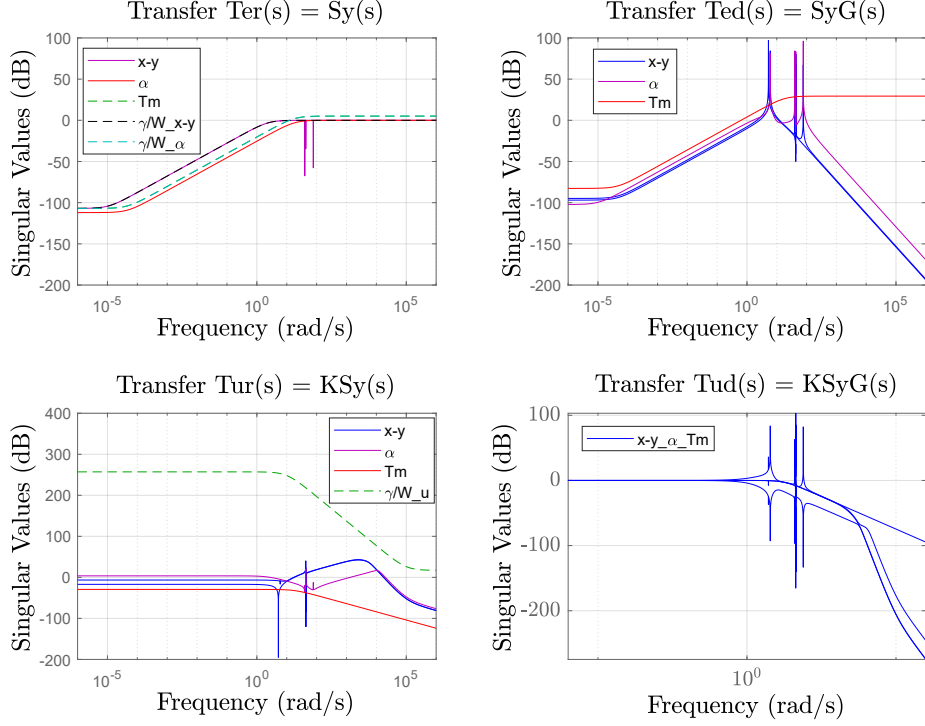
Figure 4.16: Closed-loop transfers (plain) and the corresponding templates (dashed) with two-block synthesis scheme

From the closed-loop frequency response in Figure (4.16) we can detect some lowly-damped resonances at medium frequencies in transfer $T_{ed}(s)$. During the simulation, in the time trajectory tracking of the orientation (see Figure (4.17)), an oscillation of a period 0.13 s was noticed, which corresponds exactly to the resonance at the frequency 48.33 rad/s in the transfer $T_{ed}(s)$.

4.6.2 Four-block synthesis scheme − setting #1

For damping the resonances in the transfer $T_{ed}(s)$, we opt for the four-block synthesis scheme that promotes not only the trajectory tracking but also the disturbance rejection. Notice that the tuning methodology is similar to the one considered by Chellal (2016). For this synthesis, a high-pass filter template $\frac{\gamma}{W_{e1}(s) \times W_{d1}(s)}$ is chosen on the transfer $T_{ed}(s)$ in order to satisfy a good disturbance rejection at low frequencies and well damping of resonances at medium frequencies. Notice that, thanks to the disturbance rejection properties (see $T_{ed}(s)$), attenuation in low frequency on $T_{er}(s)$ is ensured, even if the corresponding weighting function is chosen as constant. This constant weighting function leads to the obtaining of a reduce-order of the weighted system and thus the order of the obtained controller.

The weighting functions $W_r(s) = W_{r1}(s)\,\mathbb{I}_4$ and $W_e(s) = W_{e1}(s)\,\mathbb{I}_4$ were selected as: $W_{r1}(s) = 1$ and $W_{e1}(s) = 0.5$. The weighting function on disturbances $W_d(s) = W_{d1}(s)\,\mathbb{I}_4$ was selected with the following shape: $W_{d1} = 5\,\dfrac{s + 10}{2\,s + 10^{-5}}$.

The performances of the trajectory tracking that are evaluated from the closed-loop frequency response (see Figure 4.18) are expressed as follows:
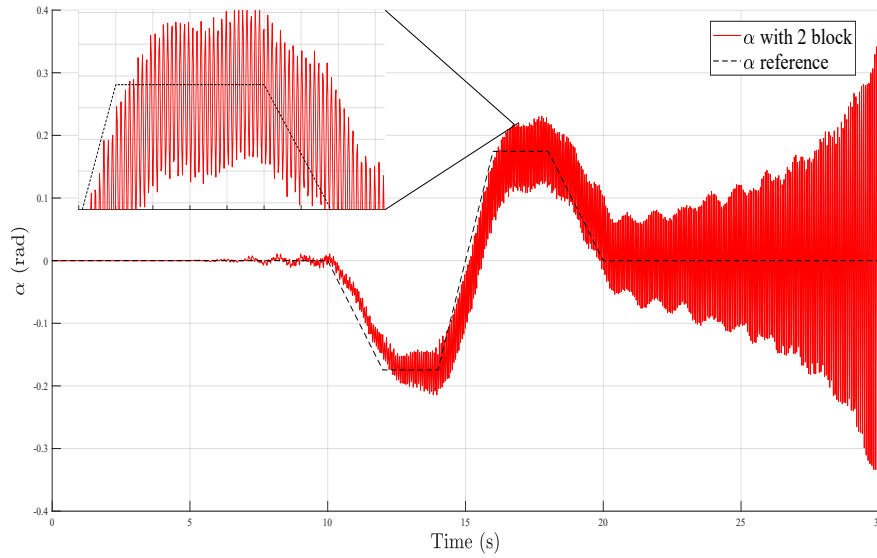
Figure 4.17: Orientation trajectories with two-block synthesis scheme
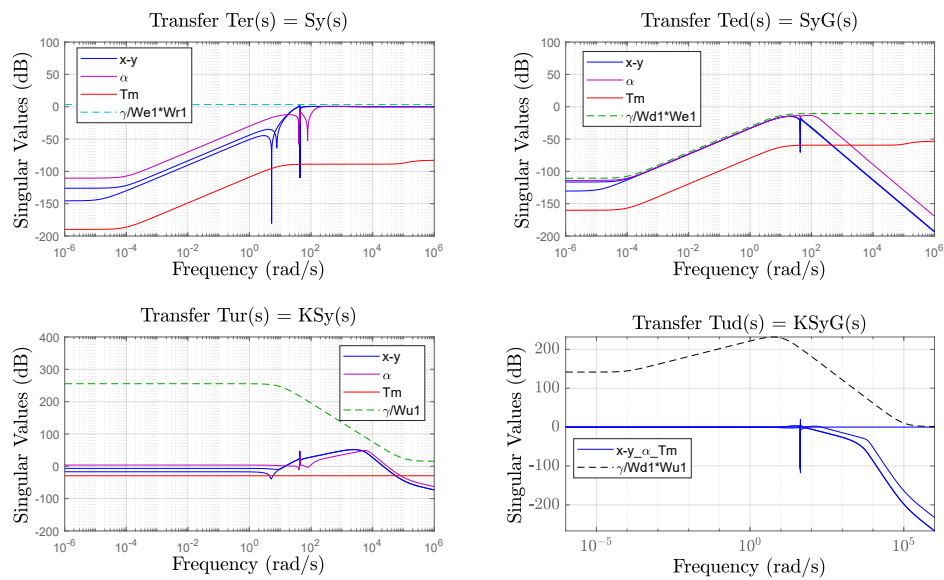
Figure 4.18: Closed-loop transfers (plain) and the corresponding templates (dashed) with four-block synthesis with setting #1

- a bandwidth of 41 rad/s for the position and 42 rad/s for the orientation.

- a modulus margin of 0.69 for the translation and 0.91 for the orientation.

- a negligible steady-state error.

86

4.6.3 Four-block synthesis scheme with modulation of dynamics – setting #2

We now propose another setting for a four-block synthesis scheme that ensures different bandwidths on the different channels, while suiting the physical nature of the system. In the previous study by Chellal (2016), where the cable-driven robot was controlled in the operational space, modulation of the performance was possible by using any weighting. In the current case, the control signal is in the joint space and there would be no sense in modifying the specifications on $W_d(s)$ or $W_u(s)$ since all the actuators are the same. Therefore, the performance modulation must be ensured by tuning $W_r(s)$ and $W_e(s)$ at the measurement side of the process.

Therefore, the weighting functions are chosen as
$W_{e2}(s) = \text{diag}\left\{W_{e2p}(s), W_{e2p}(s), W_{e2\alpha}(s), W_{e2T}(s)\right\}$ and
$W_{r2}(s) = \text{diag}\left\{W_{r2p}(s), W_{r2p}(s), W_{r2\alpha}(s), W_{r2T}(s)\right\}$. Different rejection properties are first ensured on the channels $T_{ejd}(s)$ of $T_{ed}(s)$, where j stands for p, α or Tm, by adjusting the weighting $W_{e2j}(s)$. Then, a uniform modulus margin on the four channels is ensured by choosing $W_{r2j}(s) = \frac{\Delta M}{W_{e2j}(s)}$, resulting in a template of the form $\frac{\gamma}{W_{r2j}(s) \times W_{e2j}(s)} = \frac{\gamma}{\Delta M}$ on $T_{er}(s)$.

In this presented synthesis, the weighting function $W_{d1}(s)$ and the modulus margin $\Delta M = 0.5$ are identical to those in setting #1. The weighting functions on the error signals are adjusted as: $W_{e2p}(s) = W_{e2T}(s) = 0.6$ and $W_{e2\alpha}(s) = 4.5$ while those on the references are adjusted as: $W_{r2p}(s) = W_{r2T}(s) = \Delta M$ and $W_{r2\alpha}(s) = \frac{\Delta M}{4.5}$.

Note that the weighting function of the control signals $W_u(s)$ for the synthesis #1 and #2 are the same considered for the case of a two-block synthesis scheme.
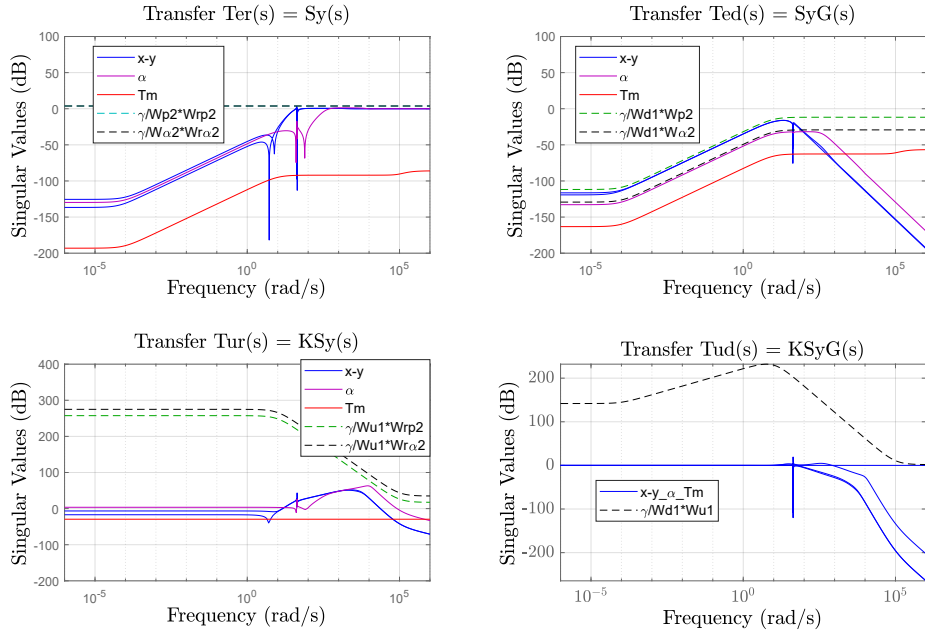

Figure 4.19: Closed-loop transfers (plain) and the corresponding templates (dashed) with four-block synthesis with setting #2

The performances of the trajectory tracking are evaluated from the closed-loop frequency response (see Figure 4.19) are expressed as follows:

- a bandwidth of 42 rad/s for the translation and 865.46 rad/s for the orientation.

- a modulus margin of 0.68 for the translation and 0.86 for the orientation.

- a negligible steady-state error.

4.6.4 Controller synthesized
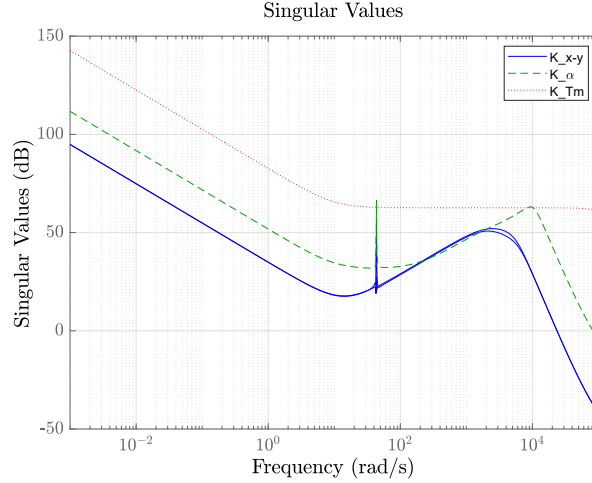
Figure 4.20: Frequency response of the controller

The frequency response of the controller $K(s) = \begin{bmatrix} K_{x-y}(s) & K_\alpha(s) & K_{Tm}(s) \end{bmatrix}$ that is obtained by the chosen second tuning #2 is illustrated in the Figure (4.20). From this response, we can notice that the position $K_{x-y}(s)$ and the orientation $K_\alpha(s)$ parts of the controller provide a high gain at low frequencies with a derivative behavior ranging from 9.85 rad/s to $1.07 \cdot 10^4$ rad/s along with a compensation of the flexible modes close to 43.3 rad/s. The controller gain decreases perfectly at high frequencies. The tension part $K_{Tm}(s)$ of the controller behaves like a proportional-integral controller. The obtained controller is of order 30 and with satisfying closed-loop performance criteria $\gamma = 0.7729 < 1$.

4.6.5 Simulation results

The ODE non-linear model with four-flexible cables attached to a rotational platform has been simulated in closed-loop with the obtained $\mathcal{H}_\infty$ controller synthesized with the four-block synthesis scheme. Based on the identification performed by Chellal (2016), the numerical parameters have been updated to match the real parameters of the INCA 6D prototype in order to perform in a second time the experimental tests with the obtained $\mathcal{H}_\infty$ controller. The parameters are provided in Table (4.3). All the results of the simulation have been published by (Saadaoui et al. (2022b); Saadaoui et al. (2022a)).

The simulations have been performed by considering a reference signal such that the platform translates according to a square trajectory of 0.4 m per side with a constant speed of 0.2 m/s, while performing an orientation of -10° at $t = 10$ s and

R	0.017 m	ρ	0.02 kg/m
J_0	$2.911 \cdot 10^{-5}$ kg·m^2	m_p	0.036 kg
l_t	3.85 m	Je	$23.52 \cdot 10^{-5}$ kg·m^2
D_1	$(-1.255, -1.395)$ m	D_2	$(1.255, -1.395)$ m
D_3	$(1.255, 1.395)$ m	D_4	$(-1.255, 1.395)$ m
B_1	$(-0.07, 0)$ m	B_2	$(-0.07, 0)$ m
B_3	$(0.07, 0.07)$ m	B_4	$(-0.07, 0.07)$ m

Table 4.2: Numerical values of the four-flexible robot

of $+10^o$ at $t = 14$ s, then returning to 0° at the end of the simulation. The mean tensions trajectory was imposed to follow a variation from 11 N to 12 N at $t = 14$ s. The platform starts from the center of the workspace and returns to the center at the end of the simulation. During the simulation, step disturbances are added to the control signals, with an amplitude of 0.2 N·m at $t = 5$ s, $t = 10$ s, $t = 15$ s, and $t = 20$ s.
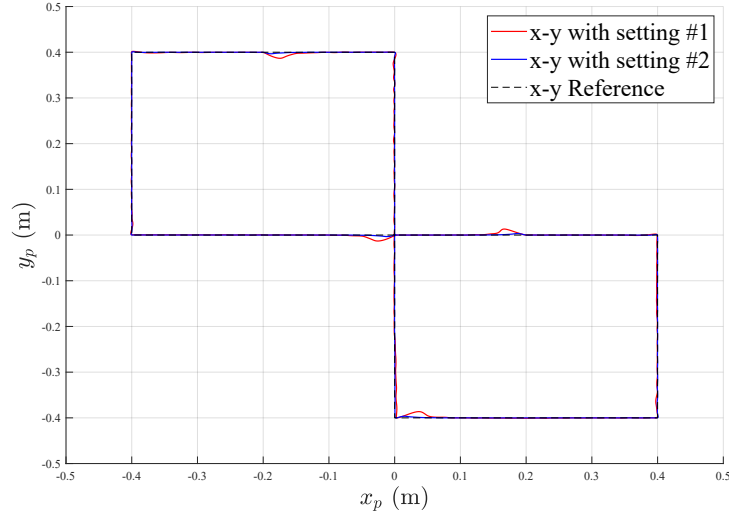
Figure 4.21: Translation trajectories of the platform for $\mathcal{H}_\infty$ control with our two four-bloc synthesis

Figures (4.21), (4.22), and (4.23) represent the trajectories of the position and orientation of the platform for the two four-block synthesis controllers. The trajectories are well tracked and the disturbance rejection is improved with the second synthesis (setting #2) specially for the case of the orientation trajectory. The root means square (RMS) of the trajectories tracking errors are given in Table (4.3). The RMS values of the position (x_p, y_p) and orientation (α) obtained in the second synthesis are smaller than those obtained with the first synthesis, which signifies a higher precision and a better disturbance rejection.

The position and orientation trajectories of the closed-loop system and the geometry of the four cables captured at three different times are shown in Figure (4.24). The three instants are chosen to show the platform in different orientations (0°, -10°, 10°). The flexibility coordinates of the four cables are depicted in Figure (4.25). The
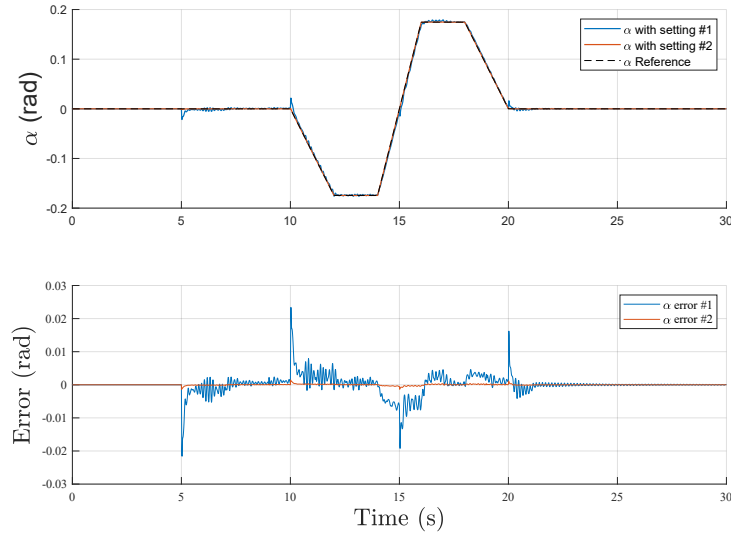
Figure 4.22: Orientation trajectory of the platform for $\mathcal{H}_\infty$ control with our two four-bloc synthesis
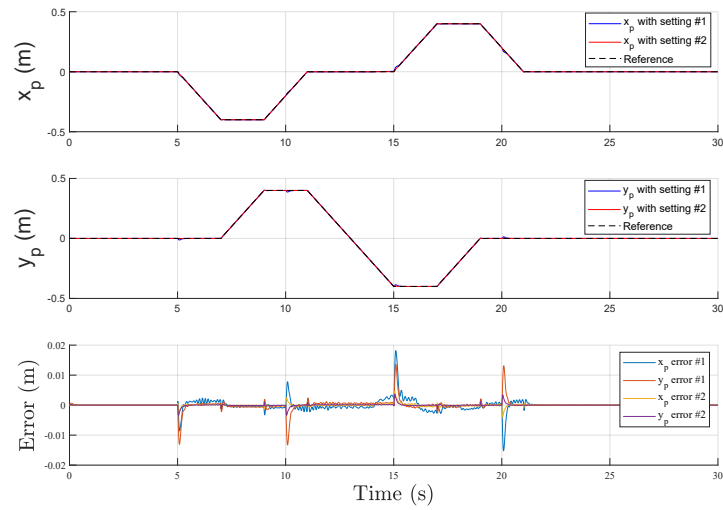
Figure 4.23: x_p and y_p trajectories tracking and error with $\mathcal{H}_\infty$ control with with our two four-bloc synthesis

flexibility modes are of an amplitude between 0.01 and 0.02 and they fade out at the end of the simulation.

The trajectories of the mean tensions and the four cable tensions are shown in Figure 4.26. In the results, we can observe that the mean tension is well controlled and all cable tensions remain positive.

	RMS with disturbance	RMS without disturbance
x_p with setting #1	1.8 mm	0.896 mm
x_p with setting #2	0.39 mm (-78 %)	0.18 mm (-79 %)
y_p with setting #1	1.6 mm	0.39 mm
y_p with setting #2	0.36 mm (-77 %)	0.1 mm (-74 %)
α with setting #1	2.8 mrad	1.8 mrad
α with setting #2	0.16 mrad (-94 %)	0.1 mrad (-94 %)

Table 4.3: RMS of the trajectories tracking error (x_p, y_p, α) with and without disturbance and the reduction from setting #1 to #2
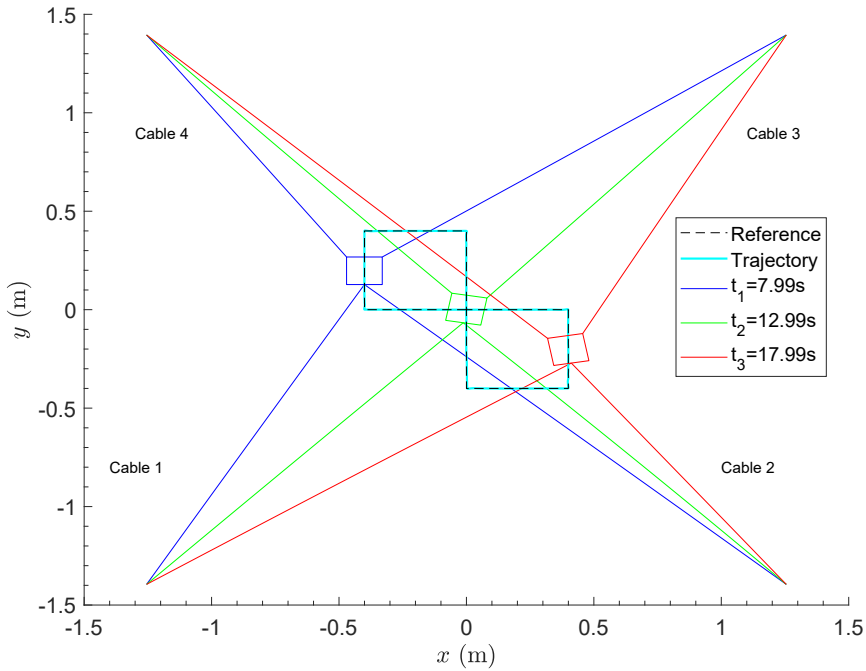
Figure 4.24: Trajectories of the platform and cables in the $x-y$ plan with the second synthesis

4.7 Conclusion

The purpose of this chapter is to present the $\mathcal{H}_\infty$ dynamic control of the position and orientation of the planar parallel flexible cable robots with two and three degrees of freedom. The theoretical aspects and a detailed discussion for the standard $\mathcal{H}_\infty$ synthesis problem was presented to properly introduced the method.

To perform the $\mathcal{H}_\infty$ synthesis, two different synthesis block schemes were proposed, promoting the properties of trajectory tracking and the rejection of disturbances. Based on the closed-loop frequency response and the simulation results, the simplest synthesis approach with a two-block scheme was found to be limited compared with the four-block synthesis scheme that better privileged the disturbance rejection.
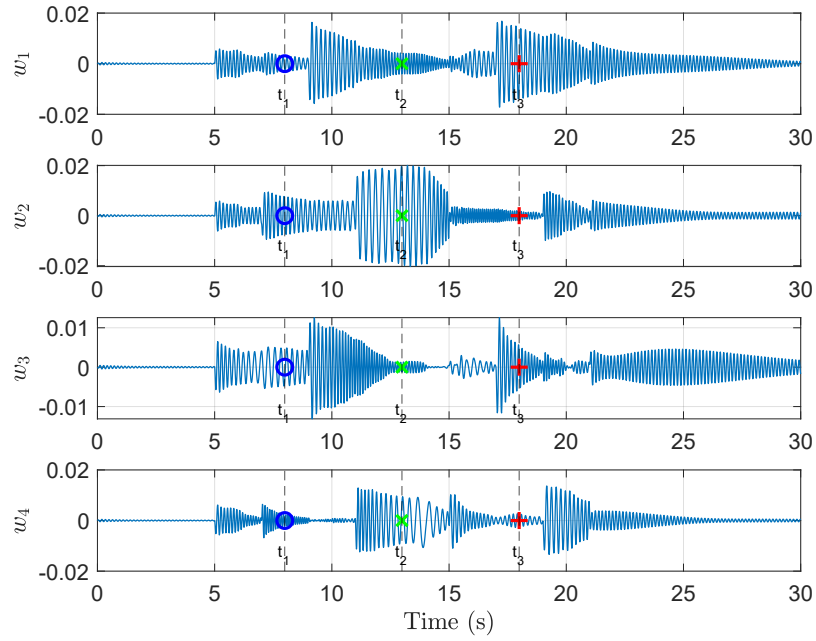
Figure 4.25: Modal coordinates for the flexibility of the cables with the second synthesis
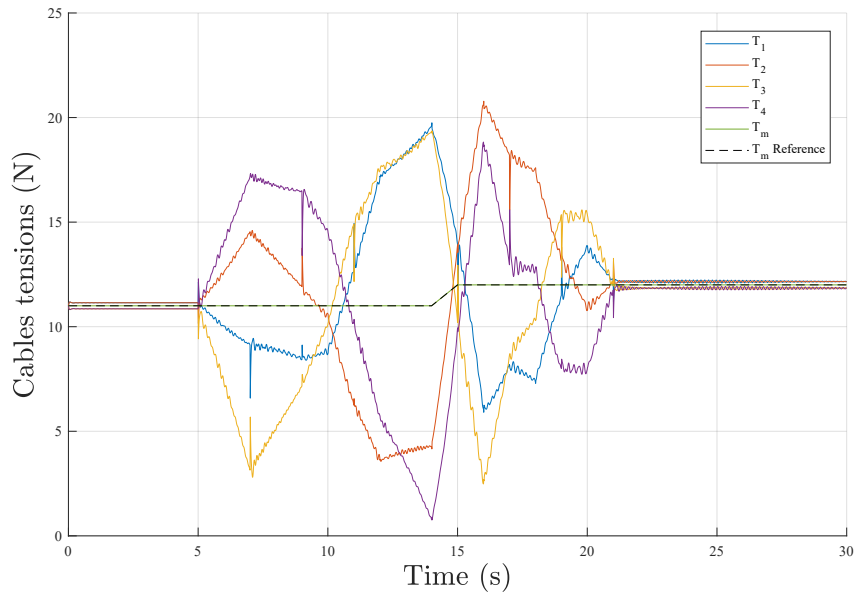
Figure 4.26: Cables tensions and mean tension reference with the second synthesis

The investigations on the simulation results of the non-linear model controlled with the synthesized controller were presented in detail. The results obtained by considering the $\mathcal{H}_\infty$ controller reveals an outstanding performance in terms of rapidity, precision, and stability on the trajectory tracking and also a good disturbances rejection. The condition of the positivity of the cable tension was also satisfied.

Conclusion et perspectives

Conclusion

With a wide range of potential applications in various fields, cable robots can be a promising and rapidly developing technology. Among its applications fields, let us mention construction, medical rehabilitation, entertainment, space exploration, etc. As well as their low cost of construction and maintenance, high payload capability, and the ability to move rapidly in a large work-space, they can accomplish tasks that conventional robots cannot. However, cable robots also present challenging issues such as the unilateral actuation and the flexibility of the cables. These challenges are likely addressed in ongoing research, making the CDPRs more capable and applicable.

Dynamic modeling of CDPRs leads to models with geometric constraints. The drawback of this class of models is the variable's dependency which makes it not suitable for the control synthesis. In addition, the phenomenon of the flexibility of cables disrupts the positioning of the robot's platform by causing delay and inaccuracy. The scientific contribution of the thesis is therefore to solve these problems by applying an $\mathcal{H}_\infty$ control synthesis to maintain the robot cables under tension and to track the platform trajectory with accuracy while damping the cables vibrations. The control synthesis has been applied for an ODE model with four flexible cable and 3-DOF to avoid the variable's dependency in the case of the DAE model. Notice that, in our approach, we do not use additional sensors to estimate the displacements of the cables and improve the observability of the model, contrarily to Dallej et al. (2019). The approach that we presents can be implemented on a standard process without additional cost.

In order to achieve this contribution, the dynamic model of planar cable-driven parallel robots, with four cables and 3-DOF, has been developed considering its geometry, its kinematics, and its dynamics. This model also incorporates the pre-tensioning system specific to the INCA 6D prototype available in our laboratory, that modifies the stiffness of the mechanism. This model was obtained using the Lagrange formalism. At first, the cables were considered as rigid-links and were modeled based on this principle. The simplified obtained model was used to design the classic PID controller and also to study the reachability of the workspace.

Then, a model based on the assumption of cable flexibility was subsequently developed and the cables were considered to be inextensible, without torsion, and deformed by generating transverse vibrations. These vibrations or flexibilities have been modeled using the assumed modes approach by considering a polynomial shape of deformation with one single mode. This dynamic model obtained also by using the Lagrange formalism exhibits geometric constraints (differential-algebraic equation model). The resulting dynamics of this multi-variable system are non-linear.

This differential-algebraic equation model has been linearized by following two approaches: a direct one and an indirect one (descriptor system form), to be used afterwards for the $\mathcal{H}_\infty$ synthesis that is well suited to multivariate systems with flexibility. Obtained a controllable and observable linear DAE model was not possible, then a transformation to an ordinary differential equation model was carried out to avoid this problem.

The geometric model has been validated experimentally, considering the INCA 6D prototype. During the experimental test, the measurement of the platform pose was accomplished by a motion capture system. A video of cable movement was taken during robot operation and the 3D positions of the cable points have been calculated from the video and compared to the geometric model using the least squares approach. The results show that the proposed flexible cable geometric model represents well the real behavior of cable.

After obtaining the nominal linear controllable and observable ODE dynamic model, we proceeded to the $\mathcal{H}_\infty$ synthesis. This synthesis has been established in the operational space for controlling the positioning of the robot platform while taking into account the cables' flexibility. The $\mathcal{H}_\infty$ controller is synthesized to manage the cable tensions and to ensure the control performance of the platform pose. This controller provides the necessary forces to be exerted on the platform, maintaining a good tracking trajectory and rejecting disturbances.

The approach was first developed in the context of a three-cable with 2DOFs robot based on the model proposed by Ayala Cuevas et al. (2017) and then in the case of the four-cable with 3DOFs presented in this thesis. In the case of the first model, the synthesis was obtained considering a two-block synthesis scheme. The weighting functions have been adjusted to meet the requirements and the results show a good trajectory tracking of the mass-point. Then, an $\mathcal{H}_\infty$ controller has been proposed in the case of a flexible four-cable model with a platform of 3-DOF (translation and orientation). A two-block scheme was unable to achieve satisfactory performance and meet disturbance rejection requirements, so a four-block scheme was proposed. To distinguish between translation and orientation dynamics of the platform pose, this scheme was proposed in two versions. Using the obtained $\mathcal{H}_\infty$ controller, the nonlinear model was able to track the trajectory and reject disturbances very effectively.

Perspectives

The results of this thesis contribute to the control of flexible cable-parallel robots and suggest several future studies. Some of these perspectives extend the accomplished work that we did not have enough time to achieve as follows:

- **Control strategy experimental test on planar CDPR**

  The validation of the synthesized obtained controller has been accomplished only on simulation and only the geometric model that has been validated considering a video taken during the cable movement. An experimental test of this controller on the INCA prototype should be performed. Prior to these tests on the planar INCA robot, future studies should identify and validate the dynamic model with flexible cables considering the video.

- **Robustness analysis**

  The $\mathcal{H}_\infty$ synthesis is performed from the linearized nominal model that has been obtained by linearization of the system dynamics around the nominal pose (center of the workspace). Only the simulation for a specified trajectory has been considered to validate the non-linear closed-loop performance of the control system. In order to verify its performance and stability across the entire workspace, a robustness analysis based on the existing theorems should be performed.

- **Control of CDPRs**

  Certainly, the $\mathcal{H}_\infty$ control is very suitable for multi-variable systems with flexibility but this control synthesis is limited to the surroundings of the chosen operating point (center of the workspace in the case of this thesis). Comparing this synthesis with a non-linear control strategy that take the non-linearity of the model during the synthesis would be beneficial.

Other perspectives reformulate a new research problem can be expressed as follows:

- **Modeling and synthesis of 3D CDPRs model**

  Due to the mathematical complexity of the model which takes into account the flexibility and the numerical problems of calculation that we encountered during its modeling, we have not been able to generate a dynamic 3D model with 6DOFs of CDPR by modeling the flexibility using assumed modes. Therefore, we have only proposed a 2D model with 3DOFs. By considering only four cables, we made the INCA prototype into a planar structure in order to perform the experimental tests. While testing the INCA prototype during the experiments, we encountered many problems due to the fact that it is essentially designed as a robot with eight cables and 6DOFs, not a planar robot. Future work can propose a 3D model of a cable-driven parallel robot with flexibility modeled using the assumed modes approach to better perform experimental tests on the INCA prototype. More investigations can also be carried out on the study to perform the DAE synthesis.

Bibliography

Project ANR CoGiRo. http://www.lirmm.fr/cogiro/. [Online].

M. Agahi and L. Notash. Redundancy resolution of wire-actuated parallel manipulators. *Transactions of the Canadian Society for Mechanical Engineering*, page 561–575, 2009.

R. A. Ahouee, S. Z. Moussavi, and J. Hamedi. Neuro-fuzzy intelligent control algorithm for cable-driven robots with elastic cables. In *International Symposium on Computer Science and Intelligent Controls (ISCSIC)*, pages 57–62, 2017. doi: 10.1109/ISCSIC.2017.25.

J. Albus, R. Bostelman, and N. Dagalakis. The NIST ROBOCRANE. (10, No. 5), 1992-09-08 00:09:00 1992. URL https://tsapps.nist.gov/publication/get_pdf.cfm?pub_id=820409.

A.B. Alp and S.K. Agrawal. Cable suspended robots: design, planning and control. In *Proceedings 2002 IEEE International Conference on Robotics and Automation (Cat. No.02CH37292)*, volume 4, pages 4275–4280 vol.4, 2002. doi: 10.1109/ROBOT.2002.1014428.

P. Apkarian and D. Noll. Nonsmooth $\mathcal{H}_\infty$ synthesis. *IEEE Transactions on Automatic Control*, page 71–86, 2006.

M. M. Aref, P. Gholami, and H. D. Taghirad. Dynamic and sensitivity analysis of kntu cdrpm: A cable driven redundant parallel manipulator. *2008 IEEE/ASME International Conference on Mechtronic and Embedded Systems and Applications*, pages 528–533, 2008.

C. Armanini, F. Boyer, A. Mathew, C. Duriez, and F. Renda. Soft robots modeling: A structured overview. *IEEE Transactions on Robotics*, PP:1–21, 06 2023. doi: 10.1109/TRO.2022.3231360.

M. Arsenault. *Stiffness Analysis of a Planar 2-DoF Cable-Suspended Mechanism While Considering Cable Mass*, pages 405–421. 01 2013. ISBN 978-3-642-31987-7. doi: 10.1007/978-3-642-31988-4_25.

J. Ayala Cuevas, E. Laroche, and O. Piccin. Assumed-mode-based dynamic model for cable robots with non-straight cables. In *Third International Conference on Cable-Driven Parallel Robots*, volume 53 of *Mechan. Machine Science*. Springer, Aug 2017. doi: 10.1007/978-3-319-61431-1_2. URL http://icube-publis.unistra.fr/4-ALP17.

K. Azizian and P. Cardou. The dimensional synthesis of planar parallel cable-driven mechanisms through convex relaxations. *Journal of Mechanisms and Robotics*, 4: 031011, 08 2012. doi: 10.1115/1.4006952.

R. Babaghasabha, M. Khosravi, and H. Taghirad. *Adaptive Control of KNTU Planar Cable-Driven Parallel Robot with Uncertainties in Dynamic and Kinematic Parameters*, volume 32, pages 145–159. 08 2015. ISBN 978-3-319-09488-5. doi: 10.1007/978-3-319-09489-2_11.

E. Barnett and C. Gosselin. Large-scale 3d printing with a cable-suspended robot. *Additive Manufacturing*, 7:27–44, 2015. ISSN 2214-8604. doi: https://doi.org/10.1016/j.addma.2015.05.001. URL `https://www.sciencedirect.com/science/article/pii/S2214860415000263`.

G. Barrette and C. Gosselin. Determination of the dynamic workspace of cable-driven planar parallel mechanisms. *Journal of Mechanical Design*, 127:242–248, 03 2005. doi: 10.1115/1.1830045.

J. Baumgarte. Stabilization of constraints and integrals of motion in dynamical systems. *Computer Methods in Applied Mechanics and Engineering*, 1(1):1–16, 1972. ISSN 0045-7825. doi: https://doi.org/10.1016/0045-7825(72)90018-7. URL `https://www.sciencedirect.com/science/article/pii/0045782572900187`.

H. Bayani, M. T. Masouleh, and A. Kalhor. An experimental study on the vision-based control and identification of planar cable-driven parallel robots. *Robotics and Autonomous Systems*, 75:187–202, 2016. ISSN 0921-8890. doi: https://doi.org/10.1016/j.robot.2015.10.002.

J Beckers, T Verstraten, B Verrelst, F Contino, and J Van Mierlo. Analysis of the dynamics of a slider-crank mechanism locally actuated with an act-and-wait controller. *Mechanism and Machine Theory*, 159:104253, 2021. ISSN 0094-114X. doi: https://doi.org/10.1016/j.mechmachtheory.2021.104253. URL `https://www.sciencedirect.com/science/article/pii/S0094114X21000112`.

Y. Babazadeh Bedoustani, H. D. Taghirad, and M. M. Aref. Dynamics analysis of a redundant parallel manipulator driven by elastic cables. In *2008 10th International Conference on Control, Automation, Robotics and Vision*, pages 536–542, 2008. doi: 10.1109/ICARCV.2008.4795575.

B. Belzile, P. K. Eskandary, and J. Angeles. Workspace determination and feedback control of a pick-and-place parallel robot: Analysis and experiments. *IEEE Robotics and Automation Letters*, 5(1):40–47, 2020. ISSN 2377-3766. doi: 10.1109/LRA.2019.2945468.

D. P. Bertsekas. *History of strength of materials*. McGraw-Hill, New York, 1982.

P. Bosscher, R. Williams, and M. Tummino. A concept for rapidly-deployable cable robot search and rescue systems. 01 2005. doi: 10.1115/DETC2005-84324.

S. Bouchard and C. Gosselin. Workspace optimization of a very large cable-driven parallel mechanism for a radiotelescope application. 01 2007. doi: 10.1115/DETC2007-34286.

F Boyer, V Lebastard, F Candelier, and F Renda. Dynamics of continuum and soft robots: a strain parametrization based approach. *IEEE Transactions on Robotics*, November 2020. doi: 10.1109/TRO.2020.3036618. URL `https://hal.science/hal-02318617`.

T. Bruckmann, A. Pott, D. Franitza, and M. Hiller. A modular controller for redundantly actuated tendon-based stewart platforms. *In 1st European Conference on Mechanism Science*, page 1–12, 2006.

J. Burke, D. Henrion, A. Lewis, and M. Overton. Hifoo - a matlab package for fixed-order contoller design and $\mathcal{H}_\infty$ optimization. In *In IFAC Symposium on Robust Control Design*, page 339–344, 2006.

M. Carricato and Jean-Pierre Merlet. Geometrico-static analysis of under-constrained cable-driven parallel robots. pages 309–319, 06 2010. ISBN 978-90-481-9261-8. doi: 10.1007/978-90-481-9262-5_33.

D. Chamaret, M. Naud, L. Hamon, S. Ullah, E. Richard, and P. Richard. Human-Scale Haptic Interaction Using the SPIDAR. In *Joint Virtual Reality Conference EGVE-ICAT-EURO VR (JVRC 2009)*, pages 123–128, Lyon, France, 2009. URL `https://hal.archives-ouvertes.fr/hal-00957369`.

I. Chawla, P. M. Pathak, L. Notash, A. K. Samantaray, Q. Li, and U. K. Sharma. Workspace analysis and design of large-scale cable-driven printing robot considering cable mass and mobile platform orientation. *Mechanism and Machine Theory*, 165:104426, 2021. ISSN 0094-114X. doi: https://doi.org/10.1016/j.mechmachtheory.2021.104426. URL `https://www.sciencedirect.com/science/article/pii/S0094114X21001841`.

R. Chellal. *Commande Robuste des Robots Parallèles à Câbles avec Mesure Extéroceptive.* PhD thesis, University of Strasbourg France, 2016.

R. Chellal, L. Cuvillon, and E. Laroche. *A Kinematic Vision-Based Position Control of a 6-DoF Cable-Driven Parallel Robot*, volume 32, pages 213–225. 08 2015. ISBN 978-3-319-09488-5. doi: 10.1007/978-3-319-09489-2_15.

R. Chellal, L. Cuvillon, and E. Laroche. Model identification and vision-based $\mathcal{H}_\infty$ position control of 6-dof cable-driven parallel robots. *International Journal of Control*, 90(4):684–701, 2017. doi: 10.1080/00207179.2016.1220623. URL `https://doi.org/10.1080/00207179.2016.1220623`.

J. F. Collard, J. Lamaury, and M. Gouttefarde. Dynamics modelling of large suspended parallel cable-driven robots multibody model. pages 3–5, 01 2011.

LL. Cone. Skycam: an aerial robotic camera system. (Byte 1985;10(10):122–32.), 1985.

X. Cui, W. Chen, X. Jin, and S. Agrawal. Design of a 7-dof cable-driven arm exoskeleton (carex-7) and a controller for dexterous motion training or assistance. *IEEE/ASME Transactions on Mechatronics*, 22:1–1, 01 2016. doi: 10.1109/TMECH.2016.2618888.

T Dallej, M Gouttefarde, N Andreff, P. E Hervé, and P Martinet. Modeling and vision-based control of large-dimension cable-driven parallel robots using a multiple-camera setup. *Mechatronics*, 61:20–36, 2019. ISSN 0957-4158. doi: https://doi.org/10.1016/j.mechatronics.2019.05.004. URL `https://www.sciencedirect.com/science/article/pii/S0957415819300662`.

A. DeLuca and B. Siciliano. Inversion-based nonlinear control of robot arms with flexible links. *Journal of Guidance, Control, and Dynamics*, 16(6):1169–1176, 1993. doi: 10.2514/3.21142.

J. Deschenes, P. Lambert, S. Perreault, N. Martel-Brisson, N. Zoso, A. Zaccarin, P. Hebert, S. Bouchard, and C. M. Gosselin. A cable-driven parallel mechanism for capturing object appearance from multiple viewpoints. In *Sixth International Conference on 3-D Digital Imaging and Modeling (3DIM 2007)*, pages 367–374, 2007. ISBN 1550-6185. doi: 10.1109/3DIM.2007.4.

J. Doyle and G. Stein. Multivariable feedback design: Concepts for a classical/modern synthesis. *IEEE Transactions on Automatic Control*, 26(1):4–16, 1981. doi: 10.1109/TAC.1981.1102555.

J. Doyle, K. Glover, P. Khargonekar, and B. Francis. State space solution to standard h_2 and $\mathcal{H}_\infty$ control problem. *Automatic Control, IEEE Transactions on*, 34:831 – 847, 09 1989. doi: 10.1109/9.29425.

J. Du and S. Agrawal. Dynamic modeling of cable-driven parallel manipulators with distributed mass flexible cables. *Journal of Vibration and Acoustics*, 137(2), 2015. doi: 10.1115/1.4029486.

J. Du, H. Bao, C. Cui, and D. Yang. Dynamic analysis of cable-driven parallel manipulators with time-varying cable lengths. *Finite Elements in Analysis and Design*, 48(1):1392–1399, 2012. ISSN 0168-874X. doi: https://doi.org/10.1016/j.finel.2011.08.012. URL `https://www.sciencedirect.com/science/article/pii/S0168874X11001533`.

J. L. Du, Chuanzhen Cui, Hong Bao, and Y.Y. Qiu. Dynamic analysis of cable-driven parallel manipulators using a variable length finite element. *Journal of Computational and Nonlinear Dynamics*, 10:011013, 09 2014. doi: 10.1115/1.4026570.

G. R. Duan. *Analysis and design of descriptor linear systems*. Advances in Mechanics and Mathematics, Springer, 2010.

G. Duc. *La synthèse $\mathcal{H}_\infty$ en pratique: Méthode et cas d'application*. 01 2022. ISBN 978-2-10-082556-1.

S. Fang, D. Franitza, M. Torlo, F. Bekes, and M. Hiler. Motion control of a tendon-based parallel manipulator using optimal tension distribution. *IEEE/ASME Transactions on Mechatronics*, page 561–568, 2004.

D. Farruggio and L. Menini. Control of a flexible link using $\mathcal{H}_\infty$ design methods. *IFAC Proceedings Volumes*, 33(14):495–500, 2000. ISSN 1474-6670. doi: https://doi.org/10.1016/S1474-6670(17)36277-8. URL `https://www.sciencedirect.`

com/science/article/pii/S1474667017362778. 3rd IFAC Symposium on Robust Control Design (ROCOND 2000), Prague, Czech Republic, 21-23 June 2000.

A. Fattah and A. Sunil. On the design of cable-suspended planar parallel robots. *Journal of Mechanical Design*, 127:1021–1028, 09 2005. doi: 10.1115/1.1903001.

M. Filipovic, Ana. Djuric, and L. Kevac. The rigid s-type cable-suspended parallel robot design, modelling and analysis. *Robotica*, 34:1948 – 1960, 2014.

D. Forsyth and J. Ponce. *Computer Vision: A Modern Approach. (Second edition)*. Prentice Hall, November 2011. URL `https://hal.inria.fr/hal-01063327`.

A. Fortin-Côté, P. Cardou, and C. Gosselin. An admittance control scheme for haptic interfaces based on cable-driven parallel mechanisms. In *2014 IEEE International Conference on Robotics and Automation (ICRA)*, pages 819–825, 2014. doi: 10.1109/ICRA.2014.6906949.

L. Gagliardini, M. Gouttefarde, and S. Caro. *Determination of a Dynamic Feasible Workspace for Cable-Driven Parallel Robots*, pages 361–370. Springer International Publishing, Cham, 2018. ISBN 978-3-319-56802-7. doi: 10.1007/978-3-319-56802-7_38. URL `https://doi.org/10.1007/978-3-319-56802-7_38`.

P Gahinet and P Apkarian. An lmi-based parametrization of all $\mathcal{H}_\infty$ controllers with applications. volume 1, pages 656 – 661 vol.1, 12 1993. ISBN 0-7803-1298-8. doi: 10.1109/CDC.1993.325066.

P. Gahinet and P. Apkarian. A linear matrix inequality approach to $\mathcal{H}_\infty$ control. *Int. J. Robust and Nonlinear Control*, 4(4):421–448, 07 1994. doi: 10.1002/rnc.4590040403.

P. Gholami, M. Aref, and H. Taghirad. On the control of the kntu cdrpm: A cable driven redundant parallel manipulator. pages 2404 – 2409, 10 2008. doi: 10.1109/IROS.2008.4650740.

H. Godbole, R. Caverly, and J. Forbes. Dynamic modeling and adaptive control of a single degree-of-freedom flexible cable-driven parallel robot. *Journal of Dynamic Systems, Measurement, and Control*, 141(10), 2019. doi: 10.1115/1.4043427.

H. Goldstein, C. Poole, and J. Safko. *Classical Mechanics*. Addison Wesley, San Francisco, 2002. ISBN 0201657023.

C. Gosselin. *Global Planning of Dynamically Feasible Trajectories for Three-DOF Spatial Cable-Suspended Parallel Robots*, pages 3–22. 09 2013. ISBN 978-3-642-31987-7. doi: 10.1007/978-3-642-31988-4_1.

C. Gosselin and M. Grenier. On the determination of the force distribution in overconstrained cable-driven parallel mechanisms. *Meccanica*, page 3–15, 2010.

M. Gouttefarde and C. M. Gosselin. On the Properties and the Determination of the Wrench-Closure Workspace of Planar Parallel Cable-Driven Mechanisms. In ASME, editor, *ASME Design Engineering Technical Conferences 2004*, page 10, Salt Lake City, Utah, USA, September 2004. URL `https://hal-lirmm.ccsd.cnrs.fr/lirmm-00198798`.

M. Gouttefarde and C.M. Gosselin. Analysis of the wrench-closure workspace of planar parallel cable-driven mechanisms. *IEEE Transactions on Robotics*, 22(3): 434–445, 2006. doi: 10.1109/TRO.2006.870638.

M. Gouttefarde, J. P. Merlet, and D. Daney. Wrench-feasible workspace of parallel cable-driven mechanisms. pages 1492–1497, 04 2007. doi: 10.1109/ROBOT.2007. 363195.

M. Gouttefarde, D. Daney, and J. P. Merlet. Interval-analysis-based determination of the wrench-feasible workspace of parallel cable-driven robots. *IEEE Transactions on Robotics*, 27(1):1–13, 2011. doi: 10.1109/TRO.2010.2090064.

M. Gouttefarde, J. F. Collard, N. Riehl, and C. Baradat. Simplified static analysis of large-dimension parallel cable-driven robots. In *2012 IEEE International Conference on Robotics and Automation*, pages 2299–2305, 2012. doi: 10.1109/ICRA.2012.6225159.

M. Gouttefarde, J. Lamaury, C. Reichert, and T. Bruckmann. A. A versatile tension distribution algorithme for n-dof parallel robots driven by n+2 cables. *IEEE Transactions on Robotics*, page 1444–1457, 2015.

J. L. Ha, R. F. Fung, K. Y. Chen, and S. C. Hsien. Dynamic modeling and identification of a slider-crank mechanism. *Journal of Sound and Vibration - J SOUND VIB*, 289:1019–1044, 02 2006. doi: 10.1016/j.jsv.2005.03.011.

A. Habed. Approches géométriques en vision par ordinateur, 2022.

J. Harandi, M. Reza, S. A. Khalilpour, Taghirad D. Hamid, and R. Jose Guadalupe. Adaptive control of parallel robots with uncertain kinematics and dynamics. *Mechanical Systems and Signal Processing*, 157:107693, 2021. ISSN 0888-3270. doi: https://doi.org/10.1016/j.ymssp.2021.107693. URL `https://www.sciencedirect.com/science/article/pii/S0888327021000881`.

R Hartley and A Zisserman. *Multiple View Geometry in Computer Vision*. Cambridge University Press, 2 edition, 2004. doi: 10.1017/CBO9780511811685.

J. W. Helton. Orbit structure of the mobius transformation semigroup action on h-infinity (broadband matching). *Adv. Math. Suppl. Stud*, 3:129–197, 1978.

Y. Hirata and M. Sato. 3-dimensional interface device for virtual work space. *Proceedings of the IEEE/RSJ International Conference on Intelligent Robots and Systems*, 2:889–896, 1992.

K. Homma, O. Fukuda, J. Sugawara, Y. Nagata, and M. Usuba. A wire-driven leg rehabilitation system: development of a 4-dof experimental system. pages 908 – 913 vol.2, 08 2003. ISBN 0-7803-7759-1. doi: 10.1109/AIM.2003.1225463.

H. Irvine. *Cable structures*. MIT Press, Cambridge, MA, 1981.

J. B. Izard, A. Dubor, P. E. Herve, E. Cabay, D. Culla, M. Rodriguez, and M. Barrado. Large-scale 3d printing with cable-driven parallel robots. *Construction Robotics*, 1:1–8, 12 2017. doi: 10.1007/s41693-017-0008-0.

H. Jia, W. Shang, F. Xie, B. Zhang, and S. Cong. Second-order sliding-mode-based synchronization control of cable-driven parallel robots. *IEEE/ASME Transactions on Mechatronics*, 25(1):383–394, 2020. ISSN 1941-014X. doi: 10.1109/TMECH. 2019.2960048.

H. Jianjun, G. Hong, and W. ZHELONG. Solving the forward kinematics problem of six-dof stewart platform using multi-task gaussian process. *Proceedings of the Institution of Mechanical Engineers, Part C: Journal of Mechanical Engineering Science*, 227:161–169, 01 2013. doi: 10.1177/0954406212444508.

M. Katliar, J. Fischer, G. Frison, M. Diehl, H. Teufel, and H. H. Bülthoff. Nonlinear model predictive control of a cable-robot-based motion simulator. *IFAC-PapersOnLine*, 50(1):9833–9839, 2017. ISSN 2405-8963. doi: https://doi.org/ 10.1016/j.ifacol.2017.08.901. URL `https://www.sciencedirect.com/science/article/pii/S2405896317313678`.

S. Kawamura, W. Choe, S. Tanaka, and S.R. Pandian. Development of an ultrahigh-speed robot falcon using wire drive system. In *Proceedings of 1995 IEEE International Conference on Robotics and Automation*, volume 1, pages 215–220 vol.1, 1995. doi: 10.1109/ROBOT.1995.525288.

I. Khayour, S. Durand, L. Cuvillon, and J. Gangloff. Active damping of parallel robots driven by elastic cables using on-off actuators through model predictive control allocation. *IFAC-PapersOnLine*, 53(2):9169–9174, 2020. ISSN 2405-8963. doi: https://doi.org/10.1016/j.ifacol.2020.12.2167. URL `https://www.sciencedirect.com/science/article/pii/S2405896320328202`.

K. Kozak, Qian Zhou, and Jinsong Wang. Static analysis of cable-driven manipulators with non-negligible cable mass. *IEEE Transactions on Robotics*, 22(3): 425–433, 2006. doi: 10.1109/TRO.2006.870659.

W. Kraus, P. Miermeister, V. Schmidt, and A. Pott. Hybrid position-force control of a cable-driven parallel robot with experimental evaluation. *Mechanical Sciences*, 6:119–125, 08 2015. doi: 10.5194/ms-6-119-2015.

P Lafourcade. *Étude des manipulateurs parallèles à câbles, conception d'une suspension active pour soufflerie*. PhD thesis, École Nationale Supérieure de l'Aéronautique et de l'Espace, France, 2004.

J. Lamaury and M. Gouttefarde. Control of a large redundantly actuated cable-suspended parallel robot. In *2013 IEEE International Conference on Robotics and Automation*, pages 4659–4664, 2013. doi: 10.1109/ICRA.2013.6631240.

C. Lambert, M. Nahon, and D. Chalmers. Implementation of an aerostat positioning system with cable control. *Mechatronics, IEEE/ASME Transactions on*, 12:32 – 40, 03 2007. doi: 10.1109/TMECH.2006.886251.

S. Landsberger and T. Sheridan. A new design for parallel link manipulator. *In International Conference on Systems, Man and Cybernetics*, page 812–814, 1985.

A. J. Laub, M. T. Heath, C. C. Paige, and R. C. Ward. Computation of system balancing transformations and other applications of simultaneous diagonalization algorithms. *IEEE Trans. Autom. Control*, AC-32(2), 1987.

Q. Liu, J. Zuo, C. Zhu, W. Meng, Q. Ai, and S. Q. Xie. Design and hierarchical force-position control of redundant pneumatic muscles-cable-driven ankle rehabilitation robot. *IEEE Robotics and Automation Letters*, 7(1):502–509, 2022. doi: 10.1109/LRA.2021.3123747.

K. Mankala, S. Agrawal, S. Canfield, and J. Peddieson. Dynamic model verification process for a rotating, elastic in-space tether. *Proceedings of the ASME Design Engineering Technical Conference*, 2006, 01 2006. doi: 10.1115/DETC2006-99746.

L. Meirovitch. *Analytical Methods in Vibrations*. Macmillan, New York, 1967.

J. P. Merlet. Marionet, a family of modular wire-driven parallel robots. 07 2010. ISBN 978-90-481-9261-8. doi: 10.1007/978-90-481-9262-5_6.

J. P. Merlet and D. Daney. A portable, modular parallel wire crane for rescue operations. pages 2834–2839, 05 2010. doi: 10.1109/ROBOT.2010.5509299.

J.P. Merlet. *Parallel Robots*. Solid Mechanics and Its Applications. Springer Netherlands, 2012. ISBN 9789401095877. URL https://books.google.fr/books?id=GydrCQAAQBAJ.

L. Mikelsons, T. Bruckmann, M. Hiller, and D. Schramm. A real-time capable force calculation algorithm for redundant tendon-based parallel manipulators. In *2008 IEEE International Conference on Robotics and Automation*, pages 3869–3874, 2008. doi: 10.1109/ROBOT.2008.4543805.

A. Ming and Higuchi Toshiro. Study on multiple degree-of-freedom positioning mechanism using wires (part 1) - concept, design and control. *Int. J. Jpn Soc. Eng.*, 28:131–138, 01 2004.

U. Mishra and S. Caro. *Unsupervised Neural Network Based Forward Kinematics for Cable-Driven Parallel Robots with Elastic Cables*, pages 63–76. 06 2021. ISBN 978-3-030-75788-5. doi: 10.1007/978-3-030-75789-2_6.

M. Opl, Michal Holub, J. Pavlík, F. Bradáč, P. Blecha, J. Kozubík, and J. Coufal. *DELTA - Robot with Parallel Kinematics*, pages 445–452. 01 2012. ISBN 978-3-642-23243-5. doi: 10.1007/978-3-642-23244-2_54.

E. Ottaviano, V. Gattulli, F. Potenza, and P. Rea. Modeling a planar point mass sagged cable-suspended manipulator. 2015.

S. Perreault and C. Gosselin. Cable-driven parallel mechanisms: Application to a locomotion interface. *Journal of Mechanical Design*, 130:102301, 10 2008. doi: 10.1115/1.2965607.

S. Perreault, P. Cardou, C. Gosselin, and M. Otis. Geometric determination of the interference-free constant-orientation workspace of parallel cable-driven mechanisms. *ASME Journal of Mechanisms and Robotics*, 2, 08 2010. doi: 10.1115/1.4001780.

B. Pham, S. Yeo, G. Yang, and I. M. Chen. Workspace analysis of fully restrained cable-driven manipulators. *Robotics and Autonomous Systems*, 57:901–912, 09 2009. doi: 10.1016/j.robot.2009.06.004.

B. Poitrimol and H. Igarashi. Haptic interface for virtual reality based on hybrid cable-driven parallel robot. In *2020 IEEE 16th International Workshop on Advanced Motion Control (AMC)*, pages 351–356, 2020. ISBN 1943-6580. doi: 10.1109/AMC44022.2020.9244444.

A. Pott, T. Bruckmann, and L. Mikelsons. Computational kinematics : Proceedings of the 5th international workshop on computational kinematics, chapitre closed-form force distribution for parallel wire robots. *Springer*, pages 25–34, 2009.

A. Pott, H. Mütherich, W. Kraus, V. Schmidt, P. Miermeister, and A. Verl. *IPAnema: A family of Cable-Driven Parallel Robots for Industrial Applications*, volume 12, pages 119–134. 01 2013. ISBN 9783642319877. doi: 10.1007/978-3-642-31988-4_8.

J. Pusey, A. Fattah, S. Agrawal, and E. Messina. Design and workspace analysis of a 6–6 cable-suspended parallel robot. *Mechanism and Machine Theory*, 39:761–778, 07 2004. doi: 10.1016/j.mechmachtheory.2004.02.010.

W. Qian, L. Ai, Z. Zhou, J. Liao, X. Xiao, and Z. Guo. Adaptive impedance control of a 6-dof cable-driven compliant upper limb rehabilitation robot. In *27th International Conference on Mechatronics and Machine Vision in Practice (M2VIP)*, pages 534–539, 2021. doi: 10.1109/M2VIP49856.2021.9665097.

R. Rahmani, S. Mobayen, and M. H. Barhaghtalab. Position tracking of parallel robot by an adaptive second order sliding mode control based on projection neural network. In *28th Iranian Conference on Electrical Engineering (ICEE)*, pages 1–5, 2020. ISBN 2642-9527. doi: 10.1109/ICEE50131.2020.9260594.

N. Riehl, M. Gouttefarde, S. Krut, C. Baradat, and F. Pierrot. Effects of Non-Negligible Cable Mass on the Static Behavior of Large Workspace Cable-Driven Parallel Mechanisms. In *ICRA: International Conference on Robotics and Automation*, pages 2193–2198, Kobe, Japan, May 2009. IEEE. doi: 10.1109/ROBOT.2009.5152576. URL https://hal-lirmm.ccsd.cnrs.fr/lirmm-00397805.

R. Saadaoui, G. I. Bara, H. Omran, O. Piccin, and E. Laroche. $\mathcal{H}_\infty$ synthesis for a planar flexible cable-driven robot. In *2021 European Control Conference (ECC)*, pages 710–715, 2021. doi: 10.23919/ECC54610.2021.9654926.

R. Saadaoui, E. Laroche, I. G. Bara, and O. Piccin. $\mathcal{H}_\infty$ control of a planar 3-dof flexible-cable manipulator. *IFAC-PapersOnLine*, 55(25):199–204, 2022a. ISSN 2405-8963. doi: https://doi.org/10.1016/j.ifacol.2022.09.347. URL https://www.sciencedirect.com/science/article/pii/S2405896322016020. 10th IFAC Symposium on Robust Control Design ROCOND 2022.

R. Saadaoui, O. Piccin, H. Omran, I. G. Bara, and E. Laroche. Control-Oriented Modeling of a Planar Cable-Driven Parallel Robot with Non-Straight Cables. 10th European Nonlinear Dynamics Conferences ENOC22, Lyon, France, juillet 2022, July 2022b. URL https://hal.archives-ouvertes.fr/hal-03799514. Poster.

D. Sai, J. Fengshui, Z. Rongzhang, L. Zize, and Y. Guodong. Multi-objective pose optimal distribution method for the feed support system of five-hundred-meter aperture spherical radio telescope. *International Journal of Advanced Robotic Systems*, 15:172988141875669, 02 2018. doi: 10.1177/1729881418756695.

P. Shi, J. Mcphee, and G.R. Heppler. A deformation field for euler-bernoulli beams with applications to flexible multibody dynamics. *Multibody System Dynamics*, 5:2001, 2000.

Y. Sugahara, T. Ueki, D. Matsuura, Y. Takeda, and M. Yoshida. Offline reference trajectory shaping for a cable-driven earthquake simulator based on a viscoelastic cable model. *IEEE Robotics and Automation Letters*, 7(2):2415–2422, 2022. doi: 10.1109/LRA.2022.3144778.

Y. Suilu, W. Zhao, L. Qi, and C. Yixin. Stiffness analysis of a wire-driven parallel manipulator. In *2012 IEEE International Conference on Computer Science and Automation Engineering (CSAE)*, volume 3, pages 31–34, 2012. doi: 10.1109/CSAE.2012.6272901.

D. Surdilovic, J. Radojicic, and J. Krüger. *Geometric Stiffness Analysis of Wire Robots: A Mechanical Approach*, pages 389–404. 09 2013. ISBN 978-3-642-31987-7. doi: 10.1007/978-3-642-31988-4_24.

P. Tempel, D. Lee, F. Trautwein, and A. Pott. *Modeling of Elastic-Flexible Cables with Time-Varying Length for Cable-Driven Parallel Robots*, pages 295–306. 06 2019. ISBN 978-3-030-20750-2. doi: 10.1007/978-3-030-20751-9_25.

S. Timoshenko. *Constrained Optimization and Lagrange Multiplier Methods*. Academic Press, New York, 1953.

R. Toscano. *Structured controllers for uncertain systems. A stochastic optimization approach.* 01 2013. ISBN 978-1-4471-5187-6. doi: 10.1007/978-1-4471-5188-3.

A. Vafaei, M. M. Aref, and H. D. Taghirad. Integrated controller for an over-constrained cable driven parallel manipulator: Kntu cdrpm. *2010 IEEE International Conference on Robotics and Automation*, pages 650–655, 2010.

X. Weber, L. Cuvillon, and J. Gangloff. Active vibration canceling of a cable-driven parallel robot using reaction wheels. In *2014 IEEE/RSJ International Conference on Intelligent Robots and Systems*, pages 1724–1729, 2014. doi: 10.1109/IROS.2014.6942787.

R. L. Williams II and P. Gallina. Translational planar cable-direct-driven robots. *Journal of Intelligent and Robotic Systems*, 37(1):69–96, 2003. ISSN 1573-0409. doi: 10.1023/A:1023975507009. URL https://doi.org/10.1023/A:1023975507009.

R. L. Williams II, P. Gallina, and J. Vadia. Planan translational cable-direct-driven robots. *Journal of Robotic Systems*, 20(3):107–120, 2003. doi: 10.002/rob.10073.

S. Xiang, H. Gao, Z. Liu, and C. Gosselin. Dynamic transition trajectory planning of three-dof cable-suspended parallel robots via linear time-varying mpc. *Mechanism and Machine Theory*, 146:103715, 2020. ISSN 0094-114X. doi: https://doi.org/10.1016/j.mechmachtheory.2019.103715. URL https://www.sciencedirect.com/science/article/pii/S0094114X19323213.

X. Yangwen, L. Qi, Z. Yaqing, and L. Bin. Model aerodynamic tests with a wire-driven parallel suspension system in low-speed wind tunnel. *Chinese Journal of Aeronautics*, 23(4):393–400, 2010. ISSN 1000-9361. doi: https://doi.org/10.1016/S1000-9361(09)60233-8.

M. J Yazdanpanah. *Control of flexible-link manipulators using nonlinear $\mathcal{H}_\infty$ techniques*. PhD thesis, Concordia University, 1997. URL `https://spectrum.library.concordia.ca/id/eprint/361/`. Unpublished.

W. Yi, Y. Zheng, W. Wang, X. Tang, X. Liu, and F. Meng. Optimal design and force control of a nine-cable-driven parallel mechanism for lunar takeoff simulation. *Chinese Journal of Mechanical Engineering*, 32(1):73, 2019. ISSN 2192-8258. doi: 10.1186/s10033-019-0382-2. URL `https://doi.org/10.1186/s10033-019-0382-2`.

A. Yiğit, M. Perozo Arpa, M. Ouafo, L. Cuvillon, S. Durand, and J. Gangloff. Aerial manipulator suspended from a cable-driven parallel robot: Preliminary experimental results. In *2021 IEEE/RSJ International Conference on Intelligent Robots and Systems (IROS)*, pages 9662–9668, 2021. doi: 10.1109/IROS51168.2021.9635933.

M. Yousefzadeh and H. Tourajizadeh. Control and residual vibration suppression of a cable-suspended parallel robot with elastic cables. In *5th RSI International Conference on Robotics and Mechatronics (ICRoM)*, pages 558–563, 2017. ISBN 2572-6889. doi: 10.1109/ICRoM.2017.8466223.

H. Yuan, E. Courteille, and D. Deblaise. Static and dynamic stiffness analyses of cable-driven parallel robots with non-negligible cable mass and elasticity. *Mechanism and Machine Theory*, 85(85):64–81, 2015a. doi: 10.1016/j.mechmachtheory.2014.10.010. URL `https://hal.archives-ouvertes.fr/hal-01127965`.

H. Yuan, E. Courteille, and D. Deblaise. Static and dynamic stiffness analyses of cable-driven parallel robots with non-negligible cable mass and elasticity. *Mechanism and Machine Theory*, 85:64–81, 2015b. ISSN 0094-114X. doi: https://doi.org/10.1016/j.mechmachtheory.2014.10.010. URL `https://www.sciencedirect.com/science/article/pii/S0094114X14002572`.

G. Zames. Feedback and optimal sensitivity: Model reference transformations, multiplicative seminorms, and approximate inverses. *IEEE Trans. Automat.*, 26(2):301–320, 1981.

M. Zasadzinski, M. F. Khelfi, E. Richard, and M. Darouach. $\mathcal{H}_\infty$ reduced-order output feedback controller for trajectory tracking of robot manipulators. *IFAC Proceedings Volumes*, 30(6):1629–1634, 1997. ISSN 1474-6670. doi: https://doi.org/10.1016/S1474-6670(17)43594-4. URL `https://www.sciencedirect.com/science/article/pii/S1474667017435944`. IFAC Conference on Control of Industrial Systems "Control for the Future of the Youth", Belfort, France, 20-22 May.

K. Zhou, J. C. Doyle, and K. Glover, editors. *Robust and optimal control*. Prentice Hall, 1996.

Appendix A

Modeling

A.1 Determination of the small displacement δx

In this appendix section, we demonstrate the formula for the displacement along x (this formula is used in the section 3.2.1). We want to introduce the deformation $(x + \delta x, \delta y)$ of the point $(x, 0)$, with the assumption that the cable is inextensible, which means that a segment between x and $x + dx$ remains of length dx even during the deformations (see Figure A.1). First, we consider a point in its coordinates are $(x, 0)$, and at an infinitesimally small distance $dl = dx$ we consider a second one in its coordinates are $(x + dx, 0)$.

By applying a displacement $\delta y(x)$ along y direction, the point moves also along the direction x with δx. Then, the new coordinates of the points taken previously are $(x + \delta x(x), \delta y(x))$ and $(x + dx + \delta(x + dx), \delta(x + dx))$ (see Figure A.1).
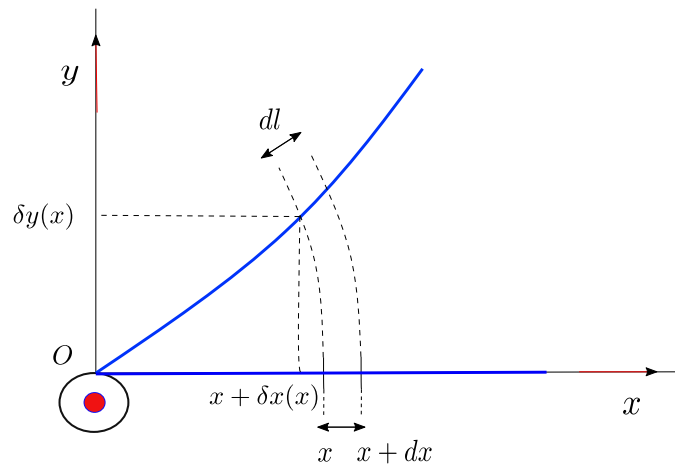

Figure A.1: Cable displacement

Since dl is a very small distance, we can consider that the curve that connects the two points is a straight line of modulus $dl = dx$. Then the displacement seen in detail will be as in the Figure A.2

Yet, we obtain the following expression:
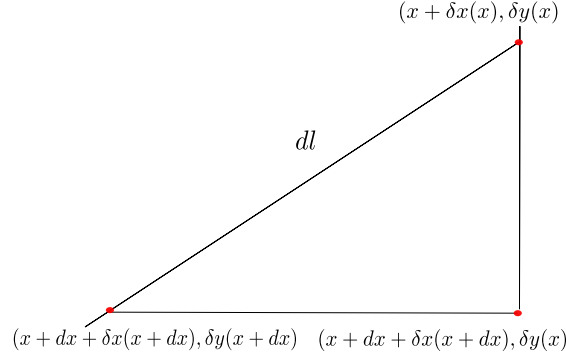
Figure A.2: Small displacement

$$dl^2 = dx^2 = [(x + dx + \delta x(x + dx) - x - \delta x(x))^2] + [(\delta y(x + dx) - \delta y(x))^2]. \quad (A.1)$$

Knowing that $(\delta y(x + dx) - \delta y(x)) \simeq \frac{\mathrm{d}\delta y}{\mathrm{d}x}\, dx$, we obtain:

$$dx^2 = (\frac{\mathrm{d}\delta y}{\mathrm{d}x}\, dx)^2 + (\frac{\mathrm{d}\delta x}{\mathrm{d}x}\, dx + dx)^2. \quad (A.2)$$

By developing the squared terms and with simplification, we obtain:

$$(\frac{\mathrm{d}\delta y}{\mathrm{d}x})^2 + (\frac{\mathrm{d}\delta x}{\mathrm{d}x} + 1)^2 = 1. \quad (A.3)$$

$$\frac{\mathrm{d}\delta x}{\mathrm{d}x} = \sqrt{1 - (\frac{\mathrm{d}\delta y}{\mathrm{d}x})^2} - 1. \quad (A.4)$$

For small displacements, we consider the Taylor expansion in the neighborhood of zero, then the first order of the right side of the equality in A.4) is expressed as:

$$\frac{\mathrm{d}\delta x}{\mathrm{d}x} = 1 - \frac{1}{2}(\frac{\mathrm{d}\delta y}{\mathrm{d}x})^2 - 1. \quad (A.5)$$

We perform a change of variable $\zeta = \frac{\mathrm{d}\delta y}{\mathrm{d}x}$ and we obtain the expression for displacements along the direction x:

$$\delta x = -\frac{1}{2}\int_0^x (\frac{\mathrm{d}\delta y}{\mathrm{d}x})^2\, d(\frac{\mathrm{d}\delta y}{\mathrm{d}x}) \quad (A.6)$$

A.2   The slider-crank mechanism model

Before performing the ODE transformation on the complex flexible cable robot model in section (3.2.6) , we tested this transformation on a simple model Slider-crank mechanism to verify if it solve the problem of the non-controllability and non-observability of the linear DAE model.

The slider-crank mechanism is a nonlinear mechanical system that is often used in the literature (Ha et al. (2006),Beckers et al. (2021)) (see Figure A.3). For the

modeling strategy, this mechanism can be considered as a double pendulum with a constraint $(y_2 = 0)$ as represented in Figure A.4. This mechanism commonly used to transform the straight line motion into a rotational motion.

A.2.1   Geometric equations
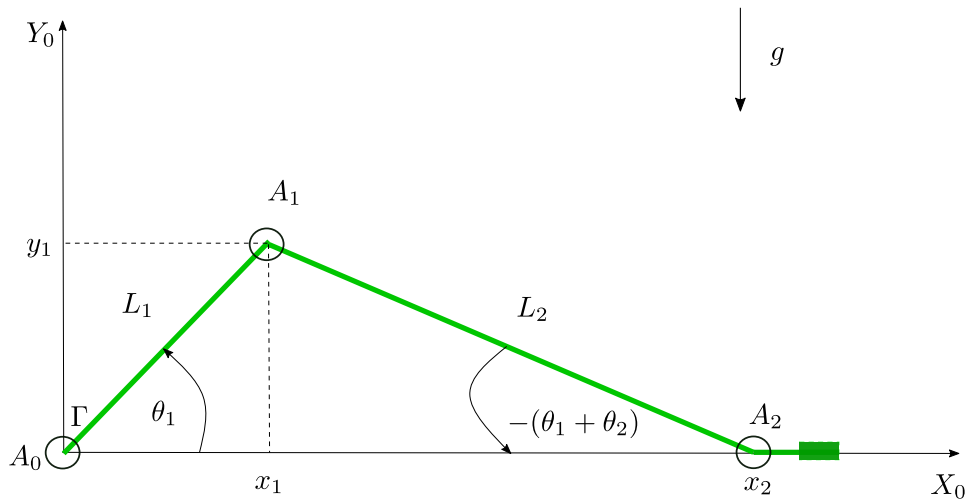
Figure A.3: Slider-Crank Mechanism
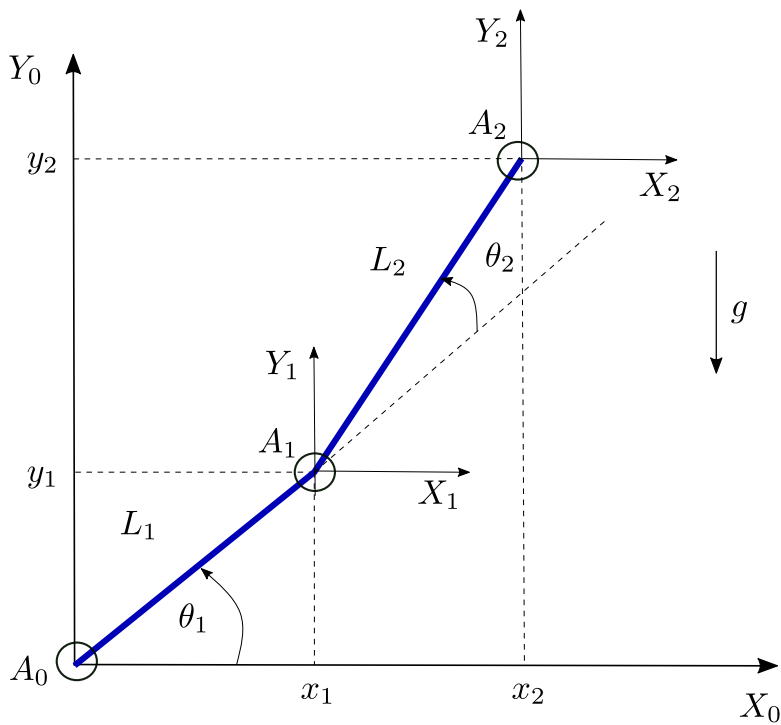

Figure A.4: Double pendulum system

Considering the minimal configuration, the slider-crank system is composed of two segments with lengths L_1 and L_2 and two punctual masses m_1 and m_2 attached to the ends of these segments. The fixed reference is $\mathcal{R}_0$ and the two references attached to the segments are $\mathcal{R}_i = (A_i, \mathbf{X_i}, \mathbf{Y_i})$ with $i = 1, 2$. The coordinates of A_i in the fixed reference $\mathcal{R}_0$ are $\mathbf{x_i}$ and $\mathbf{y_i}$, and the angles $\theta_i = (\mathbf{x_{i-1}}, \mathbf{x_i})$. The slider-crank system is a 1DOF system that can parameterized with θ_1, θ_2, x_2, and y_2.

The position expressions are given as:

$$x_1 = L_1 \cos\theta_1. \tag{A.7}$$

$$y_1 = L_1 \sin\theta_1. \tag{A.8}$$

$$x_2 = L_1 \cos\theta_1 + L_2 \cos(\theta_1 + \theta_2). \tag{A.9}$$

$$y_2 = L_1 \sin\theta_1 + L_2 \sin(\theta_1 + \theta_2). \tag{A.10}$$

and the constrained condition is given as:

$$y_2 = 0 \tag{A.11}$$

A.2.2 Kinematics analysis

Taking the time derivative of the positions, we obtain the velocities expressions as follows:

$$\dot{x}_1 = -L_1 \sin(\theta_1)\, \dot{\theta}_1. \tag{A.12}$$

$$\dot{y}_1 = L_1 \cos(\theta_1)\, \dot{\theta}_1. \tag{A.13}$$

$$\dot{x}_2 = -L_1 \sin(\theta_1)\, \dot{\theta}_1 - L_2 \sin(\theta_1 + \theta_2)\, (\dot{\theta}_1 + \dot{\theta}_2). \tag{A.14}$$

$$\dot{y}_2 = L_1 \cos(\theta_1)\, \dot{\theta}_1 + L_2 \cos(\theta_1 + \theta_2)\, (\dot{\theta}_1 + \dot{\theta}_2). \tag{A.15}$$

A.2.3 Differential-algebraic equations model (DAE)

The Lagrangian formalism is considered to obtain the dynamic model:

- The potential energy of the system is given as:

$$V(\theta_1, \theta_2) = m_1\, g\, y_1 + m_2\, g\, y_2. \tag{A.16}$$

- The kinetic energy of the system is calculated as follows:

$$T(\theta_2, \dot{\theta}_1, \dot{\theta}_2) = \frac{1}{2}\left(m_1\,(\dot{x}_1^2 + \dot{y}_1^2) + m_2\,(\dot{x}_2^2 + \dot{y}_2^2)\right) = \frac{1}{2}\,\dot{q}^T\, M(q)\, \dot{q} \tag{A.17}$$

where $q = \begin{bmatrix} \theta_1 & \theta_2 \end{bmatrix}^T$ is the coordinate vector and the kinetic inertia matrix $M(q)$ is presented as:

$$M(q) = \begin{bmatrix} M_{11} & M_{12} \\ M_{12} & M_{22} \end{bmatrix}$$
$$= \begin{bmatrix} (m_1 + m_2)\, L_1^2 + m_2\, L_2^2 + 2\, m_2\, L_1\, L_2\, cos\, \theta_2 & m_2\, (L_2^2 + L_1\, L_2\, cos\, \theta_2) \\ * & m_2\, L_2^2 \end{bmatrix}.$$
(A.18)

The Lagrangian formalism is used to obtain the equation of motion as follows:

$$\frac{\mathrm{d}}{\mathrm{d}t} \frac{\partial L}{\partial \dot{q}} - \frac{\partial L}{\partial q} = \underbrace{\Gamma}_{J^T\, Fx + C} + A^T \lambda \tag{A.19}$$

where:

- The Lagrange equation is given as $L = T - V$, then the left side terms of the equation (A.19) is calculated as: $\frac{\partial L}{\partial q} = \begin{bmatrix} \frac{\partial T}{\partial \theta_1} - \frac{\partial V}{\partial \theta_1} & \frac{\partial T}{\partial \theta_2} - \frac{\partial V}{\partial \theta_2} \end{bmatrix}^T$ with $\frac{\partial V}{\partial \theta_1} = m_1\, g\, L_1\, cos\, \theta_1 + m_2\, g\, (L_1\, cos\, \theta_1 + L_2\, cos(\theta_1 + \theta_2)$, $\frac{\partial V}{\partial \theta_2} = m_2\, g\, L_2\, cos(\theta_1 + \theta_2)$, $\frac{\partial T}{\partial \theta_1} = 0$, $\frac{\partial T}{\partial \theta_2} = -m_2\, L_2\, L_1\, sin\, \theta_2\, (\dot{\theta}_1 + \dot{\theta}_2)\, \dot{\theta}_1)$, then
  $$\frac{\partial L}{\partial q} = \begin{bmatrix} -g\, L_1\, (m_1 + m_2)\, cos\, \theta_1 - m_2\, g\, L_2\, cos(\theta_1 + \theta_2) \\ -m_2\, L_2\, L_1\, sin\, \theta_2\, (\dot{\theta}_1 + \dot{\theta}_2)\, \dot{\theta}_1 - m_2\, g\, L_2\, cos(\theta_1 + \theta_2) \end{bmatrix}.$$

- The matrix of the external forces Γ is given as follows: $\Gamma = J^T\, F_x + C$, with $C = \begin{bmatrix} c_1 & 0 \end{bmatrix}^T$ is the torque vector, F_x is the force applied to the system in the point A_2 in the direction x_0 and the matrix J is calculated as: $J = \begin{bmatrix} -L_1\, sin\, \theta_1 - L_2\, sin(\theta_1 + \theta_2) & -L_2\, sin(\theta_1 + \theta_2). \end{bmatrix}.$

- λ is the Lagrange multiplier vector.

- The matrix $A = \begin{bmatrix} L_1\, cos\, \theta_1 + L_2\, cos(\theta_1 + \theta_2) & L_2\, cos(\theta_1 + \theta_2) \end{bmatrix}$ is the Jacobian matrix of the constraint which fulfill that $A(q)\, \dot{q} = 0$.

The potential energy depends only on the generalized coordinate vector q, then the term $\frac{\mathrm{d}}{\mathrm{d}t} \frac{\partial L}{\partial \dot{q}}$ is calculated as: $\frac{\mathrm{d}}{\mathrm{d}t} \frac{\partial L}{\partial \dot{q}} = \begin{bmatrix} \frac{\mathrm{d}}{\mathrm{d}t} \frac{\partial T}{\partial \dot{\theta}_1} & \frac{\mathrm{d}}{\mathrm{d}t} \frac{\partial T}{\partial \dot{\theta}_2} \end{bmatrix}^T$ and given that $\frac{\partial T}{\partial \dot{\theta}} = M\, \dot{q}$, then $\frac{\mathrm{d}}{\mathrm{d}t} \frac{\partial T}{\partial \dot{\theta}} = M\, \ddot{q} + \dot{M}\, \dot{q}$ with the matrix $\dot{M}$ can be calculated as:
$$\dot{M} = \frac{\partial M}{\partial \theta_1}\, \dot{\theta}_1 + \frac{\partial M}{\partial \theta_2}\, \dot{\theta}_2 = \begin{bmatrix} -2\, m_2\, L_1\, L_2\, sin\, \theta_2\, \dot{\theta}_2 & -m_2\, L_1\, L_2\, sin\, \theta_2\, \dot{\theta}_2 \\ -m_2\, L_1\, L_2\, sin\, \theta_2\, \dot{\theta}_2 & 0 \end{bmatrix}.$$

The dynamic equation of motion of the constrained system in (A.19) can be rewritten as follows:

$$M\, \ddot{q} = \frac{\partial L}{\partial q} + \Gamma + A^T\, \lambda - \dot{M}\, \dot{q} \tag{A.20}$$

with $\ddot{q} = \begin{bmatrix} \ddot{\theta}_1 & \ddot{\theta}_2 \end{bmatrix}^T$.

By combining the dynamic equation of motion (A.20) and the time derivative of the constraint $(A(q)\, \dot{q} = 0)$, then the differential algebraic equation model can be obtained as follows:

$$\underbrace{\begin{bmatrix} M & -A^T \\ A & 0 \end{bmatrix}}_{G} \begin{bmatrix} \ddot{q} \\ \lambda \end{bmatrix} = \underbrace{\begin{bmatrix} \frac{\partial L}{\partial q} + \Gamma - \dot{M}\,\dot{q} \\ -\dot{A}\,\dot{q} \end{bmatrix}}_{F} \tag{A.21}$$

where matrix $\dot{A}$ is given by:

$$\dot{A} = \frac{\partial A}{\partial \theta_1}\,\dot{\theta}_1 + \frac{\partial A}{\partial \theta_2}\,\dot{\theta}_2$$
$$= \begin{bmatrix} -sin(\theta_1)\,L_1\,\dot{\theta}_1 - L_2\,sin(\theta_1 + \theta_2)\,\dot{\theta}_1 - L_2\,sin(\theta_1 + \theta_2)\,\dot{\theta}_2 & -sin(\theta_1 + \theta_2)\,L_2\,(\dot{\theta}_1 + \dot{\theta}_2). \end{bmatrix} \tag{A.22}$$

.

The DAE model has been linearized and the linear model has been found non-observable and non-controllable due to the geometric dependency between the variables, then to solve this problem we thought about reducing these geometric constraints by transforming the DAE model into and ordinary differential equation model (ODE).

A.3   The ordinary differential equation model (ODE)

The differential-algebraic equations (DAE) model presented with the two variables $q = \begin{bmatrix} \theta_1 & \theta_2 \end{bmatrix}^T$ can be reduced into an ordinary differential equations model (ODE) presented only with one variable by expressing θ_2 in the function of θ_1 due to the dependency between the two variables (θ_1, θ_2) caused by the geometric constraint.

From the geometric constraint in the equation A.11, then the variable θ_2 can be expressed in function of the variable θ_1 as follows:

$$\theta_2 = \arcsin(\frac{-L_1\,sin\,\theta_1}{L_2}) - \theta_1 \tag{A.23}$$

and then:

$$\dot{\theta}_2 = \frac{\partial \theta_2}{\partial \theta_1}\,\dot{\theta}_1 = (-\frac{L_1\,cos\,\theta_1}{L_2\,\sqrt{1 - \frac{L_1^2\,sin^2\theta_1}{L_2^2}}} - 1)\,\dot{\theta}_1. \tag{A.24}$$

The potential energy of the ODE model is given by the equation:

$$V_c = V(\theta_1) = g\,m_1\,L_1\,sin\,\theta_1. \tag{A.25}$$

The kinetic energy of the ODE model is then expressed as follows:

$$T_c = T(\theta_1, \dot{\theta}_1) = \frac{1}{2}\,\dot{q}_c^T\,M_c\,\dot{q}_c = \frac{1}{2}\,M_c\,\dot{\theta}_1^2. \tag{A.26}$$

Considering the first order kinetic model $\dot{q} = B\,\dot{q}_c$ given as:

$$\underbrace{\begin{bmatrix} \dot{\theta}_1 \\ \dot{\theta}_2 \end{bmatrix}}_{\dot{q}} = \underbrace{\begin{bmatrix} 0 \\ \frac{\partial \theta_2}{\partial \theta_1} \end{bmatrix}}_{B}\,\underbrace{\dot{\theta}_1}_{\dot{q}_c} \tag{A.27}$$

then equation (A.26) can be written as:

$$T_c = \frac{1}{2}\dot{q}_c^T\,\underbrace{B^T\,M\,B}_{M_c}\,\dot{q}_c \tag{A.28}$$

112

where matrix M_c is calculated as follows:

$$M_c(\theta_1) = B^T\, M\, B = J_1 + L_1^2\,(m_1 + m_2) + m_2\, L_2^2 + 2\, m_2\, L_1\, L_2\, cos(\theta_2) +$$
$$(\frac{-L_1\, cos(\theta_1)}{L_2\, \sqrt{1 - \frac{L_1^2\, sin(\theta_1)^2}{L2^2}}} - 1)\, m_2\, (L_2^2 + L_1\, L_2\, cos(\theta_2)) +$$
$$(m_2\, (L_2^2 + L_1\, L_2\, cos(\theta_2)) + (\frac{-L_1\, cos(\theta_1)}{L_2\, \sqrt{1 - \frac{L_1^2\, sin(\theta_1)^2}{L2^2}}} - 1)\, m_2\, L_2^2)\, (\frac{-L_1\, cos(\theta_1)}{L_2\, \sqrt{1 - \frac{L_1^2\, sin(\theta_1)^2}{L2^2}}} - 1).$$

$$(A.29)$$

The DAE model in the equation (A.21) can be transformed into an ODE model as follows:

$$M_c\, \ddot{q}_c = \frac{\partial L_c}{\partial q_c} + \Gamma_c - \dot{M}_c\, \dot{q}_c. \qquad (A.30)$$

where:

- $\frac{\partial L_c}{\partial q} = \frac{\partial Ecc}{\partial \theta_1} - \frac{\partial Epc}{\partial \theta_1}$ with $\frac{\partial Epc}{\partial \theta_1} = m_1\, g\, L_1\, cos(\theta_1)$ and, $\frac{\partial Ecc}{\partial \theta_1} = \frac{1}{2}\, \frac{\partial M_c}{\partial \theta_1}\, \dot{\theta}_1^2$.

- $\dot{M}_c(\theta_1, \dot{\theta}_1) = \frac{\partial M_c}{\partial \theta_1}\, \dot{\theta}_1$.

- $\Gamma_c = J_c\, Fx + c_1$ with $J_c = \frac{\partial x_2(\theta_1)}{\partial \theta_1} = -L_1\, sin(\theta_1) - L_2\, (1 + \frac{\partial \theta_2}{\partial \theta_1})\, sin(\theta_1 + \theta_2(\theta_1))$.

We linearized the obtained ODE model, then the linear model was found controllable and observable.

A.4 The pinhole model

The pinhole model (Hartley and Zisserman (2004)) is considered to model a camera by perspective projection (see Figure (A.5). This model has been used to calibrate and model the camera considering the perspective projection in section 3.3.3.

This model transforms a 3D point $P(X_s, Y_s, Z_s)$ of space into a 2D image point $p(u, v)$, this transformation is performed according to three transformations: The transformation between the world reference (O_s, X_s, Y_s, Z_s) and that of the camera (O, X, Y, Z), the transformation between the camera reference and the retinal plane reference $(c(u_0, v_0), x, y)$ and the transformation between retinal plane reference and the image reference (u, v).

A.4.1 First transformation

The Euclidean coordinates are expressed into a homogeneous coordinate in order to express the model of the pinhole by a linear relation, in 2D $\begin{pmatrix} x & y \end{pmatrix}^T$ becomes $\begin{pmatrix} x & y & 1 \end{pmatrix}^T$ and in 3D $\begin{pmatrix} X & Y & Z \end{pmatrix}^T$ becomes $\begin{pmatrix} X & Y & Z & 1 \end{pmatrix}^T$.

As shown in Figure A.5, the first transformation **[Rt]** is a rigid transformation that decomposes into a rotation **R** and a translation **t**. The parameters of this transformation are called the extrinsic parameters of the camera. This relations is presented as follows:
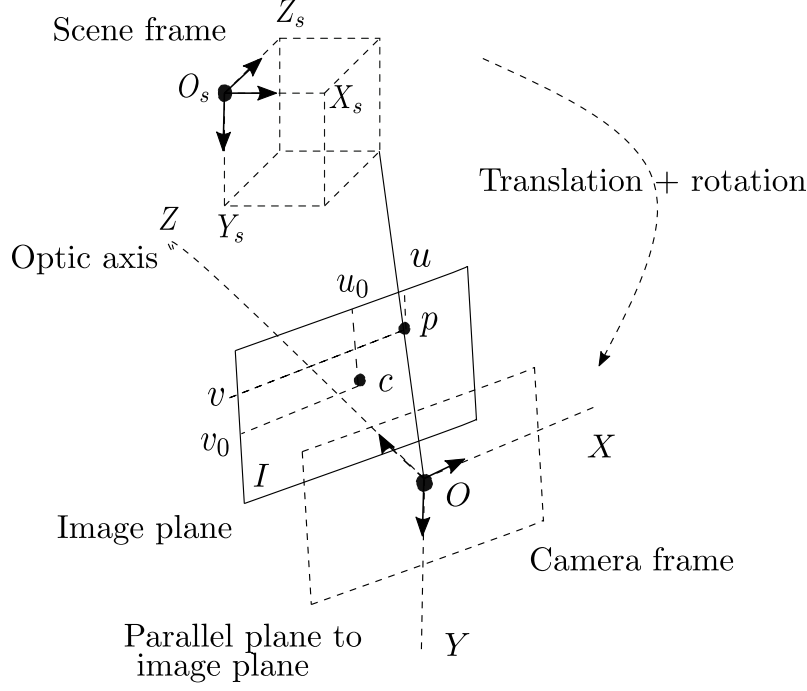
Figure A.5: Pinhole model Habed (2022)

$$
\begin{pmatrix} X \\ Y \\ Z \\ 1 \end{pmatrix} = \mathbf{R} \cdot \begin{pmatrix} X_s \\ Y_s \\ Z_s \end{pmatrix} + \mathbf{t} = \begin{pmatrix} \mathbf{R} & \mathbf{t} \\ 0^T & 1 \end{pmatrix} \cdot \begin{pmatrix} X_s \\ Y_s \\ Z_s \\ 1 \end{pmatrix} = \mathbf{T} \cdot \begin{pmatrix} X_s \\ Y_s \\ Z_s \\ 1 \end{pmatrix} \tag{A.31}
$$

where $\mathbf{t} = \begin{pmatrix} t_x \\ t_y \\ t_z \end{pmatrix}$ and $\mathbf{R} = \begin{pmatrix} r_{11} & r_{12} & r_{13} \\ r_{21} & r_{22} & r_{23} \\ r_{31} & r_{32} & r_{33} \end{pmatrix}$.

A.4.2   Second transformation

This transformation is a perspective projection $\mathbf{P}(3 \times 4)$ matrix which transforms a 3D point (X, Y, Z) into an image point (x, y) (in metric unit). This relations is presented as follows:

$$
s \cdot \begin{pmatrix} x \\ y \\ 1 \end{pmatrix} = \begin{pmatrix} f & 0 & 0 & 0 \\ 0 & f & 0 & 0 \\ 0 & 0 & 1 & 0 \end{pmatrix} \cdot \begin{pmatrix} X \\ Y \\ Z \\ 1 \end{pmatrix} = \mathbf{P} \cdot \begin{pmatrix} X \\ Y \\ Z \\ 1 \end{pmatrix} \tag{A.32}
$$

where s is a factor and f is the focal length of the lens.

A.4.3   Third transformation

This transformation corresponds to the operation of converting the metric image coordinates (x, y) into discrete image coordinates (u, v) (pixels). This relations is presented as follows:

114

$$\begin{pmatrix} u \\ v \\ 1 \end{pmatrix} = \begin{pmatrix} k_x & k_x \cot\theta & u_0 + v_0 \cot\theta \\ 0 & k_y/\sin\theta & v_0/\sin\theta \\ 0 & 0 & 1 \end{pmatrix} \cdot \begin{pmatrix} x \\ y \\ 1 \end{pmatrix} = \mathbf{A} \cdot \begin{pmatrix} x \\ y \\ 1 \end{pmatrix} \qquad (A.33)$$

where:

- u_0 and v_0 (in pixels) designate the coordinates of the intersection between the optical axis and the image plane.

- k_x and k_y designate the number of pixels per unit length along x and y of the sensor.

- θ translates the non-orthogonality of the rows and columns of the image.

As $\theta \simeq \frac{\pi}{2}$, then the relation simplifies as following:

$$\begin{pmatrix} u \\ v \\ 1 \end{pmatrix} = \begin{pmatrix} k_x & 0 & u_0 \\ 0 & k_y & v_0 \\ 0 & 0 & 1 \end{pmatrix} \cdot \begin{pmatrix} x \\ y \\ 1 \end{pmatrix} \qquad (A.34)$$

The multiplication of the matrix $\mathbf{A}$ by the matrix $\mathbf{P}$ gives the matrix containing the intrinsic parameters of the camera: $M_{int} = \mathbf{AP}$.

Finally, the complete model of the pinhole shown in Figure A.5 results in the following relation:

$$\begin{pmatrix} X_s & Y_s & Z_s \end{pmatrix} \xrightarrow{\mathbf{T}} \begin{pmatrix} X & Y & Z \end{pmatrix} \xrightarrow{\mathbf{P}} \begin{pmatrix} x & y \end{pmatrix} \xrightarrow{\mathbf{A}} \begin{pmatrix} u & v \end{pmatrix} \qquad (A.35)$$

The projection matrix will therefore be $M_P = APT$ of size 3×4.

Appendix B

Control

B.1 The Popov-Belevitch-Hautus theorems of controllability and observability

The Popov-Belevitch-Hautus theorems have been used to test the controllability and observability of the obtained linear models in the sections 3.2.5.

Theorem 1 (Popov-Belevitch-Hautus controllability test (Zhou et al. (1996))). The following conditions are equivalent:

   i (A, B) is controllable.

   ii The matrix $\begin{bmatrix} A - \lambda I & B \end{bmatrix}$ has full column rank for all $\lambda \in \mathbb{C}$.

   iii The controllability matrix $\mathcal{C} = \begin{bmatrix} B & AB & A^2B & \ldots & A^{n-1}B \end{bmatrix}$ has full row rank.

   iv Let λ and x be any eigenvalue and any corresponding left eigenvector of A, i.e., $x^*A = x^*\lambda$, then $x^*B \neq 0$.

Theorem 2 (Popov-Belevitch-Hautus observability test (Zhou et al. (1996))). The following conditions are equivalent:

   i (C, A) is detectable.

   ii The matrix $\begin{bmatrix} A - \lambda I \\ C \end{bmatrix}$ has full column rank for all $\operatorname{Re} \lambda \geq 0$.

   iii $\mathcal{O} = \begin{bmatrix} C \\ AC \\ A^2C \\ \vdots \\ A^{n-1}C \end{bmatrix}$ has full row rank.

   iv For all λ and x such that $A\,x = \lambda x$ and $\operatorname{Re} \lambda \geq 0$, $C\,x \neq 0$.

   v (A^*, C^*) is stabilizable.

B.2 Mathematical tools for the $\mathcal{H}_\infty$ synthesis

B.2.1 Singular values of a transfer matrix

Definition B.2.1 (Singular value of a matrix (Toscano (2013))). By considering the singular values of the transfer matrix $G(s)$, we can extend the frequency gain of a SISO system to a MIMO system. Considering the system response $y(t)$ with a number ny and the input system $u(t)$ with the number n_u, the response in the frequency domain of a SISO system $G(s)$ is given as:

$$y(j\omega) = G(j\omega)\,u(j\omega) \tag{B.1}$$

where $G(j\omega) = G(s)_{s=j\omega}$ and the gain of the SISO system at frequency ω is presented as $|G(j\omega)|$.

The frequency gain in the case of SISO systems are represented as a singular values is the case of MIMO systems. The singular values σ_i of the matrix $G(j\omega)$ are defined as the square roots of eigenvalues of $G(j\omega)G(j\omega)^*$ as follows:

$$\sigma_i(G(j\omega)) = \sqrt{\lambda_i(G(j\omega)G(j\omega)^*)} = \sqrt{\lambda_i(G(j\omega)^*G(j\omega))} \tag{B.2}$$

where $\lambda_i(G(j\omega)G(j\omega)^*)$ is an eigenvalue of the matrix $(G(j\omega)G(j\omega)^*)$, $i = 1, \ldots, \min(n_u, n_y)$, $G(j\omega)^* = G(-j\omega)^T$ is the conjugate transpose of $G(j\omega)$, and the two matrices $G(j\omega)^*G(j\omega)$ and $G(j\omega)G(j\omega)^*$ are Hermitian[a] positive semi-definite matrices, and their eigenvalues are non-negative. The largest $\bar{\sigma}(G(j\omega))$ and the smallest $\underline{\sigma}(G(j\omega))$ singular values of $G(s)$ are denoted as:

$$\bar{\sigma}(G(j\omega)) = \sigma_1(G(j\omega)) \geq \sigma_2(G(j\omega)) \geq \ldots \geq \underline{\sigma}(G(j\omega)) \geq 0 \quad \forall\,\omega \tag{B.3}$$

Figure (B.1) shows the frequency domain representation of singular values as a positive functions of ω.

[a]A matrix is Hermitian if it is equal to its conjugate transpose
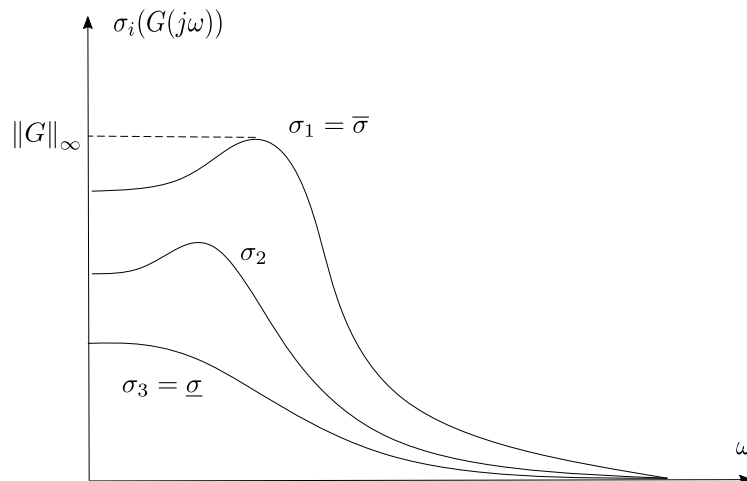
Figure B.1: Singular values and $\mathcal{H}_\infty$-norm of a transfer matrix (Toscano (2013))

B.2.2 $\mathcal{H}_2$ norm of system

> **Definition B.2.2 ($\mathcal{H}_2$ norm of a system).** Let G be a stable strictly proper transfer matrix defined as $G(s) = C(sI - A)^{-1}B$, the $\mathcal{H}_2$ norm of the system is represented as following:
> $$\|G\|_2 = \sqrt{\tfrac{1}{2\pi} \int_{-\infty}^{+\infty} Tr(G(j\omega)^* G(j\omega))d\omega}.$$

B.2.3 $\mathcal{H}_\infty$ norm of system

> **Definition B.2.3 ($\mathcal{H}_\infty$ norm of a system).** Let the LTI system be represented by the transfer function defined as $G(s) = C(sI - A)^{-1}B$. Then, the $\mathcal{H}_\infty$ norm of the stable system G is given by:
> $$\|G\|_\infty = \sup_w \overline{\sigma}(G(j\omega))$$

B.3   Riccati's algebraic equations approach

This approach of resolution of the $\mathcal{H}_\infty$ problem is based on the use of the state-space formulation and it has been presented by Doyle et al. (1989).

Let us introduce a minimal realization of the system $P(s)$:

$$P(s) = \begin{bmatrix} P_{11}(s) & P_{12}(s) \\ P_{21}(s) & P_{22}(s) \end{bmatrix} = \begin{bmatrix} C_1 \\ C_2 \end{bmatrix} [sI - A]^{-1} \begin{bmatrix} B_1 & B_2 \end{bmatrix} + \begin{bmatrix} D_{11} & D_{12} \\ D_{21} & D_{22} \end{bmatrix} \tag{B.4}$$

where $D_{12} \in \mathbb{R}^{p_1 \times m_2}$, $D_{21} \in \mathbb{R}^{p_2 \times m_1}$, $m_1 \geq p_2$, $p_1 \geq m_2$ and $A \in \mathbb{R}^{n \times n}$ and n the order of the system $P(s)$.

The $\mathcal{H}_\infty$ sub-optimal solution is obtained considering the following assumptions:

  i (A, B_2) stabilizable and (A, C_2) detectable.

 ii D_{12} has full column rank and D_{21} has full row rank.

iii rank $\begin{bmatrix} A - jwI & B_2 \\ C_1 & D_{12} \end{bmatrix} = n + m_2$ has full column rank for all $w \in \mathbb{R}$.

    the matrix D_{12} has full row rank for all $w \in \mathbb{R}$.

iv rank $\begin{bmatrix} A - jwI & B_1 \\ C_2 & D_{21} \end{bmatrix} = n + p_2$ has full row rank for all $w \in \mathbb{R}$.

    the matrix D_{21} is of full row rank $\forall w \in \mathbb{R}$.

Solving the following two Riccati equations to find the stabilizing solutions:

$$A^T X + X A + X(\gamma^{-2} B_1 B_1^T - B_2 B_2^T)X + C_1 C_1^T = 0 \tag{B.5}$$

$$A Y + Y A^T + Y(\gamma^{-2} C_1 C_1^T - C_2 C_2^T)Y + B_1 B_1^T = 0 \tag{B.6}$$

requires the calculation of the spectra of the following two Hamiltonian matrices:

$$H_\infty = \begin{bmatrix} A & \gamma^{-2} B_1 B_1^T - B_2 B_2^T \\ -C_1^T C_1 & -A^T \end{bmatrix} \quad J_\infty = \begin{bmatrix} A^T & \gamma^{-2} C_1^T C_1 - C_2^T C_2 \\ -B_1 B_1^T & -A \end{bmatrix} \tag{B.7}$$

Notice that the $\mathcal{H}_\infty$ controller does not cancel pole and zero on the imaginary axis that would results in closed-loop instability.

Theorem 3 (Doyle et al. (1989)). There exist an admissible controller K :

$$K = \begin{bmatrix} A_\infty & -Z_\infty L_\infty \\ -B_2^T X_\infty & 0 \end{bmatrix}$$ (B.8)

where:

- $A\infty = A + \gamma^{-2} B_1 B_1^T X_\infty + B_2 F_\infty + Z_\infty L_\infty C_2$.

- $L_\infty = -Y_\infty C_2^T$.

- $Z_\infty = (I - \gamma^2 Y_\infty X_\infty)^{-1}$.

In order to ensure the closed-loop system internally stable such that $\|T_{w \to z}\|_\infty < \gamma$, if and only if:

- $H_\infty \in dom(Ric)$ and $X_\infty = Ric(H_\infty) \geq 0$.

- $J_\infty \in dom(Ric)$ and $Y_\infty = Ric(J_\infty) \geq 0$.

- $\rho(X_\infty Y_\infty) < \gamma^2$.

where *Ric(H)* is the stabilizing solution of the algebraic Riccati equation and the domain of *Ric* is denotes *dom(Ric)*.

B.4   Linear matrix inequalities

Unlike the iterative Riccati approach, the performance criteria γ of the $\mathcal{H}_\infty$-optimal problem can be found directly with the LMI approach without iteration. In this approach, the sufficient and necessary conditions for the existence of an admissible controller are represented as linear matrix inequalities.

Lemma 4 (Gahinet and Apkarian (1994)). Consider a continuous-time transfer function G(s) of (not necessarily minimal) realization $G(s) = D + C(sI - A)^{-1} B$. The following statements are equivalent:

i $\|C(sI - A)^{-1} B + D\|_\infty < \gamma$ and A is stable in the continuous-time sense $Re(\lambda_i(A) < 0)$.

ii there exists a symmetric positive definite solution X to the LMI:

$$\begin{bmatrix} A^T X + XA & XB & C^T \\ B^T X & -\gamma I & D^T \\ C & D & -\gamma I \end{bmatrix} < 0.$$ (B.9)

Theorem 5 (Gahinet and Apkarian (1993)). Given $\gamma > 0$, the system (B.4) admits an $\mathcal{H}_\infty$ sub-optimal controller if and only there exist matrices X, $Y \in S_{n+n_k}$ satisfying the following LMI:

$$\begin{bmatrix} W_{[B_2^T D_{21}^T]} & 0 \\ 0 & I \end{bmatrix}^T \begin{bmatrix} AX + XA^T & XC_1^T & B_1 \\ C_1 X & -\gamma I & D_{11} \\ B_1^T & D_{11}^T & -\gamma I \end{bmatrix} \begin{bmatrix} W_{[B_2^T D_{21}^T]} & 0 \\ 0 & I \end{bmatrix} < 0. \tag{B.10}$$

$$\begin{bmatrix} W_{[C_2^T D_{21}]} & 0 \\ 0 & I \end{bmatrix}^T \begin{bmatrix} A^T Y + YA & YB_1^T & C_1^T \\ B_1^T Y & -\gamma I & D_{11}^T \\ C_1 & D_{11} & -\gamma I \end{bmatrix} \begin{bmatrix} W_{[C_2^T D_{21}]} & 0 \\ 0 & I \end{bmatrix} < 0. \tag{B.11}$$

$$\begin{bmatrix} X & I \\ I & Y \end{bmatrix} \geq 0. \tag{B.12}$$

where $W_{[B_2^T D_{21}^T]}, W_{[C_2^T D_{21}]}$ are the matrices whose columns form bases of the null spaces of $[B_2^T D_{21}^T]$ and $[C_2^T D_{21}]$, respectively.

The set of the γ sub-optimal controllers contains controllers of order $n_K < n_x$ if and only if the matrices X and Y moreover satisfy the rank constraint :

$$\mathrm{rank}(I - XY) \leq n_K. \tag{B.13}$$

Scientific contributions

International communications

R. Saadaoui, E. Laroche, G. I. Bara, et O. Piccin,"$\mathcal{H}_\infty$ Control of a Planar 3-DOF Flexible-Cable Manipulator," FAC-PapersOnLine, 55(25):199–204, 2022. ISSN 2405-896, doi.org/10.1016/j.ifacol.2022.09.347, Conference IFAC Symposium on Robust Control Design (ROCOND), 2022.

R. Saadaoui, O. Piccin, H. Omran, G. I. Bara et E. Laroche, "Control-Oriented Modeling of a Planar Cable-Driven Parallel Robot with Non-Straight Cables," 10th European Nonlinear Dynamics Conferences ENOC22, Lyon, France, juillet 2022 (**Best poster awards**).

R. Saadaoui, G. I. Bara, H. Omran, O. Piccin et E. Laroche,"$\mathcal{H}_\infty$ Synthesis for a Planar Flexible Cable-Driven Robot," 2021 European Control Conference (ECC), 710–715, doi: 10.23919/ECC54610.2021.9654926.

National communications

R. Saadaoui, G. I. Bara, H. Omran, O. Piccin et E. Laroche, "Commande $\mathcal{H}_\infty$ de robots à câbles en tenant compte des effets inertiels du déplacement transversal des câbles", CT MOSAR des Journées Nationales MACS, Novembre 2020.

R. Saadaoui, E. Laroche, G. I. Bara, H. Omran et O. Piccin "Commande des systèmes non-linéaires avec contraintes algébriques - application aux robots à câbles en tenant compte des déformations des câbles," présentation de poster, journée des doctorants de l'ED MSII, septembre 2019.

Rima Saadaoui

Commande robuste de robots plans à câbles en tenant en compte des déformations des câbles

Université de Strasbourg

École doctorale Mathématiques, sciences de l'information et de l'ingénieur | ED 269 — Université de Strasbourg

Résumé en français :

Au cours des dernières décennies, les robots parallèles à câbles ont suscité un vif intérêt pour l'industrie et la recherche scientifique. Ces robots combinent les propriétés mécaniques des mécanismes parallèles et aussi des câbles, ce qui les rend parfaitement adaptés à plusieurs applications. Les câbles présentent généralement un phénomène de déformation lors de mouvement générant des vibrations qui perturbent le positionnement d'effecteur.

Tout d'abord, nous avons revisité la modalisation dynamique des robots à câbles flexibles qui mène à un modèle algebro-différentielle où la flexibilité des câbles a été modélisée par la méthode des modes supposes. Ce modèle non-linéaire a été transformé en un modèle différentiel ordinaire dans le but d'obtenir après sa linéarisation un modèle commandable et observable adapté à la synthèse H∞. Ensuite, un correcteur H∞ robuste a été synthétisé pour commander les tensions des câbles et la suivie de trajectoire de la plate-forme. Une validation en simulation de la loi de commande sur un robot parallèle à quatre câbles a été effectuée. Cette étape a été précédée par une évaluation du modèle géométrique à partir d'images vidéos acquises sur le prototype de robot plan INCA.

Mots-clés : Robot parallèle à câbles, Câble flexible, Approche par modes supposés, Commande H∞, Commande robuste, Modèle algébro-différentiel, Modèle différentiel ordinaire.

Résumé en anglais :

Over the past decades, cable-driven parallel robots have evoked great interest in industry and scientific research. These robots combine the mechanical properties of parallel mechanisms and cables, which makes them perfectly suitable for several applications. During the movement, the cables show transverse vibration, which causes inaccuracy in the positioning of the platform.

First, we revisited the dynamic modeling of the flexible cable robot, which leads to a differential algebraic equation model where the flexibility of the cables was modeled using the assumed-modes approach. This model has been transformed into a non-linear ordinary differential equation model to obtain a controllable and observable model after its linearization. Then, an H∞ controller was synthesized to control the cable tensions and the trajectory tracking of the platform. Simulation validation of the control law on a parallel robot with four cables was performed, and an evaluation of the geometric model from video images acquired on the INCA prototype.

Keywords: Parallel cable robots, Flexible cable, Assumed-mode approach, H∞ synthesis, Robust control, Algebraic-differential model, Ordinary differential model.